ISSN: 2331-1959 Volume 11, Number 2, April 2023

Scientific Research Publishing

Archaeological Discovery

ISSN: 2331-1959

https://www.scirp.org/journal/ad

Journal Editorial Board

ISSN Print: 2331-1959 ISSN Online: 2331-1967

https://www.scirp.org/journal/ad

Archaeological Discovery, 2023, 11, 39-170
https://www.scirp.org/journal/ad
ISSN Online: 2331-1967
ISSN Print: 2331-1959

Table of Contents

Volume 11 Number 2 April 2023

Archaeological Discovery (AD)
Journal Information

SUBSCRIPTIONS

The *Archaeological Discovery* (Online at Scientific Research Publishing, https://www.scirp.org/) is published quarterly by Scientific Research Publishing, Inc., USA.

Subscription rates:
Print: $39 per issue.
To subscribe, please contact Journals Subscriptions Department, E-mail: sub@scirp.org

SERVICES

Advertisements
Advertisement Sales Department, E-mail: service@scirp.org

Reprints (minimum quantity 100 copies)
Reprints Co-ordinator, Scientific Research Publishing, Inc., USA.
E-mail: sub@scirp.org

COPYRIGHT

PRODUCTION INFORMATION

For manuscripts that have been accepted for publication, please contact:
E-mail: ad@scirp.org

Archaeological Discovery, 2023, 11, 39-64
https://www.scirp.org/journal/ad
ISSN Online: 2331-1967
ISSN Print: 2331-1959

Enigma of Alluvial Gold Mining in Pre-Contact Peru—The Present Is Key to the Past

William E. Brooks

Geologist, Reston, VA, USA
Email: webgeology@aim.com

How to cite this paper: Brooks, W. E. (2023). Enigma of Alluvial Gold Mining in Pre-Contact Peru—The Present Is Key to the Past. *Archaeological Discovery, 11,* 39-64.
https://doi.org/10.4236/ad.2023.112003

Received: January 3, 2023
Accepted: February 25, 2023
Published: February 28, 2023

Abstract

Peru has produced metals for thousands of years and is the leading gold producer in Latin America today; however, the indigenous mining technology used to produce industrial amounts of gold in pre-contact Peru has thus far been undescribed. Industrial amounts of gold are produced in only two ways: 1) gravity separation/mercury (amalgamation), and 2) cyanide. Therefore, an understanding of present-day gold mining methods is key to understanding gold mining in the past. For example, in 2018, Peru's large-scale open-pit gold mines produced 123,767 kg of gold using cyanide and 18,875 kg of gold were produced from small-scale alluvial gold mines that used gravity separation and mercury. Since cyanide was not used until the 1880s, mercury amalgamation must be critiqued as the mining technology that produced prodigious amounts of gold from alluvial sources in pre-contact Peru.

Keywords

Alluvial Gold, Mercury, Amalgamation, Retort, Pre-Contact Peru

1. Introduction

The ore of mercury, cinnabar (HgS), is a sulfide mineral that was widely used in the ancient world: 1) it was mined, selectively ground, and widely used as a blood-red pigment (vermilion) on ceramics, gold masks, murals, statues, burial rites (Petersen, 1970/2010; Bonavia, 1985; Brooks et al., 2008; Spindler, 2018) and, 2) it was retorted to produce mercury (Cabrera la Rosa, 1954; Craddock, 1995; Brooks, 2012). Retorting cinnabar to obtain mercury has been documented more than 8000 years ago in ancient Türkiye (Barnes & Bailey, 1972; Brooks et al., 2017); during Roman time (Pliny the Elder, 77 AD); the Middle East (Al-Hassan & Hill, 1986), in ancient Mexico (Langenscheidt, 1986); medieval Europe (Agricola, 1556/1912); California in the 1840s (Bailey & Everhart, 1964); and present-day Indonesia (Paddock, 2019). Mercury has been used to recover gold by amalgamation with mercury for centuries (Ahern, 2016; Fernández-Lozano et al., 2021).

The most important present-day use of mercury world-wide is for small-scale alluvial gold mining (United Nations Environment Programme, 2017). Other uses include: auto switches, batteries, chlor-alkali production, dental amalgam, explosives, fluorescent lamps, light-up toys, medical equipment, medicines, mirror-backing, and neon lights. Therefore, since cinnabar was mined and retorted in the past, and none of the above uses existed in the past, it is logical to conclude that mercury mined in the past had but one use-amalgamation of alluvial gold.

Alluvial gold is known to have been the main source of gold for ancient man and provided two-thirds of the gold ever produced (Boyle, 1979; Marsden & House, 2006). In Peru, alluvial gold deposits are widespread; however, the most well-known districts include Marañon in northeastern Peru, Rio Huallaga in east-central Peru, and Madre de Dios in southeastern Peru (Noble & Vidal, 1994; Atlas, 1999). These alluvial gold sources likely provided much of the gold used by Atahualpa as ransom for his release from the Spanish before his execution in 1533.

Peru was the leading gold producer in Latin America in 2018 and has produced metals for thousands of years (Burger & Gordon, 1998). For example, gold foils and gold workers tools were reported from Waywanka, a site dated 6000 - 1800 BCE (Grossman, 2013). In 2018, Peru's large-scale open-pit gold mines produced 123,767 kg of gold using cyanide and 18,875 kg of gold were produced from small-scale alluvial gold mines that used only gravity separation and mercury (Soto-Viruet, 2018). Therefore, since cyanide use only dates to 1880s, mercury amalgamation must be considered as the indigenous mining technology that produced industrial amounts of gold in ancient Peru.

2. Gold Mining Methods

Even though alluvial gold is widely acknowledged as a source of pre-contact gold, Saenz & Martinon-Torres (2011) indicate that little is known about gold mining methods in the past. However, Charles Lyell's (1830) Principle of Uniformitarianism or "The Present is Key to the Past" leads to understanding pre-contact gold mining by study of gold mining methods that are used today.

For example, in California in the 1850s, the importance of mercury in alluvial gold mining is indicated by the production of approximately 26,000,000 pounds (or 342,000 seventy-six-pound flasks) of mercury from New Almaden and other California mercury mines. This mercury was essential for amalgamation of alluvial gold produced from hydraulic mining during the California Gold Rush in 1849 (Davis, 1957; Bailey & Everhart, 1964; Bailey et al., 1973; Lanyon & Bulmore, 1967; Alpers et al., 2005). Similarly, mercury produced from Alaskan cinnabar mines was used for the Klondike Gold Rush in 1896 (National Park Service, 2019). Mercury is used today to produce alluvial gold in Brazil, Colombia, Ecuador, Ghana, Indonesia, Peru, Venezuela, and many other countries.

Present-day gold mining methods are key to gold mining in the past. For example, mercury amalgamation, which is used widely today in Peru, was also used to amalgamate placer gold at the ancient Roman gold mines in Spain (Fernández-Lozano et al., 2021). Specifically, industrial amounts of gold are produced in only two ways: 1) gravity separation, first by washing and then addition of mercury (amalgamation) and 2) cyanide (Craig et al., 2001). Gravity separation is the oldest method and utilizes the high specific gravity of the gold (~19) first in water and then with mercury. Sparse native gold found in streams (Petersen, 1970/2010, Tables 2, 3) could easily be removed by hand or, as in the ancient Andes, washing in water using a wooden gold pan or "*batea*" provided a concentrate of the fine-grained, heavier, gold-bearing sediment. Lighter material was washed out of the gold pan. The gold flakes or "*chispitas*" which are mm-sized and smaller, can only be efficiently recovered from the washed mineral separate using the ages-old method of mercury amalgamation. This begins with initial gravity separation by washing the gold-bearing sediment to produce a "pay dirt" concentrate of black sand or "*arena negra*" that includes the mm-sized and smaller gold flakes as well as apatite, magnetite, zircon, and other heavy minerals. Mercury is then added to the heavy-mineral concentrate and selectively removes only the gold. Then, this silvery, gold-mercury amalgam clot is squeezed through a cloth to recover excess mercury. Finally, this amalgam is burned or "*refogado*" to volatilize the remaining mercury. This leaves a sponge-textured anthropogenic gold "nugget" that could then be used for artifact production. To extract a given amount of alluvial gold, approximately twice as much mercury is required (Roskill, 1990; Cánepa, 2005).

Gravity separation techniques include the legendary Golden Fleece, as well as other variances that use carpet, sheep or other animal skins, and rely on the high specific gravity of gold to concentrate the gold in water (Healy, 1979). Another is the *aventadero* method that uses wind to separate the heavier gold from the lighter minerals, much like grain is separated from chaff (Petersen, 1970/2010). In Chocó, Colombia, plant juices added to water are used in place of mercury to concentrate the gold (Brooks et al., 2015) and in the Philippines, borax is used as a flux, to concentrate the heavier gold in the bottom of a heated crucible (Appel & Na-Oy, 2012).

Cyanide is the newer and more efficient method; however, its use only dates to the 1880s. Metals such as gold and silver are removed in solution from the crushed ore from large-scale, hard-rock porphyry (Au-Cu-Ag) mines. In precontact Peru, surficial outcrops of porphyry ores would have provided a gold-copper-silver alloy known as "*tumbaga*", which, through depletion gilding, would have resulted in enhanced surficial gold (Petersen, 1970/2010).

As an example of the importance of cyanide in mining, alluvial gold was discovered in Aruba in 1824. The gold was successfully recovered from alluvial and vein deposits using crushing, gravity separation, and mercury amalgamation until ~1880 when profits declined and mining ceased. Then, in 1897 the cyanide method was introduced, mining resumed profitably, and continued until 1916 (Gold Mine Ranch, 2021).

3. Previous Work

The enigma of pre-contact gold production in the ancient Andes was first addressed by the scholar Márques (1590) who said "*Lavaban la tierra en bateas de madera hasta obtener un residuo que contenía el oro. Los indios son más expertos para sacar el oro por ser naturales de este tierra así por la experiencia que ellos tenian como por la noticia de sus antepasados cuya voz corre en ellos.*" [They wash the sediments in wooden gold pans until a gold-bearing concentrate is obtained. The indigenous people are experts at getting gold because they are native to these lands and because the experience of their ancestors guides them.] Historian Garcilaso de la Vega wrote that "Gold was gathered by the Incas from the streams….no idea of the virtues of mercury" (Prescott, 1847/2005). However, while it is certain that ancient Andean gold was produced from alluvial sources, de la Vega's comment regarding mercury is equivocal:

- Given, the tons of gold mined and used for artifacts such as backflaps, crowns, and masks that were produced in pre-contact Peru and the availability of cinnabar-mercury occurrences, Posnansky (1945/1957) proposed the use of cinnabar as a source of mercury for amalgamation of the fine-grained alluvial gold in the ancient Andes.
- Larco Hoyle (1945/2001) wrote that "*...el beneficio de oro es todavía primitivo…incluyendo el empleo del azogue, que fue usado desde muy remota antigüedad.*" [...gold mining is still primitive…including the use of mercury which was used since very ancient times.] Mercury is sold as *azogue* (from the Arabic "*azzáuq*" or quicksilver, or from *agogae* indicating where gold was washed and recovered at Las Médulas, the ancient Roman gold mines in Spain) which was the word used for mercury produced at the Almaden mercury mine during the Moorish occupation of Spain and suggests Spanish origin for the mercury. In the present-day small-scale mining areas in Peru, mercury or "mercurio" is also be sold with a brand name suggestive of the supposedly superior Spanish commodity, for example, "Mercurio El Español" (Brooks et al., 2007).
- Cabrera la Rosa (1954) said: "*Asimismo es posible suponer que los peruanos de aquellas tierras conocián, ya en épocas remotas, el método de la amalgamación, empleando para ello el azogue que lograban obtener del cinabrio cuyas menas existián en Buldibuyo.*" [It is possible that ancient Peruvians knew about the use of mercury amalgamation in ancient time and they used mercury obtained from cinnabar ore found near Buldibuyo.] Ravines (1978) refined Cabrera la Rosa's location and indicated that "…*azogue se encuentra en Buldibuyo al pie del gran nevado de Pelagatos.*" […mercury can be found

at Buldibuyo at the base of great snow-covered Pelegatos peak.]

- Petersen (1970/2010) sketched several ancient *quimbaletes* which are 1 - 2 m, 1-2 t, crescent-shaped stones that pulverize the gold-bearing ore as they are rocked back and forth on a stone base. Petersen (1970/2010, Figure 10) shows several *quimbalates* that were used in pre-contact Peru and also photographed a modern *quimbalete* (Petersen, 1970/2010, Figure 2) in use. Mercury is added to the watery slurry at the base and the weight and rocking movement of the *quimbalete* amalgamates the fine-grained gold and mercury. The amalgam is recovered for *refogado* and recovery of the gold (Atlas, 2000; Cánepa, 2005). Therefore, since mercury is used with the present-day *quimbalete*, it is logical to conclude that mercury was available and similarly used for gold amalgamation in the past using the ancient *quimbaletes*.
- Petersen (1970/2010) wrote "…data suggest that mercury was retorted from cinnabar" and his spectrographic analyses of alluvial gold (Petersen, 1970/2010, Table 2) and artifact gold (Petersen 1970/2010, Table 18) were, respectively, high (0.1-1%) in mercury and low (<0.01%) in mercury. This is consistent with amalgamation and lowering the initial high mercury content of the alluvial gold by the *refogado* process.
- ICP (Inductively Coupled Plasma) analyses of gold composition showed that similarly low levels of mercury (<20 ppm Hg) in pre-contact gold artifacts and modern *refogado* gold, where mercury is used, are consistent with amalgamation of alluvial gold in the past (Brooks et al., 2013).

With the exception of mercury found in an ancient Maya tomb (Pendergast, 1982), native mercury has rarely been reported in the archaeological record. However, this does not mean that it wasn't geologically available (Roberts & Irving, 1957) and used. Given, that the use of mercury in gold processing is dissipative, then the tons of gold produced in pre-contact Peru is the hard evidence for amalgamation and is consistent with the above data. Peru produced 16-22 tons of gold annually from small-scale alluvial gold mines during 2007-2011, mainly in Madre de Dios, using mercury amalgamation (Gurmendi, 2012). And today, Peru produces ~1.5 tons of gold per month from small-scale alluvial mines that use the ages-old technique of gravity separation and mercury amalgamation (Cánepa, 2005; Brooks et al., 2007; Ahern, 2016; Chauvin, 2018; Soto-Viruet, 2018). From ancient-to-modern time in Peru and elsewhere, the primary use of mercury has been for small-scale alluvial gold mining.

4. Mercury and Human Health

In the present-day small-scale gold mining areas in Colombia, Peru, and other countries where mercury is used to amalgamate gold, the dissipative *refogado* process releases toxic mercury vapor that severely affects the brain, nervous system, kidneys, and other organs (CDC, n.d.). Gold workers in Antioquia, Colombia who are exposed to mercury vapors have classic mercury poisoning symptoms that include depression, kidney problems, and trembling (Webster, 2012).

Knowledge of the effects of mercury toxicity; however, is not new. Cinnabar is toxic (Sax, 1984; Brown, 2001) and was used as a preservative, for example, in ancient Hellenistic burials (Maravelaki-Kalaitzaki & Kallithrakis-Kontos, 2003) and at the ~7000 BC archaeological site of Çatalhöyük, near the mercury district of Konya, Türkiye (Barnes & Bailey, 1972). Cinnabar and hematite pigment use dates to 5300 BC in Spain (Domingo et al., 2012). Cinnabar workers in the ancient world were advised to wear a mask to prevent inhalation of the dust (Pliny the Elder, 55 AD) which was a very serious health hazard. Agricola (1556/1912) warned retort workers to avoid breathing mercury fumes that were known to cause loose teeth and Barba (1640/1923) warned that "mercury would pass through flesh and the hardest bone." Mercury was available in colonial Peru and was used for silver amalgamation. In Lima, it was also sold as a cure for syphilis; however, it caused salivation, dehydration, and eventually destroyed the jawbone without actually curing the disease (De Peralta, 2018).

In pre-contact Peru cinnabar mining and use of mercury for amalgamation may be inferred from similar health warnings regarding toxic cinnabar dust and mercury vapors. The nervous system, in particular, was affected and resulted in "*…el temblar y perder los sentidos*", […shaking and loss of the senses] therefore, cinnabar mining was prohibited by the Inca and its uses were forgotten only to be revived in 1567 by the Europeans (Larco Hoyle, 1945/2001). Exposure to toxic cinnabar dust and mercury vapors would have occurred during: 1) firesetting and cinnabar mining, 2) retorting cinnabar to obtain mercury, and 3) during the *refogado* process to produce gold. The Inca health warnings therefore indicate that cinnabar was mined, retorted, and mercury was used before the arrival of the Europeans.

5. Map Compilation

Mercury occurrences are known widely in South America and Mexico: Bolivia (Barba, 1640/1923; Ahlfeld & Schneider-Scherbina, 1964), Chile (McAllister et al., 1950), Colombia (Wilson, 1941; Lozano, 1987; Brooks, 2014), Ecuador (Truhan et al., 2005), and Peru (Arana, 1901; Garbín, 1904; Yates et al., 1955; Petersen, 1970/2010; Giles, n.d.). The most well-known occurrences include Huancavelica and Chonta, Peru (Arana, 1901; Garbín, 1904; Cobbing et al., 1996); Aranzazu (Nueva Esperanza) and El Cinabrio, Colombia (Singewald, 1950; Buitrago & Buenaventura, 1975; Brooks, 2014); and Azogues, Ecuador (Brooks, 2018). Mercury occurrences are also known in Queretaro, Mexico (Langenscheidt, 1986; Consejo de Recursos Minerales, 1992) and in Central America (Roberts & Irving, 1957). Herein, the term "occurrence" is used to indicate any geochemical anomaly of cinnabar and includes mines as well. The crustal average for mercury in igneous rocks is 0.08 ppm and for sedimentary rocks it is 0.03 - 0.4 ppm (Turekian & Wedepohl, 1961).

Over 3000 flasks of mercury were produced annually throughout the 1960s at

Huancavelica, the most well-known cinnabar-mercury occurrence in Peru (Arana, 1901; Whitaker, 1941; Yates et al., 1955; Roskill, 1990; Brown, 2001). And, in the 1840s mercury production also took place at Chonta (Garbín, 1904; Deustua, 2010). Therefore, a map showing these and other occurrences is basic to establishing the availability of this mineral resource in Peru, whether used for pigments, as a source of cinnabar for retorting mercury, or later colonial silver amalgamation. A map is also important for evaluation of point sources of mercury for present-day environmental studies.

Peruvian mineral resource maps are available for gold, copper, silver, and lead-zinc occurrences, but not cinnabar-mercury (Atlas, 1999); however, approximately 20 cinnabar-mercury occurrences are listed by Petersen (1970/2010). Many of these occurrences might be called districts because they include numerous mines and workings, such as the 10 mines at Chonta (Garbín, 1904). And, in most cases, since only geographic names were given, and not latitude and longitude, the locations are approximate. Locations were compiled (**Figure 1**) along with data from additional reports, some unpublished, and maps (Vercelli et al., 1977; Cobbing et al., 1996) from the Instituto Geológico Minero y Metalúrgico (INGEMMET), Lima.

Some of the cinnabar occurrences may have initially been ancient mines for pigments, native mercury, or other metals and have now been obscured or overprinted by modern mining. There is no present-day mercury production in Peru from the occurrences shown on **Figure 1**. However, mercury is produced as a byproduct from treatment of porphyry copper-gold ores with cyanide from mines such as Pierina and Yanacocha. However, because of global environmental and human health considerations, Peru's byproduct mercury is exported for treatment and retirement (Brooks et al., 2007; Ahern, 2016).

Buldibuyo/Pelagatos/Pampas (2) site visit—Cabrera la Rosa (1954) indicated a cinnabar occurrence near Buldibuyo. Examination of the geologic report for the area did not list a mercury occurrence (Balarezo, n.d.); however, the report by Ravines (1978) did include "Buldibuyo" as being near Pelagatos in central Peru, and near the village of Pampas. This occurrence is important given the specific geographic reference to "Buldibuyo" that was provided by both Cabrera la Rosa (1954) and Ravines (1978). Additionally, it is near Pataz where pre-Inca and Inca alluvial gold mining has been documented (Zarate, 2006). On **Figure 1** this occurrence is indicated as Buldibuyo/Pelagatos/Pampas.

After leaving Pampas along a road paralleling Lago Pelagatos, samples with cinnabar were taken at a northeast-trending fault with abundant rusty water and pyrite. An outcrop with cinnabar was found along this fault that extended for several kilometers (**Figure 2**). The fault was iron-stained and rusty water drained from the fault. Pyrite was also found along the fault and decomposition of the pyrite is the likely source of the rust-stained water. Two samples contained 24-82 ppm Hg (**Table 1**) and are above the crustal average of 0.08 ppm Hg (Turekian & Wedepohl, 1961). Tungsten and other large-scale mining in the area limited

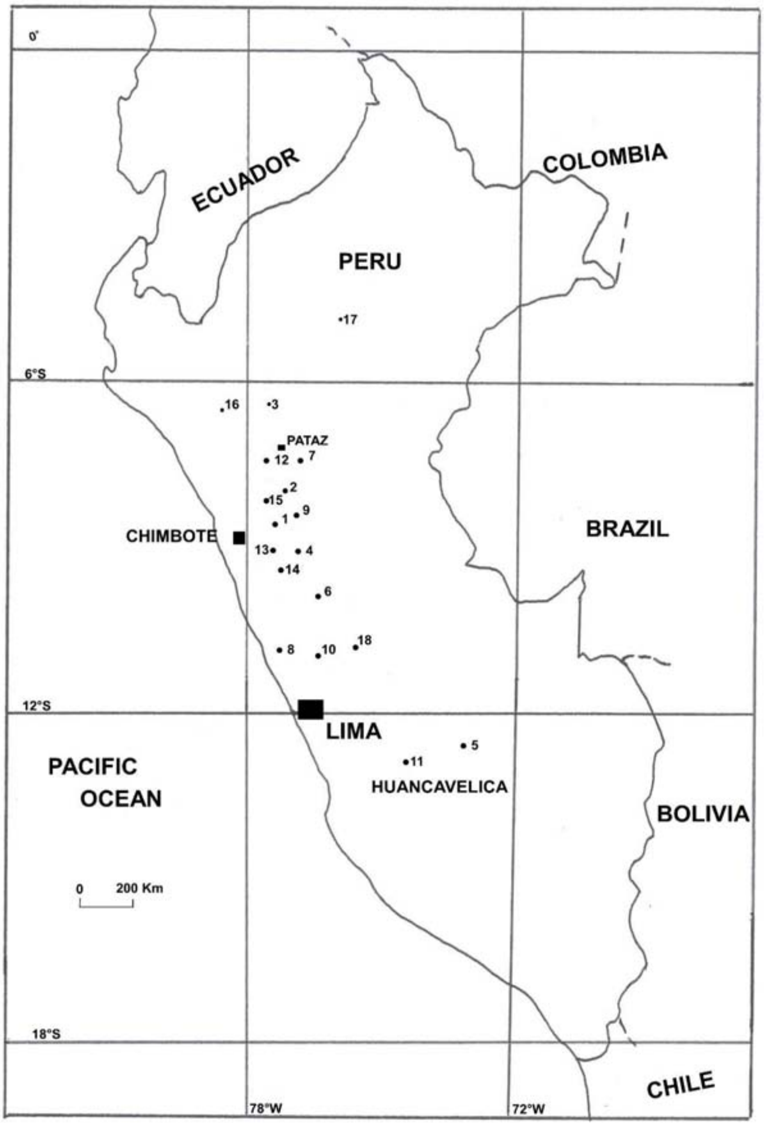

1—Baños de Jesus (BañosTermales de Monterrey?), 9˚32'S/77˚32'W (Ravines, 1978); 2—Buldibuyo/Pelagatos/Pampas, 8˚07'S/77˚23'W (Cabrera La Rosa, 1954; Ravines, 1978); 3—Chachapoyas (Sonche?), 6˚13´S/77˚52´W (Bolétin, 1900; Petersen, 1970/2010; Ravines, 1978; Deustua, 2010). "*Pinturasrupestre de Pollurua…color rojoocre*" [Pollura rock art....color of red ochre] may indicate cinnabar as pigment; 4—Chonta/Huallaca/Queropalca, 12˚38'S/74˚26'W (Petersen, 1970/2010; more than 15 named mines are noted at Queropalca by Garbín, 1904; Giles, n.d.); 5—Chuschi, 13˚35'S/74˚21'W (Petersen, 1970/2010); 6—Cuipan/Cuypan/Quipán, 10˚34'S/76˚29'W (cinnabar was taken from "*bocaminas y socavonesantiguos*" [mine openings and ancient adits] at Cuipan which is ~30 - 37 km northwest from Cerro de Pasco towards Yanahuanca, Garbín, 1904; Giles, n.d.; Petersen, 1970/2010; INGEMMET, 1999); 7—Huacrachuco, 8˚30'S/77˚04'W (Petersen, 1970/2010); 8—Huara, 11˚06'S/77˚36'W (Giles, n.d.); 9—Huaraz, 9˚31'S/77˚31'W (Petersen, 1970/2010); 10—Huarochiri, 11˚50'S/76˚22'W (Petersen 1970/2010); 11—Huancavelica/Villa Rica de Oropesa/Santa Barbara, 12˚47'S/74˚54'W (Arana, 1901; Yates et al., 1955; Petersen, 1970/2010; Brown, 2001; locations and descriptions of other mines and prospects in the region that include: Camarada, Excelsior, Carniceria, Azulcocha, ChaqaOreco/Ventanilla 7, Huajoto, Torres Orgo, San Antonio, and Pequeña are given in INGEMMET, 1999); 12—Paccha, 7˚59'S/77˚42'W (Petersen, 1970/2010); 13—Pampas, 9˚40'S/77˚49'W (Petersen, 1970/2010); 14—Punabamba, 9˚31'S/77˚31'W (Petersen, 1970/2010); 15—Santa, 9˚04'S/78˚35'W (Petersen, 1970/2010); 16—Santa Apolonia, 7˚09'S/78˚31'W (Petersen, 1970/2010); 17—Santa Cruz, 5˚33'S/75˚48'W (Petersen, 1970/2010); 18—Yauli, 11˚40'S/76˚05'W (Petersen, 1970/2010); The following occurrences are not shown on the map: 19—Cerro Azoguines, 15˚45'S/70˚01'W (Petersen, 1970/2010; INGEMMET, 1999; Diggings, n.d.); 20—Carachugo/Cajamarca, 7˚09'S/78˚30'W (INGEMMET, 1999); 21—Cangallo/Minascucho/Chauschi, 13˚37'S/74˚08'W (INGEMMET, 1999)

Figure 1. Approximate locations of cinnabar-mercury occurrences in Peru.

Figure 2. Samples of cinnabar were taken at northeast-trending fault along road that parallels Lago Pelagatos. The rust-stained water is from the decomposition of pyrite associated with cinnabar.

Table 1. ICP data for Pelagatos and Chonta cinnabar-mercury occurrences, Peru.

	PE181	PE182	PE191	PE192	PE193	PE194	PE196	PE197
Au (0.003)	0.008	0.007	0.01	0.004	0.006	0.018	0.072	0.010
Ag (0.2)	<0.2	<0.2	7.6	24.9	10	18.8	24.6	199
As (2.0)	27	7	2002	2178	87	84	824	6391
Ca (100.0)	3948	13165	199	263	<100	<100	446	<100
Cd (0.5)	<0.5	<0.5	0.9	0.7	<0.5	<0.5	0.6	<109.8
Cr (1.0)	563	237	16	14	11	16	21	4
Cu (1.0)	11	14	34	28	20	23	44	97
Fe (100)	14,306	6029	175,434	76,827	350,000	114,282	37,609	335,325
Hg (0.5)	82.9	24.9	13.1	11.9	10.7	>1000	>1000	93.6
La (10)	<10	<10	<10	<10	<10	<10	<10	<10
Mg (100.0)	2759	3483	154	116	<100	102	232	<100
Mn (5.0)	108	51	56	89	43	109	102	24
Mo (1.0)	4	1	2	3	<1	2	2	<1
Ni (1.0)	15	20	5	8	5	9	12	6
P (10)	295	105	565	216	22	25	76	17
Pb (3.0)	37	5	4016	6394	665	370	134	15,535
S (100)	904	244	6928	7619	>100,000	>100,000	31,977	>100,000

Continued

Sb (3.0)	6	3	174	248	77	23	21	367
Se (5.0)	<5	<5	<5	<5	<5	<5	<5	199
Th (10.0)	<10	<10	<10	<10	<10	<10	<10	<10
Tl (5.0)	<5	<5	<5	<5	<5	<5	<5	<5
U (8.0)	<8	<8	<8	<8	20	<8	<8	17
V (1.0)	<1	7	73	47	1	2	2	<1
W (3.0)	<3	<3	<3	<3	<3	<3	<3	<3
Zn (1.0)	5	5	339	201	36	31	72	9503

Multi-element ICP analyses in parts per million (detection limit given to right of element, in parentheses, Au-fire-assay); American Assay, Sparks, NV [ICP-2A024-Pelagatos SP0124038; Chonta SP0130401]. Sample Descriptions: PE181 [0192625/9095652 UTM] Pelagatos, dark fg quartzite, spot sample along road parallel to lake, cinnabar exposed along N 30˚ E fault in roadcut, abundant pyrite and Fe-stained water. PE182 [0192625/9095652 UTM] Pelagatos, dark fg quartzite, area sample along road parallel to lake, cinnabar exposed along N 30˚ fault in roadcut, abundant pyrite and Fe-stained water. PE191 [298130/8883304 UTM] Chonta, altered, quartzite, clay, along road at first main adit, area sample of 20 m wide breccia zone, altered with Fe stain. PE192 [298130/8883304 UTM] Chonta, at adit, area sample, vuggy, Fe stain. PE193 [298130/8883304 UTM] Chonta, at adit, float sample, dark, with pyrite. PE194 [738108/4293829 UTM] Chonta, quartzite, mine waste, with cinnabar on surface. PE196 [738108/4293829 UTM] Chonta, roadside, spot sample with cinnabar and pyrite. PE197 [738108/4293829 UTM] Chonta, at mine near plant, spot sample with abundant pyrite.

further access and likely eliminated or overprinted any traces of ancient mines.

Chonta/Huallaca/Queropalca (4) site visits—Chonta and Queropalca (Garbín, 1904; Giles, n.d.) may be accessed by a well-marked dirt road from Huallanca, to La Unión, and Baños or from Huánuco. Chonta was supposedly "discovered" upon orders from Spain in 1756 to find new sources of mercury to be used for colonial silver amalgamation. However, it is very likely that occurrences such as Chonta or Palcas, which is near Huancavelica, were first worked by pre-Inca people as a source of vermilion or *vermellón* pigment (Arana, 1901) as well as native mercury—similarly, the early use of cinnabar as a red pigment by the Ohlone people in California led to the "discovery" of the New Almaden mercury mines in California by Spanish explorers (Lanyon & Bulmore, 1967; Boulland & Boudreault, 2006).

In the 1840s, there were over 2000 miners and more than 20 individual mines at Chonta (**Figure 3**). There were 11 retorts and fuels included locally available coal, peat, and a grass called *ichu*. Water for condensers came from a nearby lagoon, Chonta Cocha. The mines produced 8-10 flasks (one flask contains ~76 pounds of mercury) of mercury per day. The grass roofs (*ichu*) of the buildings collected droplets of mercury lost during retorting (Garbín, 1904) and some of the buildings still remain (**Figure 4**).

At Chonta "*trabajos antiguos*" [ancient workings] likely indicates pre-contact cinnabar mining; however, it is unclear as to the exact location or how old these workings might be. Similarly, "…*bocaminas y socavones antiguos*" […mine

Figure 3. One of several adits at Chonta, note high-angle structure at entry.

Figure 4. Buildings and mine tailings at Chonta, smelter stack in middle-distance with ground chimney and stack to right.

opening and adits] likely indicate pre-contact mining at Cuipan (Cuypan, Quipan) ~30 km from Cerro de Pasco towards Yanahuanca (Garbín, 1904; Giles, n.d.). However, samples from a small exploration pit, and surely not the mine referenced by Garbín (1904), indicated only low gold and no mercury values (**Figure 5**, **Table 2**). Chonta closed in 1843; however, not because the ore was exhausted, but because of opportunities for miners willing to immigrate and

Figure 5. Exploration pit at Cuipan, contact between limestone (left) and dacite (right).

Table 2. ICP data for Cuipan exploration pit, Peru.

	B221	B222	B223
Au (0.003)	0.026	0.008	0.007
Ag (0.2)	0.8	<0.2	0.2
As (2.0)	11	3	34
Ca (100.0)	226,235	214,049	195,414
Cd (0.5)	70	>250	>250
Cr (1.0)	5	2	7
Cu (1.0)	3	2	<1
Fe (100)	6521	29,714	89,506
Hg (0.5)	<0.5	<0.5	<0.5
La (10)	<10	<10	<10
Mg (100.0)	92,221	87,979	79,237
Mn (5.0)	164	1266	3321
Mo (1.0)	1	<1	5
Ni (1.0)	1	4	4
P (10)	75	59	287
Pb (3.0)	14	7	195
S (100)	526	241	423
Sb (3.0)	<3	<3	<3
Se (5.0)	<5	<5	<5

Continued

Th (10.0)	<10	<10	17
Tl (5.0)	<5	<5	<5
U (8.0)	10	8	15
V (1.0)	15	8	22
W (3.0)	<3	<3	<3
Zn (1.0)	704	1841	3144

Multi-element ICP analyses in parts per million (detection limit given to right of element, in parentheses); American Assay, Sparks, NV [ICP-2A024-SP0143538]. Sample Note: B220-223 [10˚34.162 S/76˚29.373 W] Cuipan, area sample at 4 m × 2 m shallow pit, Fe-stained, west strike, limestone-dacite contact, >14300 ft.

work at the mercury mines at New Almaden, California (Garbín, 1904; Giles, n.d.). New Almaden mercury would be needed for the 1849 California Gold Rush.

Samples from Chonta for this reconnaissance contained > 1000 ppm Hg; 10 - 199 ppm Ag; 84 - 6391 ppm As; 21 - 367 ppm Sb, and 31 - 9503 ppm Zn. Gold values are 0.01 - 0.07 ppm, but may increase with depth (**Table 1**). These elements are all above background and indicate further study focused on silver and gold in association with mercury (Turekian & Wedepohl, 1961; Noble & Vidal, 1990). Specifically, the high arsenic is a pathfinder for gold and the high mercury content is an indicator of Pb-Zn-Ag ore (Rose et al., 1979). Chonta is an altered plagioclase-quartz dacite stock that intrudes sedimentary rocks of the Oyon and Casalpaca Formations (Cobbing et al., 1996). Minerals are hosted in quartzite and sedimentary rocks and include pyrite, sphalerite, galena, cinnabar, native mercury, and silver in mainly NS structures.

Queropalca is a polymetallic Au-Ag occurrence hosted in quartzites of the Chimu Formation that was supposedly "discovered" in 1736; however, there are several adits that indicate pre-contact mining. Evidence includes: dipping floors; with only daylight for work the adits were shallow; and the adits were spaced along the vein (**Figure 6(a)**). Mineralization is hosted in veins that are several meters wide and contain gold, pyrite, chalcopyrite, and copper. There were 15 named mines at Queropalca; however, production ended by 1894 (Garbín, 1904). It is important to indicate that mercury was used for amalgamation at Queropalca, likely from the mines at nearby Chonta, to treat the minerals. Exploration drilling showed several meters of gold-silver mineralization with values as high as 10 ppm Au, 1500 ppm Ag, and 0.35% Pb (Candente Gold Corp., 2009). A hot-spring was mapped in the area and this suggests a hot-spring Au-Ag exploration model for the district, especially given the high antimony and arsenic at Chonta (Berger, 1986; Candente Gold Corp., 2009). Surface samples from Queropalca for this study indicated as much as 6.4 ppm Au; >100 ppm Ag, 700 ppm Cu, >1600 ppm As, and 31 ppm Hg (**Figure 6(b)**, **Table 3**).

Mercury was also found at Huallanca but was not produced because of its

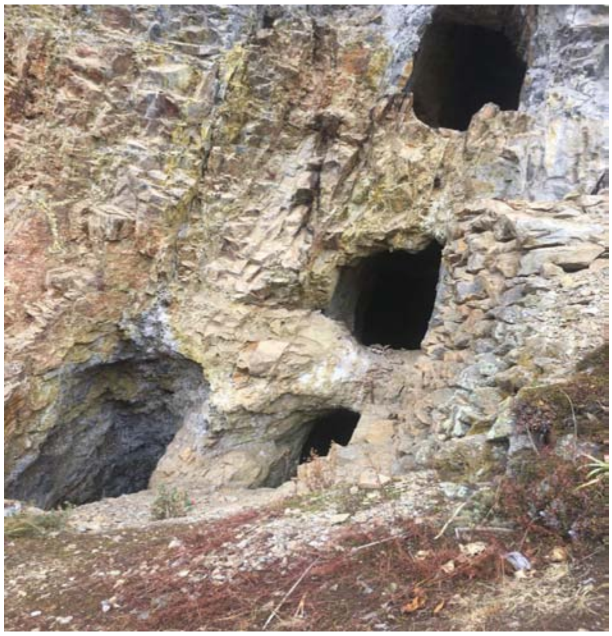

(a)

(b)

Figure 6. (a) Multiple adits at Queropalca, along steeply dipping vein in quartzite; (b) Queropalca sample B2210 with 6.44 ppm Au, >100 ppm Ag, and 31.8 ppm Hg (**Table 3**). Brassy chalcopyrite on left and white hot-spring travertine on right.

low-grade and limited extent (Arana, 1901). There are several mines at present-day Huallanca, for example Minera Santa Luisa, where mining dates to 1721 and gold, silver, and copper were produced from three veins. Pyrite, chalcopyrite, sphalerite, and copper minerals are reported from well-named mines such as Komstock and Eureka (Garbín, 1904).

Cerro Azoguines site visit—This occurrence, also known as the Cerro Azoguines quicksilver mine, is a small adit east of Alto Puno, in southern Peru. It was found in ~1640 and produced mercury, cinnabar, and tetrahedrite; however, now it is inactive (Petersen, 1970/2010; INGEMMET, 1999; Diggings, n.d.).

Table 3. ICP data for Queropalca gold-silver occurrence, Peru.

	B224	B225	B226	B227	B228	B229	B2210	B2211	B2212
Au (0.003)	0.017	0.020	0.033	0.030	0.022	0.033	6.440	1.590	0.057
Ag (0.2)	0.3	0.3	0.3	9	1.2	5.5	>100	>100	1.1
As (2.0)	15	41	51	35	40	75	1666	1148	53
Ca (100.0)	1491	1434	633	626	662	1272	381	3744	1822
Cd (0.5)	2.7	1	<0.5	<0.5	<0.5	3.1	<0.5	2.5	3
Cr (1.0)	445	377	323	451	363	324	382	370	258
Cu (1.0)	6	4	4	44	7	8	372	702	8
Fe (100)	5799	6158	6395	5968	5632	5871	73,558	28,424	4926
Hg (0.5)	0.6	1.3	1.1	1.1	4.3	2.9	31.8	31.8	1.6
La (10)	<10	<10	<10	<10	<10	<10	<10	<10	<10
Mg (100.0)	599	565	203	103	114	433	<100	1524	745
Mn (5.0)	55	51	41	56	46	42	47	52	52
Mo (1.0)	2	2	<1	1	<1	1	1	<1	<1
Ni (1.0)	8	7	5	8	7	7	98	30	5
P (10)	12	30	47	12	13	12	30	28	16
Pb (3.0)	9	11	9	16	4	9	40	35	13
S (100)	369	516	478	930	1109	711	71,436	28,705	717
Sb (3.0)	<3	<3	<3	7	9	16	226	841	5
Se (5.0)	<5	<5	<5	<5	<5	<5	29	11	<5
Th (10.0)	<10	<10	<10	<10	<10	<10	20	11	<10
Tl (5.0)	<5	<5	<5	<5	<5	<5	<5	<5	<5
U (8.0)	<8	<8	<8	<8	<8	<8	<8	<8	<8
V (1.0)	<1	<1	<1	<1	<1	1	1	<1	<1
W (3.0)	7	<3	<3	<3	<3	<3	<3	<3	<3
Zn (1.0)	27	14	11	8	11	45	17	137	38

Multi-element ICP analyses in parts per million (detection limit given to right of element, in parentheses); American Assay, Sparks, NV [ICP-2A024-SP0143538]. Sample Note: B224-2212 [10˚10.115 S/76˚48.496 W] Queropalca area samples, veins with pyrite, chalcopyrite in quartzite, >12,500 ft.

The adit is small, bifurcated, and extends for only a few meters (**Figure 7**) into Miocene volcaniclastic rocks (Rodriguez Mejía et al., 2020). Samples indicate 3 - 45 ppm Hg, up to 400 ppm As, and minor Sb (**Table 4**).

<u>Apu Campana (Fe pigment) site visit</u>—Apu Campana, near Trujillo, is a pre-contact adit that was initially considered as a source for cinnabar and other minerals used by the Moche (Franco Jordán, 2012; Peruvian Times, 2012). Local inhabitants had identified the red mineral as mercury; however, analyses by

Figure 7. Adit at Cerro Azoguines quicksilver mine, Puno.

Table 4. ICP data for Cerro Azoguines cinnabar occurrence, Peru.

	AZ1	AZ2	AZ3	AZ4	AZ5	AZ6	AZ7	AZ8
Ag (0.2)	<0.2	0.3	0.9	0.5	0.3	0.3	0.4	<0.2
As (2.0)	27	92	441	184	135	118	149	72
Ca (100.0)	12,988	2038	1080	1271	1127	1048	1050	746
Cd (0.5)	<0.5	1.5	2.7	1.1	0.8	0.8	1.3	0.5
Cr (1.0)	188	152	82	96	49	88	138	202
Cu (1.0)	555	3664	1613	1279	1128	1072	1879	757
Fe (100)	8204	17,504	20,468	22,392	19,552	22,109	33,079	9702
Hg (0.5)	0.8	3.0	12.6	8.7	16.8	45.5	4.0	8.2
La (10)	<10	<10	<10	10	<10	11	<10	<10
Mg (100.0)	148	237	191	183	139	147	134	<100
Mn (5.0)	232	1047	1254	1358	1521	1158	938	564
Mo (1.0)	<1	1	2	<1	<1	<1	1	<1
Ni (1.0)	8	10	7	8	8	8	9	9
P (10)	100	236	289	335	314	342	255	175
Pb (3.0)	6	6	33	21	15	11	11	4
S (100)	<100	149	<100	<100	<100	<100	<100	<100
Sb (3.0)	<3	3	10	6	4	4	5	<3
Se (5.0)	<5	<5	<5	<5	<5	<5	<5	<5
Th (10.0)	<10	<10	<10	<10	<10	<10	<10	<10
Tl (5.0)	<5	<5	<5	<5	<5	<5	<5	<5

Continued

U (8.0)	<8	<8	<8	<8	<8	<8	<8	<8
V (1.0)	15	48	81	78	64	73	96	22
W (3.0)	<3	<3	<3	<3	<3	<3	<3	<3
Zn (1.0)	17	65	81	39	49	46	58	31

Multi-element ICP analyses in parts per million (detection limit given to right of element, in parentheses). American Assay, Sparks, NV [ICP-2A024-Cerro Azoguines SP0137487]. Sample Note: AZ1-8 [15˚45'S/78˚30'W] alt. volcanic and volcaniclastic rocks.

Prieto et al. (2016) showed no cinnabar but rather the iron mineral hematite which was also used as an ancient red pigment (Petersen, 1970/2010). Hematite mining for pigment use on pottery dates to 2000 years ago in Peru (Vaughan et al., 2007). Geochemical data from samples taken during a reconnaissance of the Apu Campana adit for this study similarly show no mercury (<0.5 ppm Hg; **Table 5**).

6. Retorting Mercury from Cinnabar

Some native mercury may have been obtained from the cinnabar outcrop; however, retorting mercury is a straightforward process that requires cinnabar ore, retorts, fuel, water, and a condenser to trap and cool the volatilized mercury vapors. The oldest mercury retort dates to 8000 years ago in the ancient Konya mercury district in Türkiye and it consisted of a large block of marble upon which the ore was placed along with charcoal fuel. A large clay bowl cooled and condensed the mercury vapors while allowing the sulfur vapor to escape through a chimney made of ceramic tubes (Barnes & Bailey, 1972). Mercury was used to exploit the placer gold deposits in the region ~7000 years ago (Healy, 1979).

Other retorts include rows of double ceramic pots as shown in Agricola (1556/1912, Book IX, p. 427) and a pre-contact double-ceramic mercury retort from Sierra Gorda, Queretaro, Mexico (Langenscheidt, 1986) where there are many ancient cinnabar mines and retorting mercury dates to the 10th century BC (Consejo de Recursos Minerales, 1992). Descriptions and sketches of a variety of mercury retorts from China, Germany, and Mexico were compiled by Craddock (1995). Ancient retorts were known at Huancavelica (Rivero & Tschudi, 1853) and at Chonta, a chimney and buildings that housed retorts and condensers in the 1840s still remain (**Figure 4**).

At New Almaden, California the retorts consisted of whaling oil-try pots that were inverted over the cinnabar ore, sealed, and then fired with wood. The cinnabar inside the metal pot was heated, the mercury volatilized, the vapors cooled and condensed, resulting in mercury (Boulland & Boudreault, 2006). In Indonesia, up to a ton of mercury can be produced daily, using locally available cinnabar, from a simple, backyard wood-fired retort. This mercury is then sold directly to local small-scale gold miners or exported (Paddock, 2019).

Droplets of native mercury could be obtained directly from the outcrop or

Table 5. ICP data for Apu Campana/Portachuelo Fe pigment occurrence, Peru.

	AC1	AC2	AC3	AC4	AC5	AC6	AC7	AC8
Ag (0.2)	0.8	0.7	0.6	0.7	0.6	0.6	0.7	0.4
As (2.0)	5	3	11	2	<2	6	11	49
Ca (100.0)	2115	2336	2507	2275	1688	684	2372	1508
Cd (0.5)	<0.5	<0.5	<0.5	<0.5	<0.5	<0.5	<0.5	0.8
Cr (1.0)	179	236	226	253	246	116	247	96
Cu (1.0)	589	1191	2927	2430	2944	1430	1299	2457
Fe (100)	25,925	23,543	35,694	25,687	28,804	23,837	25,707	30,646
Hg (0.5)	<0.5	<0.5	<0.5	<0.5	<0.5	<0.5	<0.5	<0.5
La (10)	<10	<10	<10	<10	<10	<10	<10	<10
Mg (100.0)	7919	6193	5479	5930	6677	1810	5696	6684
Mn (5.0)	442	396	509	570	694	217	466	776
Mo (1.0)	1	3	8	3	3	23	14	6
Ni (1.0)	10	12	10	11	12	5	10	6
P (10)	582	574	612	473	363	148	836	572
Pb (3.0)	237	171	247	44	16	132	570	484
S (100)	<100	144	132	<100	149	127	161	<100
Sb (3.0)	<3	<3	<3	<3	<3	<3	<3	<3
Se (5.0)	<5	<5	<5	<5	<5	<5	<5	<5
Th (10.0)	<10	<10	<10	<10	<10	<10	<10	<10
Tl (5.0)	<5	<5	<5	<5	<5	<5	<5	<5
U (8.0)	<8	<8	<8	<8	<8	<8	<8	<8
V (1.0)	57	44	42	32	36	34	39	42
W (3.0)	<3	<3	<3	<3	<3	<3	<3	<3
Zn (1.0)	1212	448	370	231	338	389	416	448

Multi-element ICP analyses in parts per million (detection limit given to right of element, in parentheses); American Assay, Sparks, NV [ICP-2A024-Apu Campana SP0137017]. Sample Note: AC1-9 [7˚56'26"S/79˚07'59"W] ApuCampana/Portachuelo, coarse-grained, Fe-stained alt. granodiorite.

from hammering the ore and, though seldom used, cinnabar could be rubbed with vinegar in a copper mortar to obtain mercury (Takacs, 2000). However, only retorting would have provided the amounts of mercury needed to produce the tons of alluvial gold produced before the arrival of the Europeans.

Therefore, given the geological evidence for the regional availability of cinnabar-mercury occurrences and the widespread use of mercury for gold amalgamation in the past that continues to the present, it remains only to show how cinnabar could easily be retorted to provide mercury using materials readily available in the ancient world. A simple retort was modeled from the racks of double-ceramic retorts shown in Agricola (1556/1912, Book IX, p. 427) and a pre-contact double-ceramic mercury retort from Sierra Gorda, Queretaro, Mexico (Langenscheidt, 1986). This rudimentary process does not produce vermilion, only a sooty mercury-rich residue, and metallic mercury (**Figures 8-11**) that would have been collected and then used for ancient small-scale alluvial gold mining.

Figure 8. Cinnabar ore (~50 g).

Figure 9. Double-ceramic retort with clay seal, vent to right.

Figure 10. Retort in place with charcoal fuel (~600˚ F).

Figure 11. Mercury droplets in black mercury-rich residue along rim of ceramic retort. The blackened interior of a mercury smelter chimney at Karaburun, Türkiye had >400 ppm Hg (Brooks et al., 2017). At the retorts at New Almaden this black sooty residuewas scraped and removed to obtain additional mercury (Boulland & Boudreault, 2006).

7. Conclusion

Present day mining technology provides insight into pre-contact alluvial gold production in ancient Peru. References and data herein are also consistent with amalgamation in pre-contact Peru. Given that the use of cyanide dates only to the 1880s, the volume of gold produced in pre-contact Peru indicates ages-old amalgamation as key to past gold production. Availability of mercury is indicated by compilation of cinnabar-mercury occurrences and is important to the study of mineral resources and their uses in the ancient Andes. Huancavelica remains as the most well-known mercury occurrence, now followed by Chonta.

The availability of cinnabar-mercury is applicable to the study of mineral resource uses, as a source of red pigment (vermilion) and as a source of ore for mercury in pre-contact Peru. Of these, the use of mercury for gold amalgamation in the present and past helps to explain the indigenous technology that resulted in the incredible gold production that took place in ancient Peru before the arrival of the Europeans. In addition to ancient cinnabar mining at Huancavelica, there are references and evidence for ancient mine workings at Chonta, Cuipan, and Queropalca as well as pre-Inca gold mining at Pataz.

Some native mercury was available, for example at Huancavelica or Chonta; however, retorting cinnabar was a simple process that dates to ancient times worldwide. In Peru, retorting would have utilized readily available materials such as cinnabar, clay for the ceramic retorts, water for cooling, and fuels such as charcoal, coal, grass, or wood. Much as mercury is used today in Peru's small-scale alluvial gold mines in Madre de Dios or Marañon, in the past, mercury would have been sourced from the cinnabar occurrences in Peru, retorted, and used for pre-contact gold production.

Acknowledgements

Sincere thanks are expressed to Rolando Moreno, director of the INGEMMET library, in Lima for providing maps and geologic reports on mercury in Peru and to Sr. Christian Ormeño for security and transport in the field.

Conflicts of Interest

The author declares no conflicts of interest regarding the publication of this paper.

References

Agricola (1556/1912). *De Re Metallica* (638 p). Trans. by H. C. Hoover, & H. L. Hoover, Kessinger Publishing.

Ahern, N. (2016). Mercury in Gold Processing. In M. D. Adams (Ed.), *Gold Ore Processing* (2nd ed., pp. 753-766). Elsevier. https://doi.org/10.1016/B978-0-444-63658-4.00042-6

Ahlfeld, F., & Schneider-Scherbina, A. (1964). *Los Yacimientos Minerales y De Hidrocarburos de Bolivia* (388 p). La Paz, Ministerio de Minas y Petroleo, Departamento Nacional de Geología, Boletin No. 5 (Especial).

al-Hassan, A. Y., & Hill, D. R. (1986). *Islamic Technology: An Illustrated History* (304 p). Cambridge University Press.

Alpers, C. N., Hunerlach, M. P., May, J. T., & Hothem, R. L. (2005). *Mercury Contamination from Historical Gold Mining in California.* U.S. Geological Survey Fact Sheet 2005-3014 Version 1.1. https://pubs.usgs.gov/fs/2005/3014
https://doi.org/10.3133/fs20053014

Appel, P. W., & Na-Oy, L. (2012). The Borax Method of Gold Extraction for Small-Scale Miners. *Journal of Health and Pollution, 2,* 5-10.

Arana, P. P. (1901). *Las Minas de Azogue del Perú* (109 p). Imprenta El Lucero.

Atlas (1999). *Atlas of Minería y Energía en el Perú* (D. Hokama, ed., 111 p). Ministerio de Energía y Minas.

Atlas (2000). *Atlas de la Pequeña Minería en el Perú* (J. Charmot Sarmiento, ed., 88 p). Ministerio de Energía y Minas.

Bailey, E. H., & Everhart, D. L. (1964). *Geology and Quicksilver Deposits of the New Almaden District, Santa Clara County, California* (206 p). U.S. Geological Survey Professional Paper 360. https://doi.org/10.3133/pp360

Bailey, E. H., Clark, A. L., & Smith, R. H. (1973). Mercury. In D. A. Brobst, & W. P. Pratt (Eds.), *United States Mineral Resources* (pp. 401-414). U.S. Geological Survey Professional Paper 820.

Balarezo, A. (n.d.). *Croquis de Ubicación de Las Zonas Mineras de Parcoy y Buldibuyo. Lima.* Cooperación Minera Peruano Alemana, INGEMMET Archivo Tecnico, Codigo CG1794, Scale 1:1,000,000.

Barba, A. A. (1640/1923). *El Arte de los Metales*. Trans. by R. E. Douglass, & E. P. Mathewson, John Wiley & Sons.

Barnes, J. W., & Bailey, E. H. (1972). Turkey's Major Mercury Mine Today and How It was Mined 8000 Years Ago. *World Mining, 25,* 49-55.

Berger, B. R. (1986). Descriptive Model of Hot Spring Au-Ag, Model 25a. In D. P. Cox, & D. A. Singer (Eds.), *Mineral Deposit Models*. U.S. Geological Survey Bulletin 1693.

Bolétin (1900). Itinerario de los Viajes de Raimondi en el Perú. *Bolétin de la Sociedad Geográfica de Lima, 10,* 1-40.

Bonavia, D. (1985). *Mural Painting in Ancient PERU* (238 p). Indiana University Press.

Boulland, M., & Boudreault, A. (2006). *New Almaden* (225 p). Arcadia Publishing.

Boyle, R. W. (1979). The Geochemistry of Gold and Its Deposits. *Canadian Geological Survey Bulletin, 280,* 584 p.

Brooks, W. E. (2012). Ch. 2. Industrial Use of Mercury in the Ancient World. In M. S. Bank (Ed.), *Mercury in the Environment—Pattern and Process* (pp. 19-24). University of California Press. https://doi.org/10.1525/california/9780520271630.003.0002

Brooks, W. E. (2014). Colombia Mercury Inventory. *Geología Colombiana, 37,* 15-50.

Brooks, W. E. (2018). ICP Analyses from the Cinnabar-Mercury Occurrence at Azogues (Loma Guashon), Ecuador, Ancient Industrial Uses and Human Health Implications. *Archaeological Discovery, 6,* 38-51. https://doi.org/10.4236/ad.2018.61003

Brooks, W. E., Ozturk, H., & Cansu, Z. (2017). Amalgamation and Small-Scale Gold Mining at Ancient Sardis, Turkey. *Archaeological Discovery, 5,* 42-59. https://doi.org/10.4236/ad.2017.51003

Brooks, W. E., Piminchumo, V., Suarez, H., Jackson, J. C., & McGeehin, J. P. (2008). Mineral Pigments from Huaca Tacaynamo, Chan Chan, Northern Peru. *Bulletin de l'Institut Francais d'Études Andines, 37,* 441-450. https://doi.org/10.4000/bifea.2957

Brooks, W. E., Sandoval, E., Yepez, M., & Howard, H. (2007). *Peru Mercury Inventory 2006.* U.S. Geological Survey Open-File Report 2007-1252. http://pubs.usgs.gov/of/2007/1252/ https://doi.org/10.3133/ofr20071252

Brooks, W. E., Schwörbel, G., & Castillo, L. E. (2013). Ch. 10. Amalgamation and Small-Scale Gold Mining in the Ancient Andes. In N. Tripcevich, & K. J. Vaughn (Eds.), *Mining and Quarrying in the Ancient Andes, Interdisciplinary Contributions to Archaeology* (pp. 213-229). Springer Publishing. https://doi.org/10.1007/978-1-4614-5200-3_10

Brooks, W. E., Sierra, J. A., & Palacios, F. (2015). Green Gold—Dirty Gold, Tadó, Dept. Chocó, Colombia. *Natural Resources, 6,* 534-542. https://doi.org/10.4236/nr.2015.611051

Brown, K. W. (2001). Workers' Health and Colonial Mercury Mining at Huancavelica, Peru. *The Americas, 57,* 467-496. https://doi.org/10.1353/tam.2001.0030

Buitrago, C. J., & Buenaventura, J. (1975). *Ocurrencias Minerales en La Región Central del Departmento del Tolima* (837 p). INGEOMINAS Informe 1672, Bogotá.

Burger, R. L., & Gordon, R. B. (1998). Early Central Andean Metalworking from Mina Perdida, Peru. *Science, 282,* 1108-1111. https://doi.org/10.1126/science.282.5391.1108

Cabrera la Rosa, A. (1954). *Situación Actual de la Minería del Mercurio en el Perú* (pp. 3-12). Minería y Metalurgia, Madrid.

Candente Gold Corp. (2009). *Candente Gold Corporation Presentation-Oro Queropalca.* Candente Gold Corp. https://www.candentecopper.com/site/assets/files/5197/goldpropertiesapril2009.pdf

Cánepa, C. (2005). *Minería a Pequeña Escala en la Costa Sur Media del Perú* (62 p). Instituto Geológico Minero y Metalúrgico, INGEMMET Boletín 3, Serie E: Minería, Lima.

CDC (n.d.). *Mercury*. Center for Disease Control and Prevention. https://www.cdc.gov/niosh/topics/mercury/default.html

Chauvin, L. (2018). Pope Brings Environmental Crusade to Peru. *Washington Post,* 20 January, A8.

Cobbing, J., Sánchez, A., Martínez, W., & Zárate, H. (1996). *Geología de los Cuadrángulos de Huaraz, Recuay, La Unión, Chiquián y Yanahuanca* (281 p). INGEMMET Boletin n. 76, Serie A, Carta Geologíca Nacional.

Consejo de Recursos Minerales (1992). *Geological-Mining Monograph of the State of Queretaro* (108 p). Consejo de Recursos Minerales, Secretaria de Energia, Minas e Industria, Mexico, D. F., Publishing Number M4e.

Craddock, P. T. (1995). *Early Metal Mining and Production* (363 p). Smithsonian Institution Press.

Craig, J. R., Vaughan, D. J., and Skinner, B. J. (2001). *Resources of the Earth* (520 p). Prentice-Hall.

Davis, F. F. (1957). Mercury. In L. A. Wright (Ed.), *Mineral Commodities of California, State of California, Division of Mines Bulletin 176* (pp. 341-356).

De Peralta, K. K. (2018). *Dying to Heal, Women and Syphilis in Colonial Lima, Peru*. Nursing Clio. https://nursingclio.org

Deustua, J. E. (2010). Mercury (not Always Rising) and the Social Economy of Nineteenth-Century Peru. *Economía, 33,* 128-153. http://www.researchgate.net

Diggings (n.d.). *Cerro Azoguine Quicksilver Mercury Mine*. The Diggings. https://thediggings.com/mines/usgs10068939

Domingo, I., Garcia-Borja, P., & Rodán, C. (2012). Identification, Processing, and Use of Red Pigments (Hematite and Cinnabar) in the Early Neolitic (Spain). *Archaeometry, 54,* 868-892. https://doi.org/10.1111/j.1475-4754.2011.00650.x

Fernández-Lozano, J., Nnandong, A. N., Rivera, S., Esbrí, J. M., Carrasco, R. M., Pedraza, J., Bernardo-Sánchez, A., & Higueras, P. (2021). Uso de mercurio para el beneficio de yacimientos secundarios de oro en epoca romana. Realidad o ficción? *Geogaceta, 69,* 1-4. https://www.researchgate.net/publication/349685762

Franco Jordán, R. (2012). El Apu Campana, La Montaña Sagrada Moche. *Pueblo Continente, 23,* 292-307.

Garbín, L. (1904). Apuntes Sobre los Minerales de Huallanca, Chonta y Queropalca. *Boletin de la Sociedad de Ingenieros, VI,* 1-17.

Giles, C. F. (n.d.). *Minas de Mercurio Conocidas en el Peru* (3 p). INGEMMET Archivo Tecnico, Codigo 9921.

Gold Mine Ranch (2021). *The Gold Mine Ranch History*. https://www.thegoldmineranch.com/history

Grossman, J. (2013). The Waywanka Gold, New Chronometric Evidence. *Andean Past, 11,* 123-138.

Gurmendi, A. C. (2012). *The Mineral Industry of Peru*. U.S. Geological Survey 2012 Minerals Yearbook. https://minerals.usgs.gov/minerals/pubs/country/2012/myb3-2012-peru.pdf

Healy, J. F. (1979). Mining and Processing Gold Ores in the Ancient World. *Journal of Metals, 31,* 11-16. https://doi.org/10.1007/BF03354474

INGEMMET (1999). *Mercurio*. INGEMMET Archivo Tecnico, Codigo AO993.

Langenscheidt, A. (1986). Historia Minima de la Minería en la Sierra Gorda, Queretaro, Mexico. *Mineroamérica,* 24-29.

Lanyon, M., & Bulmore, L. (1967). *Cinnabar Hills, the Quicksilver Days of New Almaden* (128 p). Village Printers.

Larco Hoyle, R. (1945/2001). *Los Mochicas, Tomo II* (350 p). Museo Arqueologíco Rafael Larco Herrera, Pueblo Libre.

Lozano, H. (1987). Minerales de Mercurio. *Publicacciones Especial de Ingeominas, No. 1,* 275-293.

Maravelaki-Kalaitzaki, N., & Kallithrakis-Kontos, M. (2003). Cinnabar Find in Cretan Hellenistic Tombs, Preservative or Cosmetic Purpose. In *4th Symposium on Archaeometry*. Hellenic Society for Archaeometry. http://www.archaeometry.gr/eae/HSA

Márques, M. (1590). *Casa de Moneda, Banco de la Republica, Bogotá, explanation in a gold-mining diorama*. March 2012.

Marsden, J. O., & House, C. I. (2006). *The Chemistry of Gold Extraction* (275 p). Society of Mining, Metallurgy and Exploration.

McAllister, J. F., Flores, H., & Ruiz, C. (1950). *Quicksilver Deposits of Chile* (69 p). U.S. Geological Survey Bulletin 964-E.

National Park Service (2019). *Metals of the Gold Rush*. National Park Service. https://www.nps.gov/klse/learn/nature/geology.htm

Noble, D. C., & Vidal, C. E. (1990). Association of Silver with Mercury, Arsenic, and Antimony at the Huancavelica district, Peru. *Economic Geology, 85,* 1645-1650. https://doi.org/10.2113/gsecongeo.85.7.1645

Noble, D. C., & Vidal, C. E. (1994). Gold in Perú. *SEG Discovery, No. 17,* 1-13. https://doi.org/10.5382/SEGnews.1994-17.fea

Paddock, R. C. (2019). The Hidden Cost of Gold: Birth Defects and Brain Damage. *New York Times*. https://www.nytimes.com/2019/11/09/world/asia/indonesia-mercury-pollution-gold-mining.html

Pendergast, D. M. (1982). Ancient Maya Mercury. *Science, 217,* 533-535. https://doi.org/10.1126/science.217.4559.533

Peruvian Times (2012). Pre-Inca Cinnabar Mine Discovered in Trujillo. *Peruvian Times*. https://www.peruviantimes.com/22/pre-inca-cinnabar-mine-discovered-in-trujillo/16097

Petersen, G. (1970/2010). *Mining and Metallurgy in Ancient Perú* (90 p.). Trans. by W. E. Brooks, 2010, of Minería y Metalurgia en el Antiguo Perú, Arqueologicas 12, Museo Nacional de Antropología y Arqueología, Pueblo Libre, Lima. Geological Society of America Special Paper 467.

Posnansky, A. (1945/1957). *Tiahuanaco, La Cuna del Hombre Americano*. v. 1-II, 1945, New York; v. 3-4, Ministerio de Educación, 1957, La Paz, Bolivia.

Prescott, W. H. (1847/2005). *History of the Conquest of Peru* (537 p). Dover Publications.

Prieto, G., Wright, V., Burger, R., Cooke, C., Zeballos-Velasquez, E. L. Watanave, A., Suchomel, M. R., & Suescun, L. (2016). The Source, Processing and Use of Red Pigment Based on Hematite and Cinnabar at Gramalote, an Early Initial Period (1500-1200 cal. B.C.) Maritime Community, North Coast of Peru. *Journal of Archaeological Science Reports, 5,* 45-60. https://doi.org/10.1016/j.jasrep.2015.10.026

Ravines, R. (1978). *Tecnología Andina* (821 p). Instituto de Estudios Peruanos, Instituto de Investigación Tecnológica Industrial y de Normas Técnicas, OCLC4263659.

Rivero, M. E., & Tschudi, J. J. (1853). *Peruvian Antiquities* (225 p). New York.

Roberts, R. J. & Irving, E. M. (1957). *Mineral Deposits of Central America*. U.S. Geological Survey.

Rodriguez Mejía, R., Sanchez Chimpay, E., Choquehuanca Condori, S., Fabian Quispe, C., & Del Castillo Herrera, B. (2020). *Geología de los Cuadrángulos de Puno y Acora*. INGEMMET, Boletín Serie L. Carta Geologíca Nacional, Escala 1:50,000.

Rose, A. W., Hawkes, H. E., & Webb, J. S. (1979). *Geochemistry in Mineral Exploration* (500 p). Academic Press.

Roskill (1990). *The Economics of Mercury* (156 p). Roskill Information Services Ltd.

Saenz, J., & Martinon-Torres, M. (2011). Gold in Amerika. In R. Slotta, & I. Schnepel (Eds.), *Chiles Kupfer fur die Welt* (pp. 245-256). Deutches Bergbau-Museum.

Sax, N. I. (1984). *Dangerous Properties of Industrial Minerals* (1756 p). Van Nostrand.

Singewald, Q. E. (1950). *Mineral Resources of Colombia, Geologic Investigations in the American Republics* (pp. 151-155). U.S. Geological Survey Bulletin 964-B.

Soto-Viruet, Y. (2018). *The Mineral Industry of Peru*. U.S. Geological Survey 2017-2018 Minerals Yearbook. https://pubs.usgs.gov/myb/vol3/2017-18/myb3-2017-18-peru.pdf

Spindler, E. (2018). *The Story of Cinnabar and Vermilion at the Met*. The Metropolitan Museum of Art. https://www.metmuseum.org

Takacs. L. (2000). Quicksilver from Cinnabar, First Dcumented Mechano-Chemical Reaction. *Journal of Metals, 52,* 12-13. https://doi.org/10.1007/s11837-000-0106-0

Truhan, D. L., Burton, D. L., & Bruhns, K. O. (2005). El Cinabrio en el Mundo Andino. *Revista de Antropología, 18,* 193-205.

Turekian, K. K., & Wedepohl, K. H. (1961). Distribution of the Elements in Some Major Units of the Earth's Crust. *GSA Bulletin, 72,* 175-192. https://doi.org/10.1130/0016-7606(1961)72[175:DOTEIS]2.0.CO;2

United Nations Environment Programme (2017). *Global Mercury: Supply, Trade and Demand* (81 p). United Nations Environment Programme. https://wedocs.unep.org/bitstream/handle/20.500.11822/21725/global_mercury.pdf?sequence=1&isAllowed=y

Vaughan, K. J., Grados, M. L., Eerkens, J. W., & Edwards, M. J. (2007). Hematite Mining in the Ancient Americas: Mina Primavera, a 2000-Year-Old Peruvian Mine. *Journal of Metals, 59,* 16-20. https://doi.org/10.1007/s11837-007-0145-x

Vercelli, A., Paz, M., & Huaman, A. (1977). *Reservas Minerales en el Peru en Antimonio, Bismuto, Mercurio, Selenio, Tellurio, e Indio.* INGEMMET Archivo Tecnico, Codigo A0717.

Webster, P. C. (2012). Not All That Glitters: Mercury Poisoning in Colombia. *The Lancet, 379,* 1379-1380. https://doi.org/10.1016/S0140-6736(12)60582-0

Whitaker, A. P. (1941). *The Huancavelica Mercury Mine* (150 p). Harvard University

Press.

Wilson, F. (1941). Colombia. *Engineering and Mining Journal, 142,* 154-155.

Yates, R. G., Kent, D. F., & Concha, J. F. (1955). *Geology of the Huancavelica Quicksilver District, Peru* (45 p). U.S. Geological Survey Bulletin 975-A.

Zarate, H. (2006). *Proyecto GR5-Estudio Geológico del Batolito de Balsas-Pataz-Buldibuyo, Ocurrencias de la Mineralización en el Area de Estudio* (110 p). INGEMMET Informe A5727.

Archaeological Discovery, 2023, 11, 65-106
https://www.scirp.org/journal/ad
ISSN Online: 2331-1967
ISSN Print: 2331-1959

The Concavity of the Great Pyramid Can Be Derived from Inward Sloping Courses Needed for the Stability

Akio Kato

Department of Mathematics and Physics, Faculty of Science, Kanagawa University, Hiratsuka, Japan
Email: akiokato1521@gmail.com

How to cite this paper: Kato, A. (2023). The Concavity of the Great Pyramid Can Be Derived from Inward Sloping Courses Needed for the Stability. *Archaeological Discovery, 11,* 65-106.
https://doi.org/10.4236/ad.2023.112004

Received: December 26, 2022
Accepted: February 25, 2023
Published: February 28, 2023

Abstract

The Great Pyramid has the character of concavity that each of its four faces is slightly indented along its central line. Applying the geometry on an inclined plane, we show that this concavity could be derived from its inner structure of inward sloping courses gently inclined towards the center of each course, at about 11 degrees to the horizontal, i.e., the slope 1/5 by the ratio of "rise over run". We explain why the inclined layers together with the reinforced base were necessary for the long-term stability of the Pyramid against the severe natural forces like the high gravitational compression, earthquakes and rainstorms, pointing out the feasible fact that the Pyramid has experienced severe rainstorms more than 500 times during the 4500 years. The crucial point about stability is that the effects of such natural forces are quite different between the core of inclined courses and that of truly level courses in the sense that the former can be tightened to become stronger over time, but the latter would be disintegrated to be weaker over time. Scaled-down models of the Pyramid are introduced to understand the large-scale dynamics of the Pyramid. In particular, the small model reduced by 10^{-3} helps us to imagine the transformation of vertical into lateral forces, pointed out by Mendelssohn. On the other hand, the Step Pyramid of Djoser can be identified almost as the half-sized model of the Great Pyramid when the Great Pyramid was assumed to be composed only of truly level courses. And this identification tells the fate of the Great Pyramid only of truly level courses that it would have almost collapsed until now like the Step Pyramid before the recent restoration.

Keywords

Great Pyramid, Concavity, Rheology, Model

1. Introduction

The Great Pyramid at Giza is known to have an amazing character of concavity that each of its four faces is slightly indented along its central line, from base to peak. In other words, the Great Pyramid is a concave octagonal pyramid, rather than the standard square pyramid. This concavity is so subtle to be seen from any ground position, but can be observed from the air. The British Air Force pilot, P. Groves, captured it as in **Figure 1** quite accidently on equinox, 1926, when he was flying over the Pyramid[1] (Groves & McCrindle, 1926). Thanks to the modern technologies, we can nowadays get a picture like **Figure 2** by the Earth observation satellite Quick Bird[2]. Quite recently, a remarkable study using the modern technology of radar measurements has appeared in (Biondi & Malanga, 2022), where the eight-sided nature of all the three pyramids of Khufu, Khafre and Menkaure were rigorously demonstrated. This is a great achievement as it is the first time ever to capture the concavity of the Khafre Pyramid, which was too subtle to be seen compared with that of Khufu's and Menkaure's. Historically,

Figure 1. Photo of the Giza pyramids captured by Brigadier General P. R. C. Groves, British Royal Air Force, at sunset during the Autumnal Equinox. The Great Pyramid, almost in the middle of this picture, shows its bright western face together with the southern face divided into two right triangles. This picture was published in the National Geographic, September 1926.

[1]Natonal Geographic 1926-09: Misquotation prevails in literatures about the year this marvelous photo was taken.
[2]Similar pictures can be seen in http://philippelopes.free.fr/PyramideDeKheopsHuitFacesRevelationDesPyramides.htm.

Figure 2. Pansharpened image of the Great Pyramid, by Quick Bird on Feb.2, 2002. https://www.advite.com/satellitephotos.htm.

the concavity of the Great Pyramid was observed much earlier by Flinders Petrie (Petrie, 1883) who reported that: "I continually observed that the courses of the core had dips of as much as 1/2 degree to 1 degree so that it is not at all certain that the courses of the casing were truly level··· the faces of the core masonry being very distinctly hollowed. This hollowing is a striking feature; and beside the general curve of the face, each side has a sort of groove especially down the middle of the face, showing that there must have been a sudden increase of the casing thickness down the midline. The whole of the hollowing was estimated at 37 (inches) on the North face···" ("37 inches" is about 0.94 meters, less than one meter.) Here, recall the fact that the original shape of the Great Pyramid was the complete square pyramid covered with the casing stones; the survey (Dash & Paulson, 2015) proved the base (with the casing stones) of the Great Pyramid was a perfect square. It was when the casing stones were lost that the concavity revealed. Therefore, the concavity had been covered by the adjustment of casing stones with "a sudden increase of the casing thickness down the midline" as reported above. Another kind of observation was done on equinox, 1934, by a French mathematician André Pochan, who photographed the southern side of the Great Pyramid using the infrared camera, as in **Figure 3**, to observe that this face was divided into two right triangles with different temperatures. His illustration **Figure 4** in (Pochan, 1971) describes the maximal indent as 0.92 meters.

We show in this article, through the geometric analysis of an inclined plane, that the slight concavity of the Great Pyramid could be derived from the gentle

Figure 3. Infrared photograph of the southern face of the Great Pyramid taken by Pochan, at 6 p.m. on equinox, 1934 (Pochan, 1971).

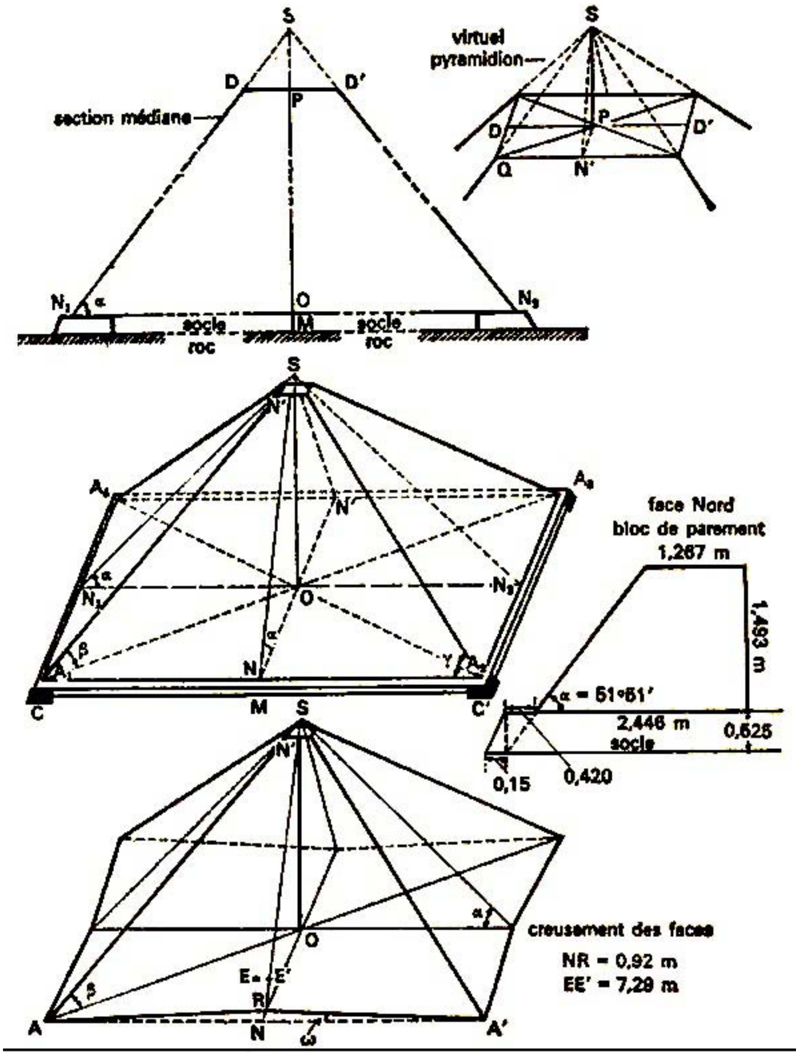

Figure 4. Illustrations of the Great Pyramid in (Pochan, 1971) as a concave octagonal pyramid with the maximal indent 0.92 meters.

slope of inclined courses, which we estimate at about 11 degrees to the horizontal, i.e., the slope 1/5 by the ratio of "rise over run". Due to the perfect masonry we cannot see the core of the Great Pyramid. Contrasting examples whose cores can be seen are the Meidum Pyramid and the three Queens Pyramids of Khufu. The Meidum Pyramid discloses its poor internal masonry through its large hole in the north side, and the inside of the Queens Pyramids is described in Chapter 9 of (Isler, 2001) that "The stones inside the tiers, which form the bulk of pyramid masonry, are small and poorly fitted compared to those on the face, some near the center of the nucleus being placed almost haphazardly". These examples teach us well that we cannot judge the inner structure of any pyramid only by its external appearance even for the small-sized pyramids like the Queens Pyramids, about 30 m high. Therefore, the best possible viewpoint we stand on should be the scientific one based upon geometry, physics and geology.

In Section 2, we will present how to lay blocks on an inclined plane to form inclined courses, and show how the geometry of an inclined plane generates the concavity of the pyramid. The strong structure of the base is definitely needed for the stability, and the Great Pyramid was built on a natural carved outcrop. We show in Section 3 how this outcrop was incorporated to reinforce the structure of the base, and how the concavity tightens the Pyramid consisting of inclined courses. Section 4 remarks a bit unexpected fact that the Great Pyramid has long been exposed to rainstorms "quite frequently" if measured by the timescale of the Pyramid. This fact is very important since most blocks of the Pyramid are limestones, quite vulnerable to the erosion by rainwater. The necessity of the inclined courses for the stability of the Pyramid will be explained in Section 5, based on the idea of (Mendelssohn, 1976) that in a pyramid containing stones of irregular shape and consisting only of truly level courses, the vertically downwards acting force generated by the gravity will develop lateral components, favouring a break-up and flattening of the structure. We show that the core of inclined courses could be tightened by earthquakes and erosion by rainwater, but the core of truly level courses would be loosened by them. In Section 6 we introduce scaled-down models to understand the large-scale (both in space and time) dynamics of the Pyramid from the viewpoint of the rheology. A small model of size 20 cm, reduced by the scale 10^{-3}, helps us to understand the transformation of vertical into lateral forces. Models not so small are also useful, and indeed, the Step Pyramid of Djoser on the Saqqara plateau can be identified almost as a half-sized model of the Great Pyramid if the Great Pyramid was assumed to be made entirely of truly level courses. Therefore, the seriously deteriorated Step Pyramid just before the recent restoration tells the fate of the Great Pyramid if it were consisted entirely of truly level courses.

2. How to Lay Blocks on an Inclined Plane

Figure 5 illustrates the outline of the Great Pyramid as a square pyramid with the top A_0 and the base $A_1A_3A_5A_7$ with its center O. Suppose the square $B_1B_3B_5B_7$

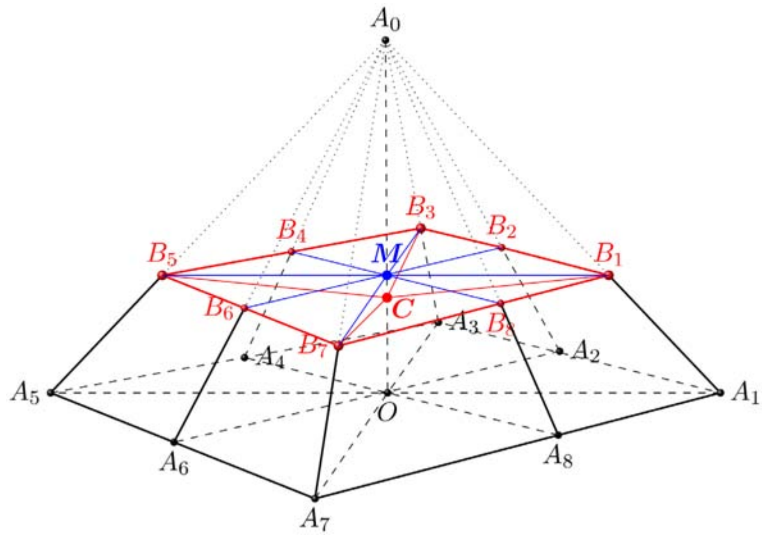

Figure 5. Pyramid $A_0A_1A_3A_5A_7$ illustrates the outline of the Great Pyramid as a square pyramid with the top A_0 and the base $A_1A_3A_5A_7$ with its center O. The square $B_1B_3B_5B_7$ with the center M denotes its horizontal cross-section. The point C is chosen between O and M, to consider the frustum with the sunken rooftop consisting of four inclined triangular planes $\Delta CB_1B_3, \Delta CB_3B_5, \Delta CB_5B_7, \Delta CB_7B_1$.

with the center M is its horizontal cross-section, and choose a point C between O and M. The midpoints of the segments $A_1A_3, A_3A_5, A_5A_7, A_7A_1, B_1B_3, B_3B_5, B_5B_7, B_7B_1$ are denoted $A_2, A_4, A_6, A_8, B_2, B_4, B_6, B_8$, respectively.

Let us consider the frustum with the sunken top surface composed of four inclined triangular planes ΔCB_1B_3, ΔCB_3B_5, ΔCB_5B_7, ΔCB_7B_1, and suppose now that we have completed the piling of stones below this sunken surface, and what we do next is to add a new course of blocks on this surface. Most blocks used in the Pyramid are assumed to be cubic, and the height of blocks used for this new course should be uniform. Due to the symmetry, it would suffice to show how we can lay blocks on the inclined triangular plane ΔCB_1B_3. Note that the horizontal ΔMB_1B_3 in **Figure 5** is the right triangle, but the triangle ΔCB_1B_3 is not, since the point C is below M:

$$\overline{CB_1} = \overline{CB_3} > \overline{MB_1} = \overline{MB_3},$$

$$\angle B_1CB_3 < \angle B_1MB_3 = \pi/2,$$

$$\angle B_2B_1C = \angle B_2B_3C > \angle B_2B_1M = \angle B_2B_3M = \pi/4.$$

The most essential idea which motivated this paper is that:

The geometry on the inclined triangle ΔCB_1B_3 differs slightly from that of the horizontal triangle ΔMB_1B_3.

Choose the point $B_2^\star$ on the line B_2C such that $\angle B_2^\star B_3C = \angle B_2^\star B_1C = \pi/4$. Then, the edge $B_3B_2^\star B_1$ becomes indented as in **Figure 6**. Put $\angle B_2B_3B_2^\star = \angle B_2B_1B_2^\star = \beta$ and $\angle B_2CB_3 = \angle B_2CB_1 = \alpha$, where $0 < \alpha < \pi/4$. We lay blocks in such a way that the sunken edge $B_3B_2^\star B_1$ becomes the outermost

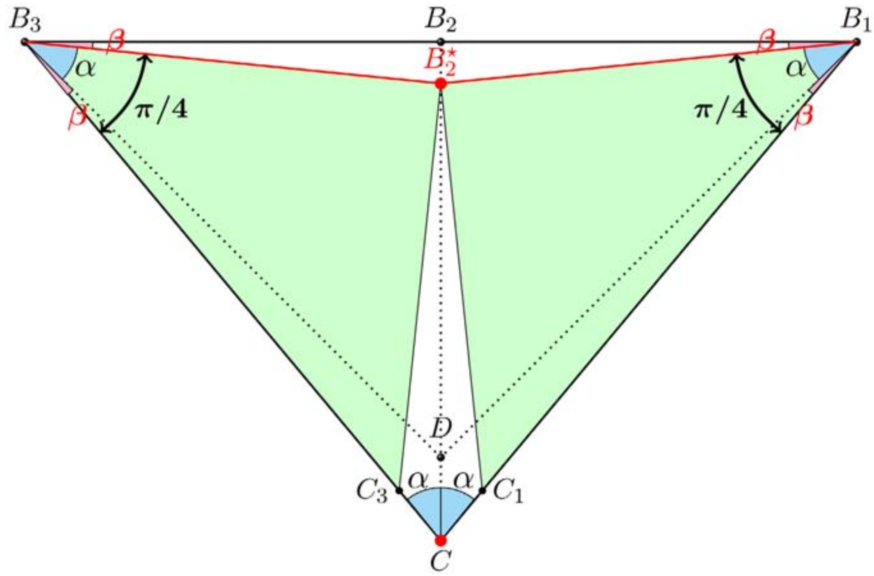

Figure 6. Geometry on the plane ΔCB_1B_3 where the point B_2^* on the line B_2C is chosen to be $\angle B_2^*B_1C = \angle B_2^*B_3C = \pi/4$, and put $\angle B_2CB_1 = \angle B_2CB_3 = \alpha < \pi/4$, $\angle B_2B_1B_2^* = \angle B_2B_3B_2^* = \beta$. The point D on the line B_2C is chosen to satisfy $\overline{B_2D} = \overline{B_2B_1} = \overline{B_2B_3}$ so that ΔDB_1B_3 is a right triangle congruent with the horizontal ΔMB_1B_3 in **Figure 5**. The points C_1 and C_3 on the line B_1C and B_3C, respectively, are chosen to be $\angle B_1B_2^*C_1 = \pi/2$, $\angle B_3B_2^*C_3 = \pi/2$, so that $\Delta B_1B_2^*C_1$ and $\Delta B_3B_2^*C_3$ (green-colored) are congruent isosceles right triangles. Observe that $\alpha + \beta = \pi/4$.

one, so we may call the angle β "the angle of indentation" and the distance $B_2B_2^*$ "the maximal indent". (Note well that in most of our illustrations the indentations of faces are quite exaggerated, as the actual size of the angle of indentation is less than one degree.) In order to see the difference between the inclined ΔCB_1B_3 and the horizontal ΔMB_1B_3, consider the plane ΔCB_1B_3 as in **Figure 6** and take the point D on the line B_2C such that $\angle B_1DB_3 = \pi/2$. Then ΔDB_1B_3 is congruent with ΔMB_1B_3. Since $\angle B_2B_3D = \angle B_2^*B_3C = \pi/4$, the definition of the angle β implies that $\angle DB_3C = \beta$. Then we get $\alpha + \beta = \pi/4$ since the external angle $\angle B_3DB_2$ at the vertex D of ΔDB_3C is $\pi/4$. Consequently, $\angle B_2^*B_3D = \pi/4 - \beta = \alpha$. By symmetry, we have $\angle DB_1C = \beta$ and $\angle B_2^*B_1D = \alpha$. Next, choose a point C_3 on the line B_3C such that $\angle B_3B_2^*C_3 = \pi/2$, and similarly, a point C_1 on the line B_1C such that $\angle B_1B_2^*C_1 = \pi/2$. Then, the green-colored triangles $\Delta B_1B_2^*C_1$ and $\Delta B_3B_2^*C_3$ are congruent isosceles right triangles. So, intuitively speaking, we can imagine that a butterfly with the body B_2D and wings ΔB_1B_2D, ΔB_3B_2D slightly moved its wings to $\Delta B_1B_2^*C_1$ and $\Delta B_3B_2^*C_3$. Note that to choose the sunken edge $B_3B_2^*B_1$ as the outermost one is quite a reasonable selection because the angle $\pi/4 = \angle B_2^*B_3C = \angle B_2^*B_1C$ can be precisely measured using the bisection of the right angle, while it would be very difficult to measure the precise angle $\angle B_2B_3C = \angle B_2B_1C$, slightly bigger than $\pi/4$. Note also that on the inclined plane it would be very difficult to measure precisely any long distance between two points using streched cord, since mason's line becomes catenary due to its weight; see (Isler, 1983). In short, we should measure "angle" rather than "length" on the inclined plane. How to lay cubic blocks on this inclined plane $CB_1B_2^{\star}B_3$ is not so difficult. In **Figure 7**, first, place stones on the (gray-colored) area $CC_1B_2^{\star}C_3$ along the central line $CB_2^{\star}$. Then, we need to lay stones on the triangles $\Delta B_1B_2^{\star}C_1$ and $\Delta B_3B_2^{\star}C_3$. Here, note that, for instance suppose $\overline{B_3B_2}=100$ meters and $\overline{B_2B_2^{\star}}=1$ meter, then $\overline{B_3B_2^{\star}}=\sqrt{100^2+1}=100.0049\cdots$ meters, so that $\overline{B_3B_2^{\star}}$ is longer than $\overline{B_3B_2}$ just about a half centimeter. Hence, practically, we can assume all of four isosceles right triangles $\Delta B_1B_2^{\star}C_1, \Delta B_3B_2^{\star}C_3, \Delta B_1B_2D, \Delta B_3B_2D$ are congruent. And recall that $\Delta B_1B_2D, \Delta B_3B_2D$ are congruent with the horizontal triangles $\Delta B_1B_2M, \Delta B_3B_2M$ in **Figure 5**. Therefore, what we need to do is to lay blocks on $\Delta B_1B_2^{\star}C_1, \Delta B_3B_2^{\star}C_3$ in the same way as on the horizontal triangles $\Delta B_1B_2M, \Delta B_3B_2M$, respectively. Note also that the gray-colored part $CC_1B_2^{\star}C_3$ in **Figure 7** is actually a very narrow area since the distance between C_1 and C_3 is $2\overline{B_2B_2^{\star}}$, which is just 2 meters in case $\overline{B_2B_2^{\star}}=1$ meter. When this kind of laying was done on each of four inclined triangles of the sunken rooftop of **Figure 5**, the whole arrangement would become like **Figure 8**. Notice that, since this is a top view and the point C is below the horizontal square $B_1B_3B_5B_7$, some apparent angles differ from their actual ones, e.g., the actual angle $\angle B_2^{\star}B_3C$ is $\pi/4$, though it appears to be smaller than $\pi/4$ in **Figure 8**. (Precisely speaking, we should place blocks on an area a bit smaller than $B_1B_2^{\star}B_3B_4^{\star}B_5B_6^{\star}B_7B_8^{\star}$, which can be done easily, for instance, if we do not place blocks on the blue part of **Figure 8**. Note also that it might happen that some central part, as shown in white, is already occupied by other structure.) We made a wooden model **Figure 9** of the sunken surface of **Figure 8**.

Now we want to calculate the maximal indent $\overline{B_2B_2^{\star}}$. So, let us introduce the 3-dimensional coordinate system as in **Figure 10** setting the origin at the center

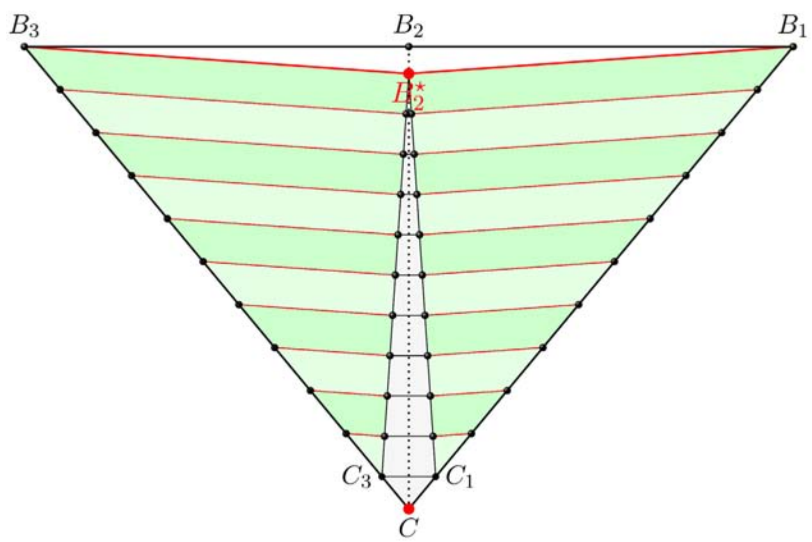

Figure 7. Example of a layment of blocks on the inclined plane $CB_1B_2^{\star}B_3$ in consecutive rows, filling first the (gray-colored) erea $CC_1B_2^{\star}C_3$ along the central line $CB_2^{\star}$.

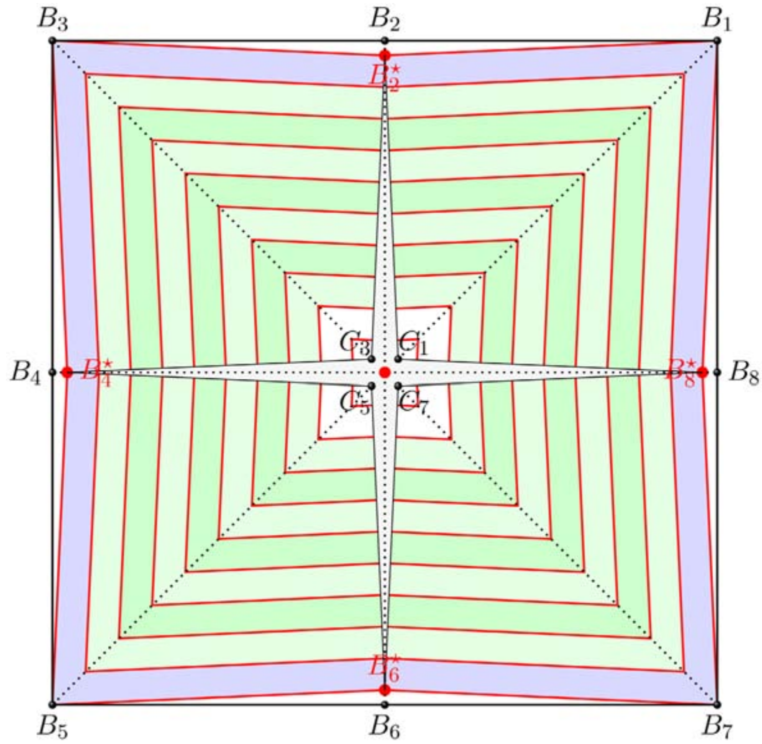

Figure 8. Top View of stone arrangement on the sunken rooftop of **Figure 5**, where the stones are layed on each of the four inclined triangular planes as in **Figure 7**.

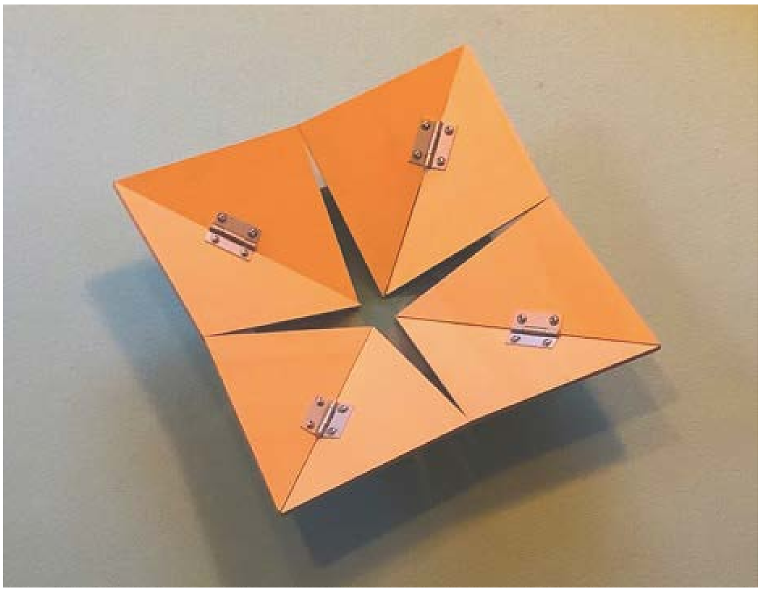

Figure 9. Wooden Model of the sunken surface $B_1B_2^\star B_3B_4^\star B_5B_6^\star B_7B_8^\star$ of **Figure 8** consisting of eight congruent isosceles right triangles, whose length of the legs of a right angle is 15 cm.

M of the square $B_1B_3B_5B_7$. Let $2a$ be the side length of the square $B_1B_3B_5B_7$ so that $\overline{B_1B_2} = \overline{B_3B_2} = \overline{MB_2} = a$. Let h be the depth of the sunken surface, i.e., $\overline{MC} = h$, and let θ be the slope of the triangular plane CB_1B_3, i.e.,
$\tan\theta = \overline{CM} \big/ \overline{B_2M} = h/a$. Then we see that the relation between α and θ is

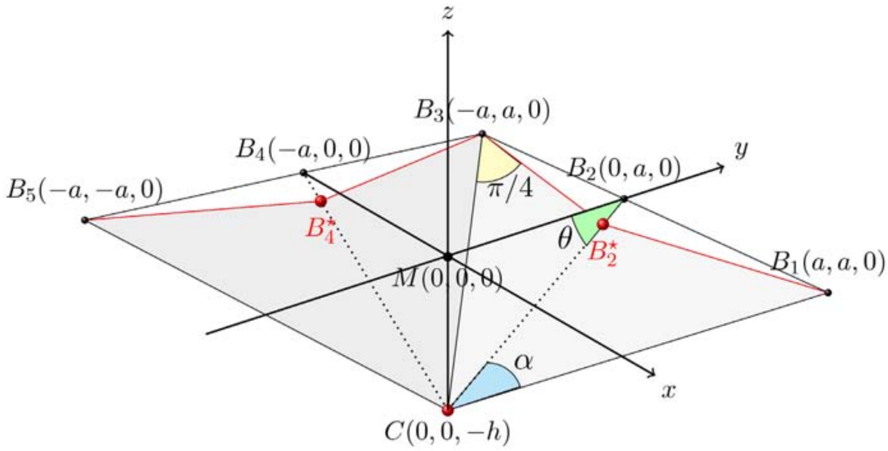

Figure 10. Introduction of a 3-dimensional coordinate system setting the origin at the center M of the square $B_1B_3B_5B_7$ with the side length $2a$ (see **Figure 5**). The depth of the point C is h, and the slope of the triangular plane CB_1B_3 is θ, so that $\tan\theta = h/a$.

$$\tan\alpha = \overline{B_1B_2}/\overline{CB_2} = a\Big/\sqrt{a^2+h^2} = 1\Big/\sqrt{1+(h/a)^2} = 1\Big/\sqrt{1+\tan^2\theta}.$$

In order to calculate $\overline{B_2B_2^\star}$ we will evaluate $\overline{B_2B_2^\star}/\overline{B_3B_2} = \overline{B_2B_2^\star}/a = \tan\beta$. The fact $\alpha+\beta = \pi/4$ implies

$$\tan\beta = \frac{1-\tan\alpha}{1+\tan\alpha}.$$

Putting $\tan\theta = s$ for simplicity, we get

$$\tan\alpha = 1\Big/\sqrt{1+s^2}, \quad \tan\beta = \frac{\sqrt{1+s^2}-1}{\sqrt{1+s^2}+1} = 1+\frac{2}{s^2}\left(1-\sqrt{1+s^2}\right).$$

Now let us utilize the expansion

$$\sqrt{1+X} = 1+X/2-X^2/8+X^3/16-\cdots$$

which is valid for X with $0 \le X \le 1$. We here assume a quite reasonable assumption $0<\theta\le\pi/4$, implying $0<\tan\theta = s\le 1$, so that we can apply the above expansion for $X = s^2$, i.e.,

$$\sqrt{1+s^2} = 1+s^2/2-s^4/8+s^6/16-\cdots.$$

Thus we finally obtain the evaluation

$$\tan\beta = 1+\frac{2}{s^2}\left(1-\sqrt{1+s^2}\right) = s^2/4-s^4/8+\cdots$$

hence

$$\overline{B_2B_2^\star} = a\tan\beta = a\left(s^2/4-s^4/8+\cdots\right).$$

When $s=\tan\theta$ is small, the term $s^4/8$ is quite small compared with $s^2/4$, so, we can roughly estimate that

$$\tan\beta \approx \frac{1}{4}\tan^2\theta, \quad \overline{B_2B_2^\star} = a\tan\beta \approx \frac{a}{4}\tan^2\theta.$$

The side length of the base of the Great Pyramid is about $230 = 115\times 2$ meters, so let us simply assume $a = 100$ meters to get the concrete values of the angle β and the indent $\overline{B_2 B_2^*}$ for various candidates of $\tan\theta$. Then we get **Table 1**. As mentioned in Section 1, Petrie reported the angle of indentation was between a half to one degree and the maximal indent was about 0.94 meters, and Pochan got the closer value of indent 0.92 meters as shown in **Figure 4**. These measurements settle us to conclude that the case which well fits to the Great Pyramid is when $\tan\theta = 1/5$ in **Table 1**, that is:

The concavity of the Great Pyramid is derived from its core layers inclined towards the center at about 11 degrees to the horizontal. Note that the angle of the slope of the inclined layers should be as simple as possible since such an angle was needed to be measured precisely and repeatedly many times during the construction, and it is known that the ancient Egyptian measured the slope by the ratio of "rise over run", and their calculation of ratio is based upon the "unit fractions" like $1/2, 1/3, 1/4, 1/5, \cdots$. So, it would be quite natural to assume that the practical value of the slope $\tan\theta$ was one of such unit fractions. We have drawn two pictures **Figure 11** and **Figure 12**, almost to scale in case of $\tan\theta = 1/5$. **Figure 11** corresponds to **Figure 8**. **Figure 12** shows the vertical cross section along the north-south direction $A_2 A_6$, of the piling of inclined layers (blue-colored) on the well-founded, lowest several courses (light-gray-colored), where the slope of inclined layers $\arctan(1/5) \approx 11^\circ$ can be compared with that of the Descending Passage $\arctan(1/2) \approx 26^\circ$. The point Q is chosen to be the point in the Queen's Chamber, at the height 23 m from the base of the Pyramid; then, since $23/115 = 23/(230/2) = 1/5$ (assuming $\overline{A_2 A_6} = 230\ \text{m}$), the angle $\angle QA_2O = \angle QA_6O$ coincides with $\arctan(1/5)$. (Since the floor of the Queen's Chamber is about 21.5 m heigh from the base of the Pyramid, and the Chamber itself is about 6 m high, the angle $\angle QA_2O = \angle QA_6O$ depends on the choice of the point Q. Creighton & Osborn (2008) chose the "center" of the Chamber and calculated it as 11.73˚. Our choice of the height $23 = 21.5 + 1.5$ m is almost that of the head of a man when he stands on the floor of the Chamber.) Note that if we illustrate the vertical cross section $A_0 A_1 A_5$ along the

Table 1. Values of the angle of indentation β and the maximal indent $\overline{B_2 B_2^*}$ for various candidates of the slope $\tan\theta$ of the inclined courses.

$\tan\theta$	θ (degree)	$\tan\beta$	β (degree)	Max. indent $\overline{B_2 B_2^*}$ (meter)
1/2	26.56···	0.0546···	3.13···	5.46···
1/3	18.43···	0.0263···	1.50···	2.63···
1/4	14.03···	0.0151···	0.87···	1.51···
1/5	**11.30···**	**0.0098···**	**0.56···**	**0.98···**
1/6	9.46···	0.0068···	0.39···	0.68···
1/7	8.13···	0.0050···	0.28···	0.50···
1/8	7.12···	0.0039···	0.22···	0.39···

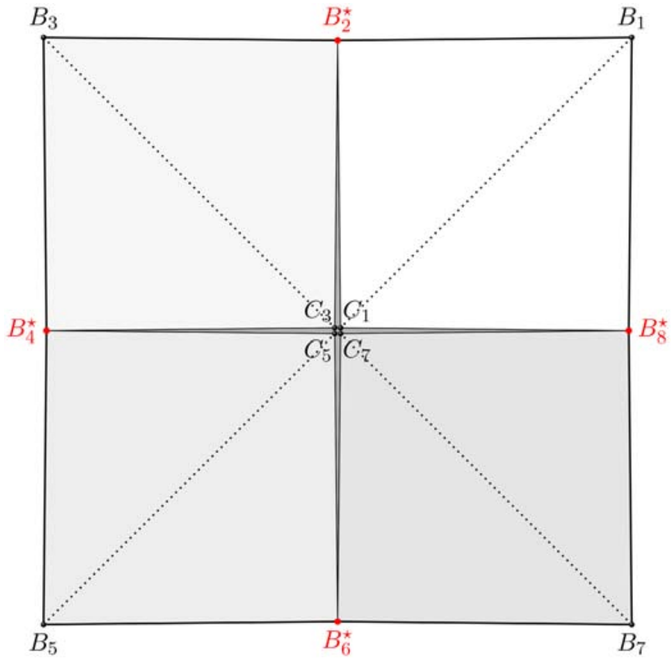

Figure 11. Illustration of **Figure 8**, almost to scale, in case of $\tan\theta = 1/5$ in **Table 1**, providing its alternative view as the union of four square-like inclined surfaces, corresponding to the hinged surfaces in **Figure 9** and each hinged surface becomes a square when it is flattened.

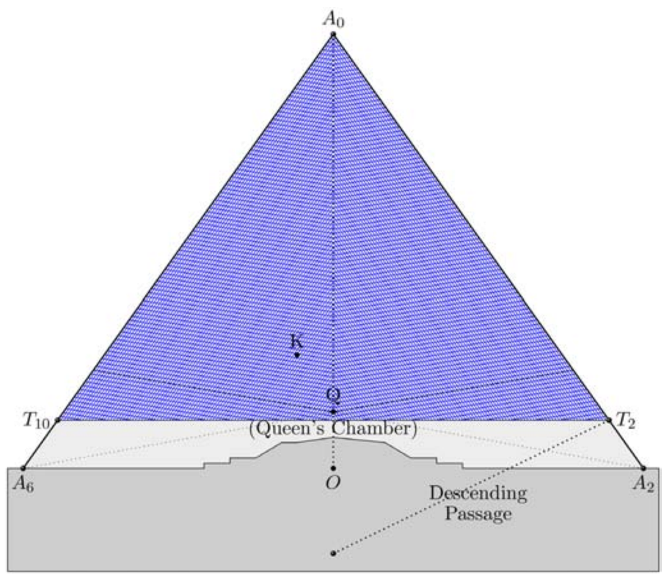

Figure 12. Illustration of the vertical cross section $A_0A_2A_6$ of the Great Pyramid in **Figure 5**, where Q and K denote the positions of the Queen's and the King's Chamber, respectively, supposing A_2A_6 is the north-south direction. Shown in blue color is the piling of inclined layers with the slope 1/5 (measured by the ratio of "rise over run") ≈ 11˚. The gentleness of this angle can be compared with the slope 1/2 ≈ 26˚ of the Descending Passage. The dark gray part is the natural bedrock and its upper part above the ground level A_2OA_6 is an outcrop or inselberg. The light gray part shows the lowest several courses tightly founded by well-squared blocks. This illustration is almost to scale, though we disregarded the indentation of faces and the detailed structure around the central axis A_0O.

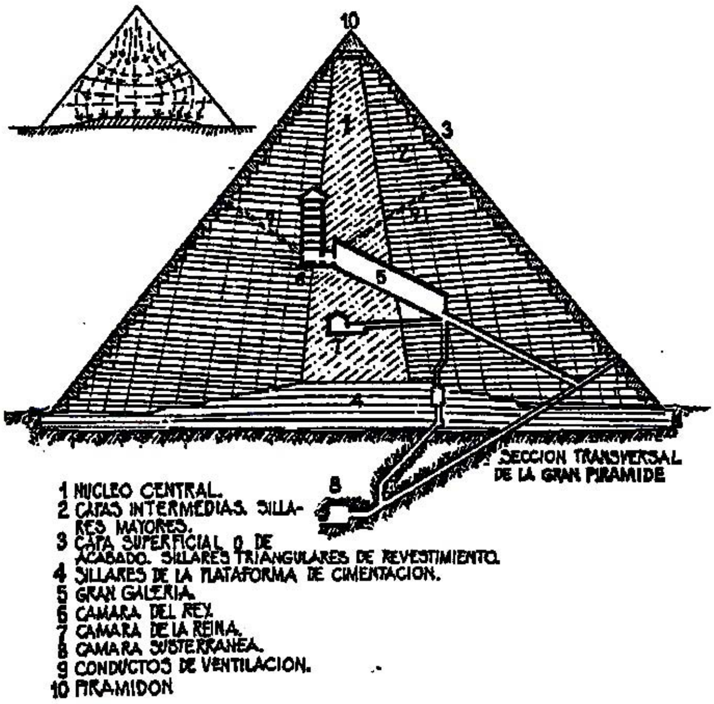

Figure 13. Inner structure of the Great Pyramid described in (Andrade, 1992), well illustrating the gentle slope of the courses.

diagonal A_1A_5 of the base, the slope of inclined layers will appear much gentler, which is $\arctan\left(1/5 \times 1/\sqrt{2}\right) \approx 8^\circ$, the slope of CB_1 or CB_5 in **Figure 5** or **Figure 10**. We are a bit surprised to find **Figure 13** in (Andrade, 1992), quite similar to our **Figure 12**, well embodying the "gentle" slope of the inclined layers. The idea of "the base divided into four triangles slightly inclined towards the center" is also suggested in (Yasseen, 2018). While **Figure 8** can be viewed as the union of four inclined triangular planes, **Figure 11** sees **Figure 8** alternatively as the union of four square-like inclined surfaces $C_1B_8^*B_1B_2^*$, $C_3B_2^*B_3B_4^*$, $C_5B_4^*B_5B_6^*$, $C_7B_6^*B_7B_8^*$. This suggests another way of piling stones by dividing the base into four "squares" like **Figure 11**. Note for example that, though the surface $C_1B_2^*B_1B_8^*$ is not flat, it is a union of two flat right triangles $\Delta C_1B_2^*B_1, \Delta C_1B_8^*B_1$ so that its area is the same as that of the square of the side length $\overline{C_1B_8^*} = \overline{B_8^*B_1} = \overline{B_1B_2^*} = \overline{B_2^*C_1}$, and it would be easier to count the number of stones needed to fill a square rather than a triangle. Additionally, it would be a wise way to convey stones from the four corners to the center since the slope of $B_1C_1, B_3C_3, B_5C_5, B_7C_7$ is only 8 degrees, as mentioned before.

3. Tightening the Pyramid by Reinforced Base and Concavity

Needless to say, the inclined courses mentioned in Section 2 should be placed on a firm foundation. Here we show how the base of the Pyramid was reinforced by the incorporation of the outcrop, and that the concavity strengthens the structure of the whole pyramid including the base. The Great Pyramid was built on a natural carved outcrop whose volume is estimated to be about 20 percent of the monument (Raynaud et al., 2008). Let us present our idea that how they incorporated this outcrop into the monument for its stability. Quite recently, a great discovery was done by (Zalewski, 2017) that each triangular face of the Great Pyramid includes at its bottom a triangular light-colored area consisting of the special type of strong limestone, of the type "grainstone", different from the other parts. This part, which Zalewski called the "Alpha triangle", has the height 16.65 meters and the base about 150 meters, and is composed of the blocks of the uniform size and shape fitted together precisely, and the spaces between them are filled with homogeneous mortar[3]. From the position of the four Alpha triangles it would be natural to assume that what they made inside was a solid substructure like the gray one in **Figure 14** in order to incorporate the outcrop. This gray structure is a union of two solid triangular prisms, one with the bases of the Alpha triangles $\Delta T_1T_2T_3$ and $\Delta T_9T_{10}T_{11}$, and another with the bases of the Alpha triangles $\Delta T_5T_6T_7$ and $\Delta T_{13}T_{14}T_{15}$. The intersection of these two prisms forms a pyramid with the top T and the square base $T_4T_8T_{12}T_{16}$. Though there exist various estimations about the dimensions of the outcrop, we believe that this gray substructure is big enough to include almost all of the outcrop. And we may assume that this substructure was constructed very carefully in the same way as the Alpha triangles, i.e., it is made of uniform blocks fitted very precisely and well connected by mortar not only each other but also to the outcrop. Consequently, this cross-shaped substructure reinforces the base of the Great Pyramid in the sense that it protects the base against the tensions in lateral directions.

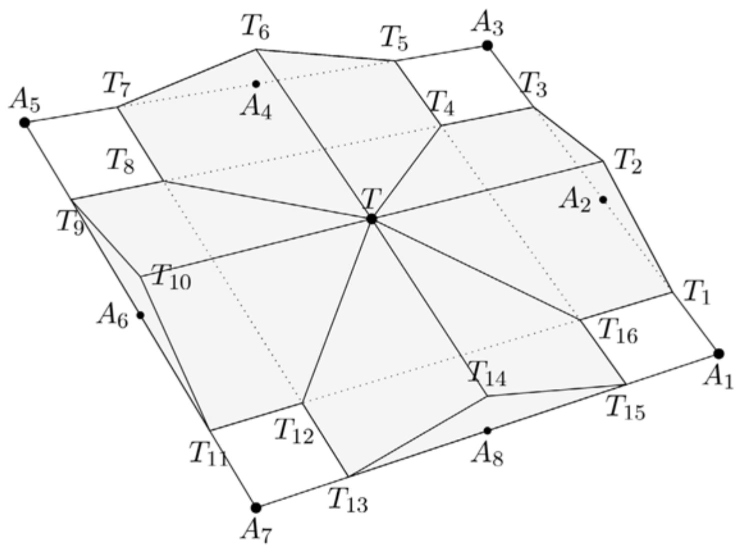

Figure 14. Reinforcement of the base of the Pyramid by the (gray-colored) substructure which incorporates the carved outcrop (see **Figure 12** or **Figure 13**) and bonds it together with the four Alpha triangles $\Delta T_1T_2T_3$, $\Delta T_9T_{10}T_{11}$, $\Delta T_5T_6T_7$, $\Delta T_{13}T_{14}T_{15}$.

[3]The "Alpha triangle" on the western face of the Great Pyramid can be seen very clearly in the picture No.10 in http://chamorrobible.org/gpw/gpw-20040823-English.htm.

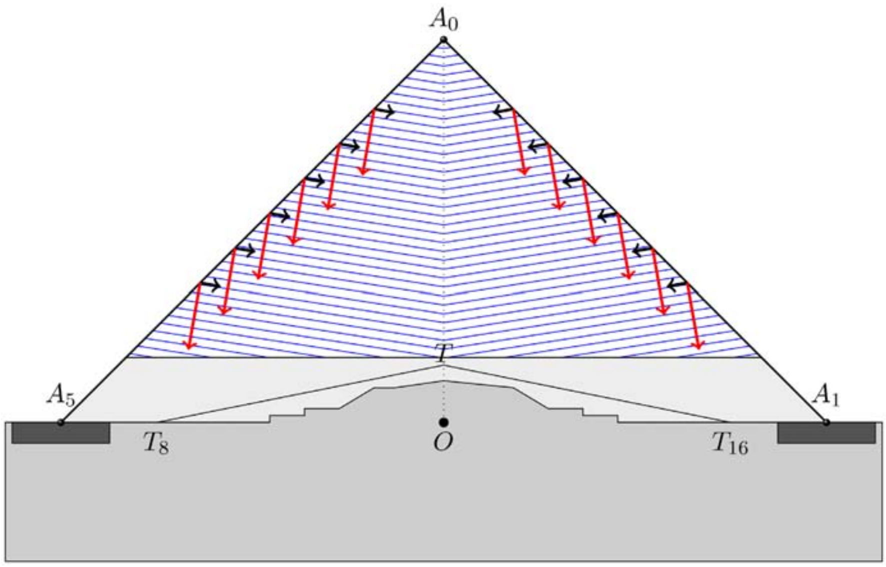

Figure 15. How gravity acts on stones. $A_0A_1A_5$ is the vertical cross section along the diagonal A_1A_5 of the base in case all courses are inclined, and the black parts at A_1, A_5 show the corner sockets. The gravity pushes blocks on the inclined course towards the center of the course (in the direction of black arrows), and also presses them in the direction perpendicular to the course (red arrows). These red-arrowed forces are a bit inclined outward from the vertical (to the same degree as the slope of the inclined course) so that they would cause some extension of the base (the light-gray part). To prevent such extension, the corner sockets would be needed.

Recall the fact that a stone is very weak against the tensile stress, though quite strong against compression. Precisely speaking, this substructure surely protects the base well from the tensions in the directions A_2A_6 and A_4A_8, but it would not be sufficient for the strong tensions in the diagonal directions A_1A_5 and A_3A_7. As illustrated in **Figure 15**, the gravity acting on each block can be decomposed into the force along the inclined course and the one perpendicular to the course, and the latter is a bit inclined outward from the vertical (to the same degree as the slope of the inclined course) to cause some extension of the base. Therefore, we believe, in order to prevent the extension of the diagonals, the corner sockets were additionally set at the four corner points A_1, A_5, A_3, A_7.

Relating with such reinforcement of the base, we want to explain the advantage of the concavity of the four faces, together with the inclined layers, that it helps to tighten the whole Pyramid. **Figure 16** illustrates the force diagram on the base $A_1A_2^*A_3A_4^*A_5A_6^*A_7A_8^*$, where each A_i^* is indented from A_i for $i = 2,4,6,8$. (Practically, these indents are quite small, so **Figure 16** is not to scale.) The reaction forces exerted from the corners against the diagonal tensions are exhibited as the four black-colored vectors of the same length, starting from A_1, A_3, A_5, A_7 and directing to the center O of the base. Denote in particular the reaction forces at the corners A_1, A_7 as $\mathbf{a}, \mathbf{b}$, respectively, and decompose them as

$$\mathbf{a} = \mathbf{a}_1 + \mathbf{a}_2, \quad \mathbf{b} = \mathbf{b}_1 + \mathbf{b}_2$$

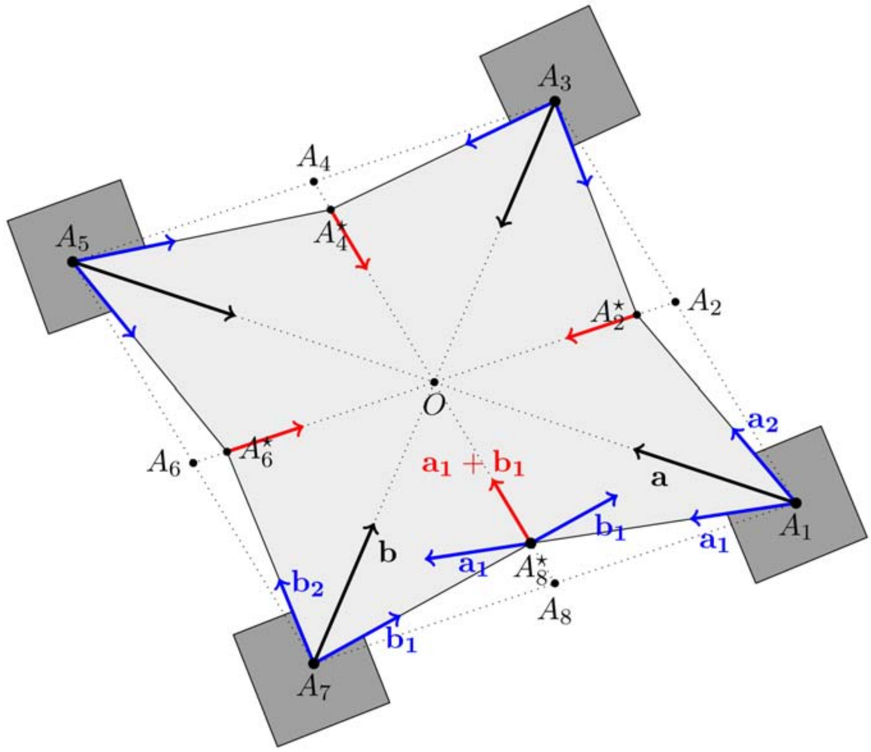

Figure 16. Force diagram on the (light-gray) base with the corners A_1, A_3, A_5, A_7 and the indented spots $A_2^\star, A_4^\star, A_6^\star, A_8^\star$. The dark-gray corner sockets prevent the extension of the diagonals A_3A_7 and A_1A_5 to produce the four black-colored reaction forces, which then generate the four red-colored forces at the indented spots towards the center O. Not to scale.

where both $\mathbf{a}_1$ and $\mathbf{b}_1$ direct to the indented $A_8^\star$, and $\mathbf{a}_2, \mathbf{b}_2$ direct to the indented $A_2^\star$ and $A_6^\star$, respectively. Then we get the (red-colored) vector sum $\mathbf{a}_1 + \mathbf{b}_1$ directing to the center O. Hence the reaction forces at the corners A_1, A_7 generate the new (red-colored) force at $A_8^\star$ towards the center O. By symmetry, we can observe the similar effects of the reaction forces at the other corners, hence concluding that:

The four black-colored reaction forces at the corners A_1, A_3, A_5, A_7 towards the center O produce the four red-colored forces at the indented spots $A_2^\star, A_4^\star, A_6^\star, A_8^\star$ towards the center O.

A similar mechanism works also on every inclined course as shown in the force diagram **Figure 17**, which is quite similar to **Figure 16** except that the dark-gray parts show some stones at the corners and the black-colored forces are due to their weight and the inclination of the course. Also, the effects of the black-colored forces are similar:

The four black-colored forces at the corners B_1, B_3, B_5, B_7 towards the center C produce the four red-colored forces at the indented spots $B_2^\star, B_4^\star, B_6^\star, B_8^\star$ towards the center C.

Thus, the form of concavity contributes to tighten and stabilize the whole Pyramid consisting of inclined courses!

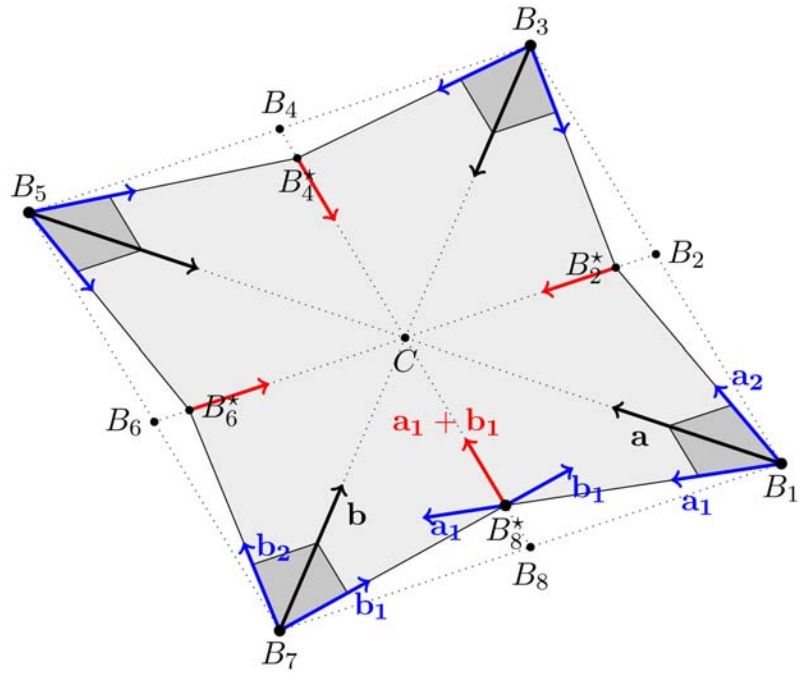

Figure 17. Force diagram on the inclined course with the corners B_1, B_3, B_5, B_7 and the indented spots $B_2^\star, B_4^\star, B_6^\star, B_8^\star$. The dark-gray parts show some stones at the corners, which produce the four black-colored forces due to the gravitation and the inclination of the course. These black forces generate the red ones at the indented spots, in the same way as **Figure 16**. Note that the light-gray surface in this figure is sunken, but the one in **Figure 16** is horizontal.

4. Heavy Rainstorms in Egypt and Measures against Them

We here want to remark a bit unexpected fact that the Great Pyramid has long been exposed to rainstorms, which were "infrequent" by the timescale of our daily life but "quite frequent" by the timescale of the Pyramid. Note though that the Pyramid was not affected by the annual Nile flooding since it lies on the Giza plateau about 60 meters above sea level. A dominant weather pattern in East Africa is called the Red Sea Trough, which is "hot and dry". But quite abruptly, only a few times a year (mainly in October or November) this pattern changes into the "Active" Red Sea Trough that is accompanied by heavy rainstorms, flash floods, and severe societal impacts in the Middle East. De Vries et al. (2013) and Alharbi (2018) explain the atmospheric dynamics leading to extreme precipitation, and twelve many cases caused by the "Active" Red Sea Trough are listed in (De Vries et al., 2013), which affected the Levant during the 25 years, Oct.1979 ~ Oct.2004, and four cases among which brought terrible damage in Egypt. For example, the case of the November 1994, one of the worst disasters with 600 casualities in Upper Egypt, affected Egypt from Luxor all the way to Cairo, and its torrential rains brought terrible damage in the Valley of the Kings (Weeks, 1995)[4]. The Tempest Stela of Ahmose describes a great storm which struck Egypt

[4]Los Angeles Times (Nov.5, 1994) "New Flooding in Egypt Threatens Historic Tombs" (https://www.latimes.com/archives/la-xpm-1994-11-05-mn-58761-story.html).

about 1550 BC and destroyed tombs, temples and pyramids in the Theban region. This severe weather is suspected to be due to the climate change triggered by a massive volcano explosion at Thera, the island of Santorini in the southern Aegean Sea (Ritner & Moeller, 2014). Heavy rainstorms around the Great Pyramid during the Old Kingdom were evidenced by the excavations of the town Heit el-Ghurab, or the Lost City of the Pyramid, as stated in (Ogilvie-Herald, 2020) that: "Excavations have shown the town was repeatedly destroyed by flash flooding and rebuilt during the reigns of the pharaohs Khafre and Menkaure, both kings of the 4th Dynasty. During Khafre's reign Heit-el-Ghurab was struck by three floods in twenty-six years, the first 'destroyed the town, while the others caused widespread damage.' However, during the later reign of Menkaure evidence from the excavations have shown that the flooding was far worse." From this record, it would be quite natural to assume that the Pyramid was actually hit by a few heavy rainstorms even during its construction over 20 years. So we believe, expecting such severe rainstorms and knowing that the limestone is vulnerable to the erosion by rainwater, the Great Pyramid incorporated some measures against the rainstorms. First, it was quite needed that the base of the Pyramid be protected from the erosion, and this would be one of the reasons that they made the specific fine structure like **Figure 14**, in which stones were fitted together precisely and the spaces between them were filled with homogeneous mortar. Second, the whole Pyramid was covered with a smooth roof of casing stones. These outer casing stones were fitted together with extremely high precision, and we believe this precision was not only for the beauty of the appearance but also for the practical reason to protect the Pyramid from the erosion by rainwater. But unfortunately, most of the outer casing stones of the Great Pyramid fell down or loosened due to the massive earthquake in 1303 AD (of magnitude 6.5 on the Richter scale, with the epicenter Fayum). So, after this earthquake the remained inner structure has been exposed directly to rainstorms until now. Even before this destructive earthquake, we suspect, the Pyramid would have been hit by severe earthquakes and violent rainstorms so that some of its outer casing stones could be damaged or loosened to let the rainwater seep through them to bring high humidity inside the Pyramid. According to (Butzer et al., 2013), the Old Kingdom (the 4th Dynasty) paleoclimatic anomaly, accompanied with heavy rainstorms, was repeated on a subdued scale during the Early Middle Ages. And, in the study of the climate during the Middle Kingdom, (Bell, 1975) asserts that "Review of textual and architectural evidence bearing on rainfall suggests that the Middle Kingdom had conditions similar to those of the A.D. 1800s, with heavy rainfalls somewhat less rare than in the present century." Thus, it seems that this pattern of anomaly has continued ever since (perhaps, a long before) the Old Kingdom, and we may conclude that the Great Pyramid has been long exposed to rainstorms quite frequently by the timescale of the Pyramid: Indeed, "a few times in 20 years" would accumulate during the 4500 years into more than 500 times! (An example of photo of a recent rainstorm which passed near the Bent Pyramid can be seen in the report by the photographer T. Badal: "A Refreshing Look at Egypt's Ancient Pyramids"[5]) Nevertheless, the Great Pyramid has survived through this long-term exposure to rainstorms even after the loss of the casing stones, and this surprising fact strongly infers the existence of some system of drainage inside the Pyramid. What system? We proposed in (Kato, 2020) that almost all stones of nucleus were chamfered and the chamfered edges of stones were utilized to make vertical holes and wells ("well" means here an empty column surrounded by walls of stones, like a chimney), in particular, the "Central Well" around the axis of the Great Pyramid from the center of the base to the apex. If all edges of cubic stones were chamfered, their chamfered parts can make not only vertical holes but also horizontal vents, and such vents and holes would form a three-dimensional grid throughout the whole nucleus, with the main vent, the Central Well. Therefore, this grid could serve well as a drainage and ventilation system of water and air. **Figure 18** and **Figure 19** show the general flow of rainwater inside the Pyramid in case all courses are horizontal or inclined, respectively. Noteworthy is that a slight inclination of courses changes the pattern of flow drastically, from **Figure 18** to **Figure 19**. The lateral flow in **Figure 18** is based upon the nature of water as a liquid that any amount of water placed on a horizontal plane will soon be spread laterally, but such flow would be quite slow so that the rainwater would not be drained easily in case of **Figure 18**.

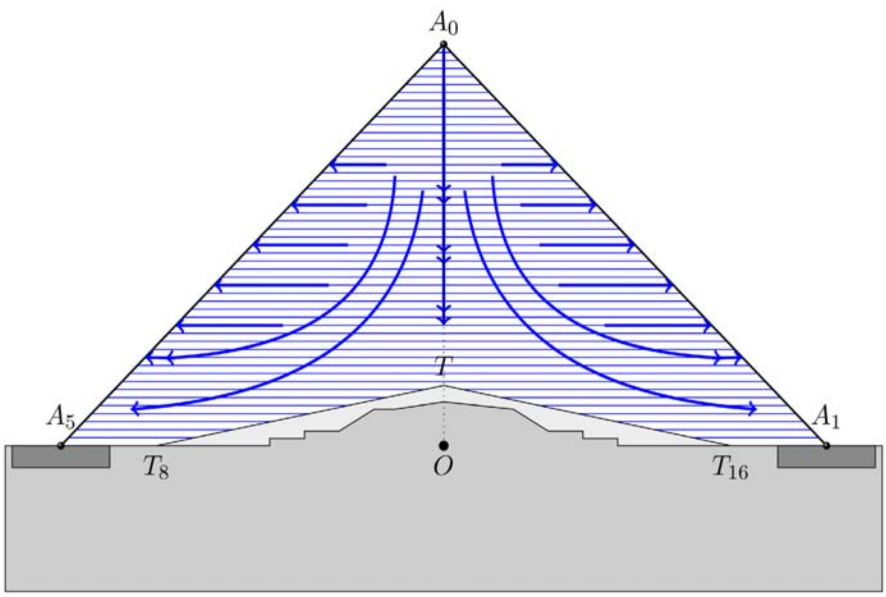

Figure 18. Vertical cross section $A_0A_1A_5$, where A_1A_5 is the diagonal of the base, showing the flow of rainwater (by blue arrows) in case all courses are truly level. The double arrows along the axis A_0T show the flow through the Central Well. About this "Central Well" see (Kato, 2020). We note that the existence of the Central Well does not contradict **Figure 12**, an illustration viewed from the east to the west, since the Queen's Chamber is away from the central axis about seven meters eastwards.

[5]https://www.nytimes.com/2022/07/04/travel/egypt-pyramids.html.

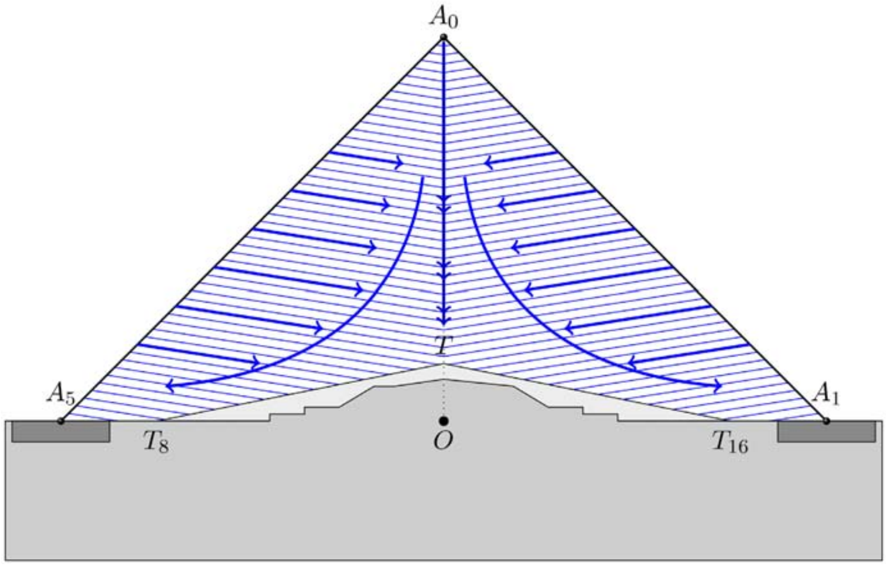

Figure 19. Vertical cross section $A_1A_0A_5$ showing the flow of rainwater in case all courses are inclined. The double arrows along the axis A_0T show the flow through the Central Well.

5. Inward Sloping Structure to Eliminate the Action of Lateral Forces

We have already shown that the concavity could be derived from the system of inward sloping courses. So, what we need to show next is the necessity of such system for the stability of the Great Pyramid. The stability we want to argue is the "long-term" stability against the high gravitational compression as well as against the natural disasters like severe earthquakes and heavy rainstorms (as mentioned in Section 4) experienced by the Great Pyramid during 4500 years. See (Morsy & Halim, 2015; Badawy, 1999; Hemeda et al., 2020) for historical earthquakes in Egypt. Though the actual notable one was the aforementioned case of 1303 AD which shook off almost all of the casing stones, "4500 years" is long enough to experience such "once-in-a-millennium" severe earthquakes at least several times. If we assume that the Pyramid was made only of horizontal courses, it is quite hard to imagine that such a strong ground shaking shook off only the casing stones without disturbing its inner structure. We will explain why? **Figure 20** and **Figure 21** illustrate how the Pyramid would behave under the ground shaking caused by an earthquake. The former is the case when we assume the Pyramid consists only of level courses, while the latter is when the Pyramid consists only of inclined courses. It would be obvious that the casing stones were shaken off because they were pushed outwards by the backing stones just behind them, inferring that the inner stones were also moved by the earthquake. Note that damage to buildings due to earthquake is related more closely to ground motion, rather than the energy of earthquake (the Richter scale), and an appropriate measure commonly used in earthquake engineering is "Peak Ground Acceleration (PGA)" which is equal to the maximum ground acceleration

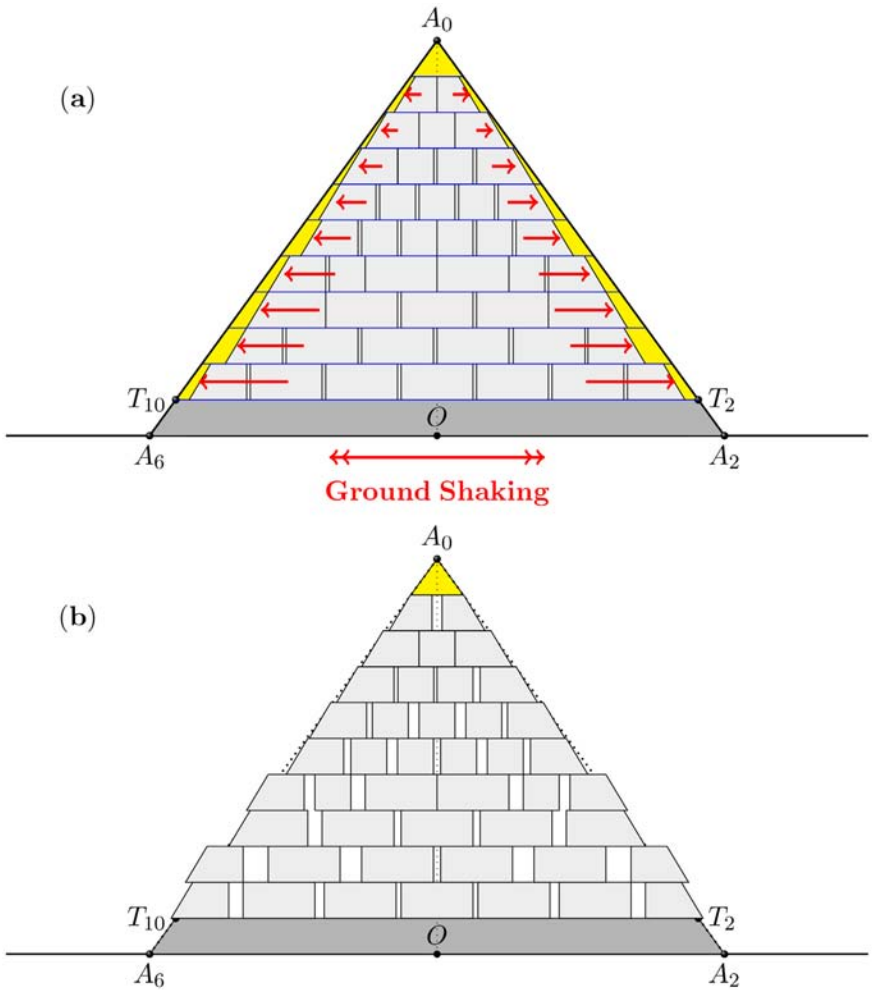

Figure 20. Ground Shaking (a) by an earthquake (strong as the case of the 1303 AD), and its aftermath (b), in case all courses were supposed to be horizontal. The ground shaking generates the lateral shaking of the horizontal courses, and the (yellow-colored) casing stones would be pushed outwards by the backing stones just behind them as shown by the red arrows. Note that the backing stones just behind the casing stones can be moved rather easily (compared with those in the center) since they are not so strongly compressed from the above.

that occurred during earthquake shaking at a location. Of course, each earthquake is an assembly of various kinds of seismic waves, and the main thrusts including PGA are always accompanied by many tremors. In either case of horizontal or inclined courses, such main thrusts would move the casing stones outwards (or upwards in case of inclined courses). But, the aftermath would be different. In case of horizontal courses some inner stones would remain to be separated as in Figure 20, but in case of inclined courses, the tremors after PGA would do some job to settle the inner stones down to their original positions as in Figure 21, since the courses are inclined. Hence the present non-disturbed, symmetric posture of the Great Pyramid would almost deny the structure only of truly level courses, taking account of all the hitherto earthquakes including the one of 1303 AD.

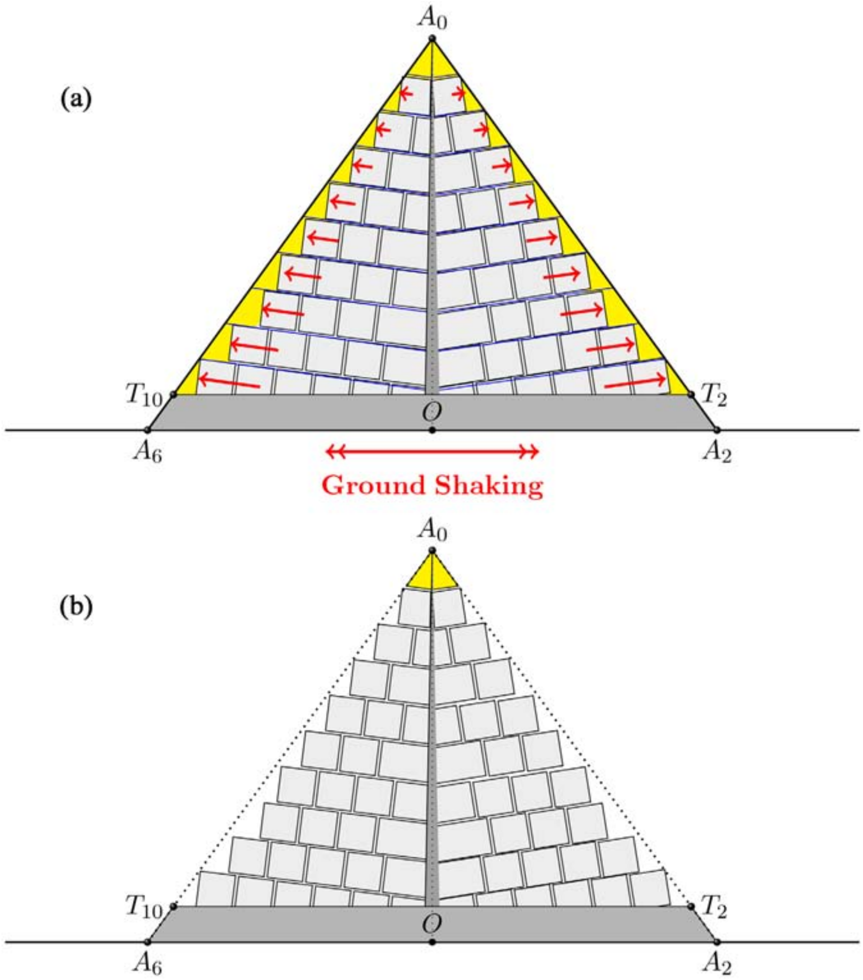

Figure 21. Ground Shaking (a) by an earthquake (strong as the case of the 1303 AD), and its aftermath (b), in case all courses are inclined. The ground shaking generates the shaking of the inclined courses, and the (yellow-colored) casing stones would be pushed outwards (or tossed in the air) by the backing stones just behind them as shown by the red arrows. Though the backing stones may be moved somewhat outwards or upwards by the "PGA (Peak Ground Acceleration)" of the earthquake, they would be settled down to their original positions by the tremors after the PGA, since the courses are inclined.

Recall the simple physical fact that the Great Pyramid stands upright only by the force of gravity. The physicist Mendelssohn pointed out in (Mendelssohn, 1976) that "in a pyramid containing stones of irregular shape, the vertically downwards acting force generated by the gravity will develop lateral components as in (b) of **Figure 22**, favouring a break-up and flattening of the structure", where he assumes the pyramid consisted only of truly level courses. Note that this picture (b) of **Figure 22** is similar to **Figure 18** because the flow of rainwater is governed also by the gravity. Mendelssohn (1973) or Mendelssohn (1976) explains that, when the blocks of irregular shape touch only in a few places, the pressure can rise locally to several hundred atmospheres, crumbling sets in at the affected regions of the stones and a shift in position of the individual blocks might take place. Then this shift causes the transformation of vertical into lateral

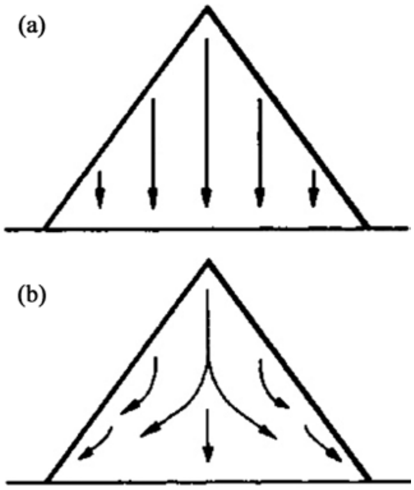

Figure 22. Illustrations in (Mendelssohn, 1973) with the caption: "The distribution of weight forces in (a) a pyramid built of well-squared blocks and (b) a pyramid with poor internal masonry."

forces. In general, as noted in Section 1, internal masonry of a pyramid is quite poor compared with its outside smooth masonry, and in case of the Great Pyramid we can further take account of the energy management in raising the vast quantity of the stones, so that we may naturally assume that blocks inside the Pyramid are relatively small and roughly shaped. Then recall our daily experience that a four legged stool on a floor will often wobble but a three legged one will not. Two roughly shaped stones would contact in a similar way that two faces do not adhere completely, rather touch only at three spots; it is even possible that two stones touch only at one tiny spot when they are placed horizontally. Then the aggregate of stones of irregular shape would be exerted by various kinds of stress like compressive, tensile and shear stresses. A stone is usually very strong against compression, but very weak against tension as the tensile strength is known to be only about one-tenth of the compressive strength. The maximum pressure at the base of the Great Pyramid is about

$$2.5\ \mathrm{t}/\mathrm{m}^2 \times 140 = 350\ \mathrm{t}/\mathrm{m}^2 = 3.5\ \mathrm{MPa}$$

assuming that a cubic limestone of volume 1 m^3 weighs about 2.5 tonnes and the height of the Pyramid is about 140 m. A limestone usually can endure the pressure about $100\ \mathrm{MPa} = 10000\ \mathrm{t}/\mathrm{m}^2$, but this high value is meaningful only if the stone is well squared, and the story would be different if the stone is not well squared and has to support a heavy weight only using some three spots of the stone, as illustrated in Figure 23. There would be various mechanisms of how some vertical force, caused by the heavy load or the earthquake, would transform into lateral forces. An instance is shown in Figure 24 when the stones are laid horizontally. Any original rock would contain some invisible tiny cracks so that it might happen that those cracks would be enlarged little by little by the stress even below the yield strength of the rock, and a long-term accumulation of such strains might deform the rock visibly. This kind of consideration is known to

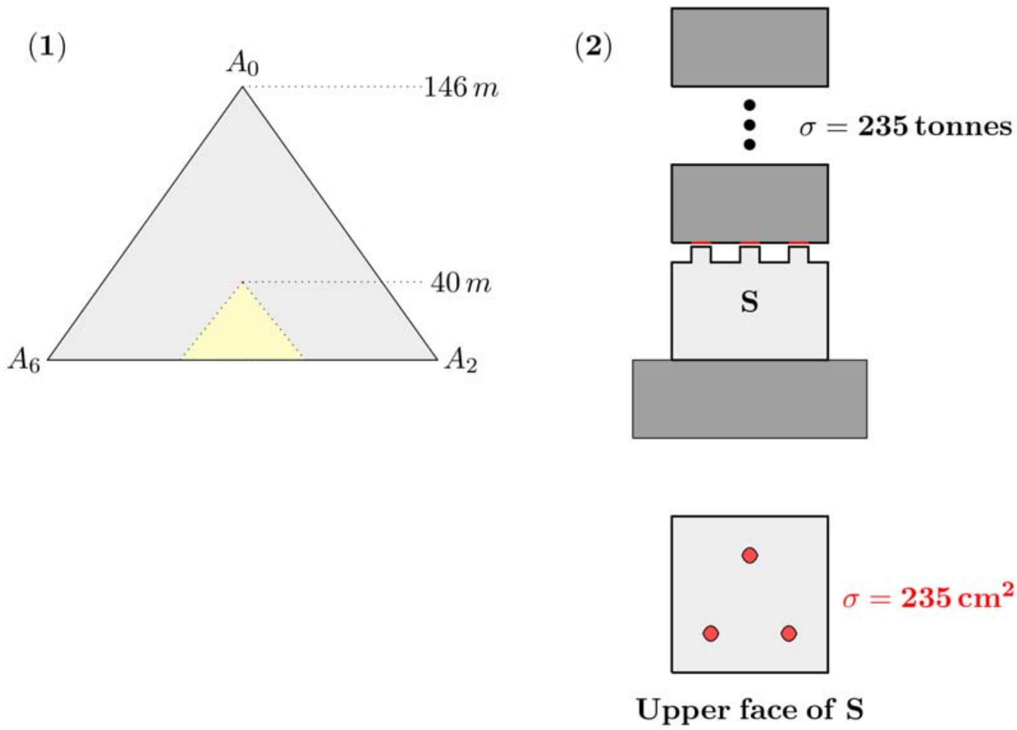

Figure 23. Assuming the compressive strength of a limestone is $100\ \mathrm{MPa} = 1\,\mathrm{t/cm}^2$, any well squared limestone with the upper face of 1 m^2 can support 10,000 tonnes, but a stone with an irregular upper face can support only σ tonnes if it touches the upper stone only with the area σ cm^2. The illustration (2) shows the case of a stone S such that the touching area is $\sigma = 3\pi(10/2)^2 = 235.6\cdots \approx 235\ \mathrm{cm}^2$ consisting of three (red) discs, each of diameter 10 cm. The cross section (1) of the Pyramid indicates the part yellow-colored (just below the King's chamber) consisting of stones each of which has to support more than $2.5\ \mathrm{t} \times 100(\mathrm{m}) = 250\ \mathrm{t} > 235\ \mathrm{t}$. So, if the stone S were placed horizontally inside the yellow part, its upper face would have been crushed when the construction of the Pyramid was completed.

be the "rheological" viewpoint, where the term "rheology" is based upon the idea of Heraclitus *panta rhei* "everything flows". For example, suppose in (b) of Figure 22 blocks had "flowed" in the arrowed direction at the average rate of one millimeter a year; then such "flow" would amount to 4 or 5 meters during 4500 years, an observable distortion much bigger than the concavity of one meter we argued in Section 1. But, no such distortion can be seen in the present symmetric Great Pyramid, leading to the denial of the structure of the Pyramid consisting only of truly level courses.

What we want to remark further is the effect of erosion by the heavy rainstorms as explained in Section 4. The important aspect we want to point out is that the effect of erosion would be quite different between the horizontal course and the inclined one in case both admit somewhat irregular gaps between blocks. The erosion on the horizontal courses would separate stones laterally as illustrated in Figure 25, while the erosion on the inclined courses would tighten the arrangement of blocks, incorporating the gravitational force, as shown in Figure 26. Observe then that each block separated laterally from other blocks as

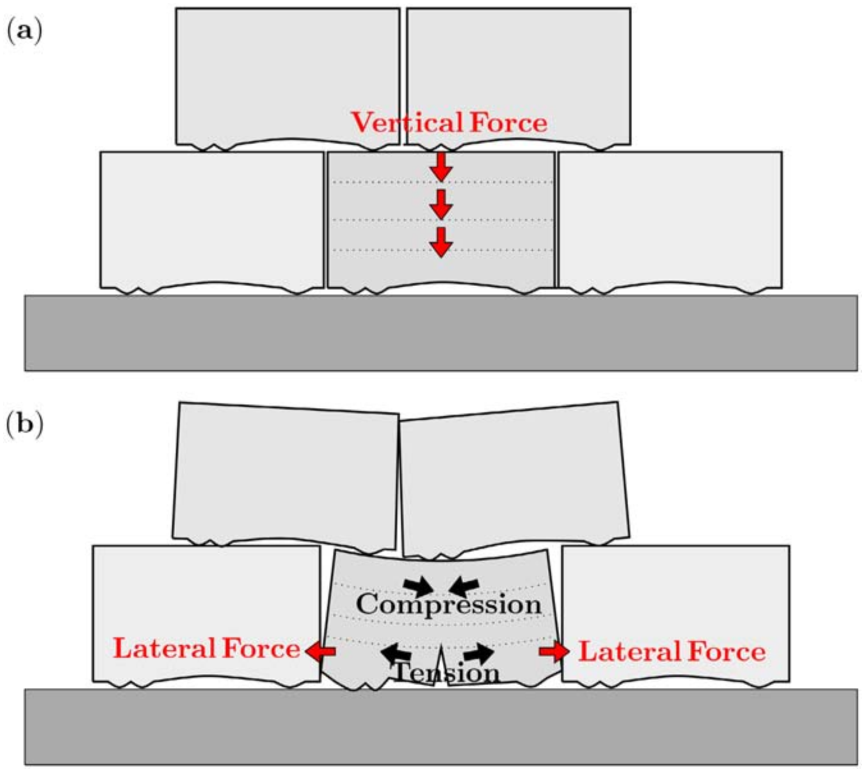

Figure 24. Instance of the mechanism of "the transformation of vertical into lateral forces" by a sag in a stone, due to the fact that a stone is weak against tension though strong against compression. This mechanism works when the stones of irregular shape are laid horizontally. The actual crack as in the middle stone of (b) might be very small in the order of millimeters.

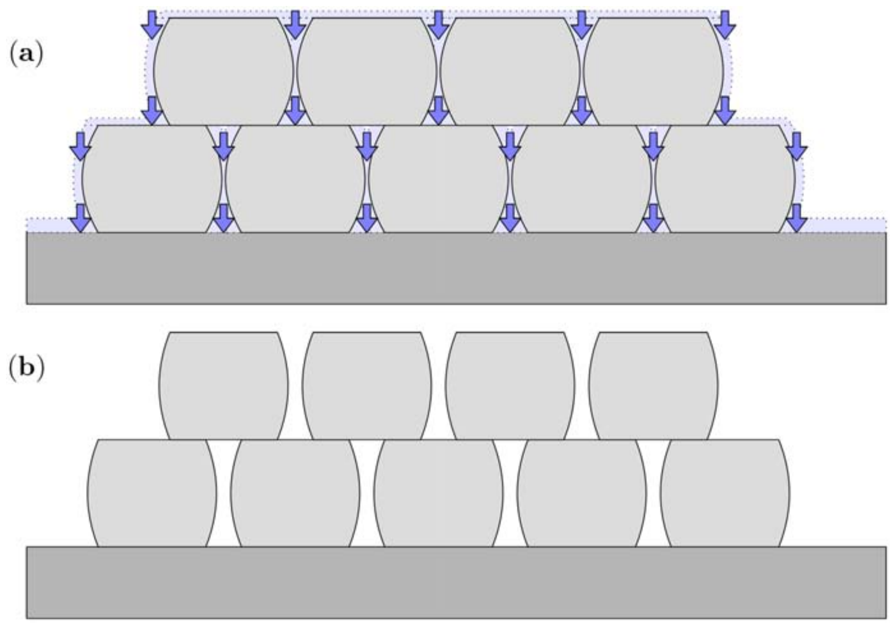

Figure 25. Effect of Erosion of blocks on the Horizontal courses by Rainfall: The rainwater flows down through the gaps between the blocks, not well-squared, as indicated by the blue arrows in (a), eroding the vertical faces of blocks to separate them laterally like (b), a bit exaggerated.

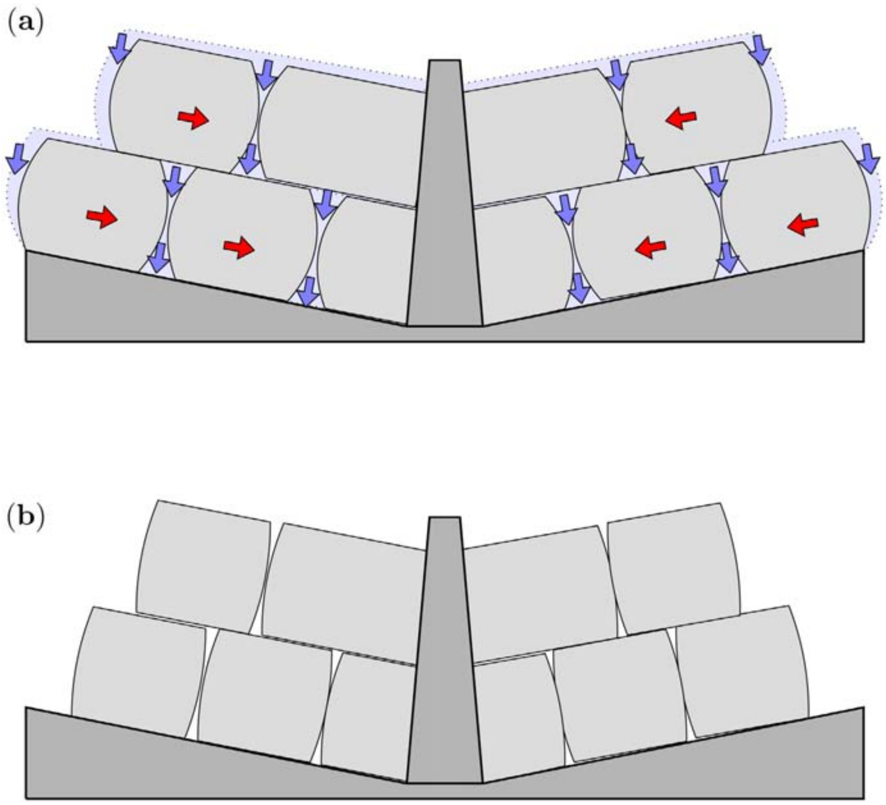

Figure 26. Effect of Erosion of blocks on the Inclined courses by Rainfall: The rainwater flows down the gaps between the blocks, not well-squared, as indicated by the blue arrows in (a). The erosion would incorporate the gravitational force to move blocks inwards (as the red arrows of (a)) so that the arrangement of blocks would be tightened further like (b).

in (b) of Figure 25 would be compressed only in the vertical direction, but each inclined block as in (b) of Figure 26 would be compressed in all of the three directions since it is completely surrounded and confined by other stones. It is well known that a stone is much stronger against the confined compression than against the uniaxial unconfined compression. Hence, the erosion makes the stones on the horizontal course vulnerable to the gravitational compression, but in contrast, the erosion strengthens the stones on the inclined course against compression. Effect of ground shaking due to earthquake is similar to that of erosion as already observed in Figure 20 and Figure 21. Thus, both erosion and earthquake are in favor of inclined layers, but against horizontal ones. The only stable case for a horizontal course would be that it consists of uniform stones fitted very precisely or well connected by mortar each other, since such unified course would behave like a bedrock. Note that granite is much stronger than limestone against earthquake and erosion. The first course of the Great Pyramid is such a stable horizontal course where many large granite blocks are used. But, it would be almost impossible to make the whole Pyramid only of such stable horizontal courses, as such precise placement would consume too vast energy to complete the construction of the Pyramid in two decades or so, taking account of its immense quantity of stones, over two millions.

Note that the above argument is about the inner part of the Pyramid, and we can see some evidence of the erosion like **Figure 25** in some outer stones laid horizontally. For example, see **Figure 27** which is the drone view of the top of the Great Pyramid by the famous photographer A. Ladanivskyy. Here we can see wide vertical gaps between blocks as in **Figure 25**, which would be mainly due to the erosion, not due to the eathquake since the top of the Pyramid is rather stable against ground shaking. We believe the original arrangement of blocks on the top was much tighter. Though not in the Pyramid, another evidence is **Figure 28** of the Moria Roman aqueduct[6,7]. This aqueduct is made of limestone called travertine, and the erosion by rainwater as well as the weathering by wind widened the gaps between stones so that the key stone of this arch is now almost dropping. We note, though, that it is not easy to compare the aqueduct with the Great Pyramid. Indeed, the Pyramid is 2.5 times older than the aqueduct since the aqueduct dates back only to the end of the 2nd century AD, but Moria is much wetter than Giza. How erosion or weathering or high compression has

Figure 27. Drone View of the Top of the Great Pyramid by the photographer A. Ladanivskyy. (https://www.thisiscolossal.com/2021/07/drone-view-of-giza/)

[6] https://www.archaeology.wiki/blog/2021/03/19/the-roman-aqueduct-at-moria/ (19 Mar 2021) "The Roman Aqueduct at Moria".

[7] https://www.archaeology.wiki/blog/2021/03/04/danger-of-the-moria-roman-aqueduct-collapsing/ (04 Mar 2021) "Danger of the Moria Roman aqueduct collapsing".

Figure 28. The Roman Aqueduct at Moria (https://www.archaeology.wiki/blog/2021/03/19/the-roman-aqueduct-at-moria/).

changed outer stones of the Great Pyramid can be seen in (Hemeda & Sonbol, 2020).

6. Scaled-Down Models

Mendelssohn (1971) demonstrated an experiment **Figure 29** about the action of lateral forces in a small model of a pyramid, made of a highly viscous, homogeneous material (the exact size and the name of material of this model are unclear). One may wonder why did he choose a "small" and "plastic" model? In this section we explain the appropriateness of his choice by introducing the idea of the "scaled-down dynamical" model. Compared with the large scale in space and time of the Great Pyramid, our size is small and our lifespan is short so that it is not easy for us to understand properly how the Pyramid behaves in the long run. In order to overcome such difficulties, geologists devised the method of creating "scaled-down" models (Hubbert, 1937; Deus et al., 2010; Schellart & Strack, 2016). So, let us consider some scaled-down models applying the theory of scale model construction as described in pp.143-150 of (Pollard and Fletcher, 2005), or (Hubbert, 1937). See also (Merle, 2015) about the basic principles of the scaling procedure. Note that we scale down everything, space and time, not only the Pyramid but also its environment including the bedrock, earthquakes and rainstorms. The Great Pyramid is the prototype, and let us reduce this prototype by the scale of 10^{-3}, to get a small model **M** (10^{-3}) of size about 20 cm. Precisely stating, the model ratio L_r for the length is

$$L_r = L_m / L_p = 10^{-3}$$

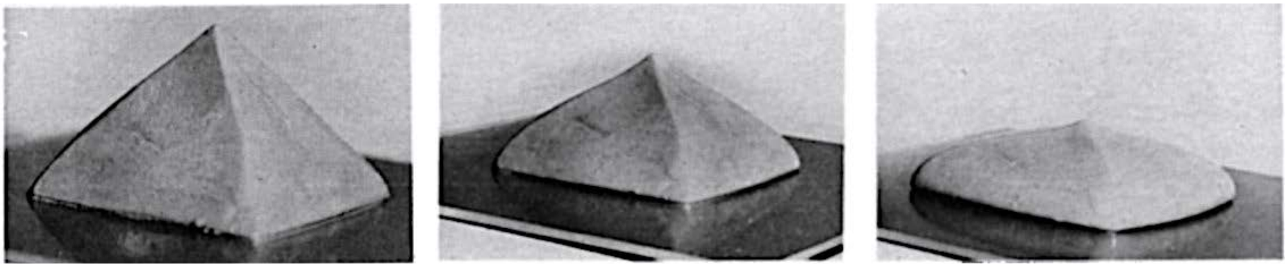

Figure 29. Picture in (Mendelssohn, 1971) with the caption "Three successive stages in the plastic flow of a pyramid under its own weight. Material and structure of the model were homogeneous, showing merely the action of lateral forces." The same picture appears in his book (Mendelssohn, 1976) with the caption "Plastic flow under gravity. The small pyramid model, made of a highly viscous material, collapses under its own weight".

where L_p stands for the length of any part of the prototype, and L_m is the corresponding length of the model (the subscripts *m* and *p* refer to the model and prototype, respectively). Since the dimension of the volume is Volume = (Length)^3, the model ratio V_r for the volume should be

$$V_r = \frac{V_m}{V_p} = \frac{L_m^3}{L_p^3} = L_r^3 = 10^{-9}.$$

For simplicity let us choose the material of the model in such a way that the model ratio ρ_r for the mass density is one, that is, the density of any part in the model is equal to the density of the corresponding part in the prototype: $\rho_m = \rho_p$. Hence the ratio M_r for the mass is the same as that of the volume:

$$M_r = \frac{M_m}{M_p} = \frac{\rho_m V_m}{\rho_p V_p} = V_r = 10^{-9}.$$

Next, we need to determine the ratio T_r for the time

$$T_r = \frac{T_m}{T_p} \text{ where } T_p = 4500 \text{ years.}$$

But, this ratio can not be chosen independently since the time relates to the acceleration, and in order to make the model *dynamically similar* (i.e., holding the similarity of driving forces) to the prototype, we need to require that the gravitational acceleration around the model in the laboratory is the same as that around the Pyramid on the Giza plateau. Therefore, the ratio a_r for the acceleration should be one:

$$a_r = \frac{a_m}{a_p} = \frac{L_m T_m^{-2}}{L_p T_p^{-2}} = L_r T_r^{-2} = 1, \text{ i.e., } L_r = T_r^2.$$

Hence

$$T_r = L_r^{1/2} = 10^{-3/2} = 0.0316\cdots (\approx 1/30)$$

and

$$T_m = T_p T_r = 4500 \text{ years} \times 0.0316\cdots = 142.3\cdots \approx 140 \text{ years.}$$

This means we need to observe the small model **M** (10^{-3}) for $T_m = 140$ years in a laboratory, about which we discuss later. Using the dimensional formulae (Force) = (Mass) × (Acceleration), (Stress) = (Force)/(Area) = (Force)/(Length)^2, we can get the ratios F_r, S_r for the force and stress, respectively, as follows:

$$F_r = M_r \cdot a_r = M_r = L_r^3, \quad S_r = F_r \cdot L_r^{-2} = L_r^3 \cdot L_r^{-2} = L_r.$$

Summarizing, we have the model ratios

$$T_r = L_r^{1/2} = 10^{-3/2} > L_r = S_r = 10^{-3} > V_r = M_r = F_r = L_r^3 = 10^{-9}$$

along with our convention $\rho_r = a_r = 1$. Let us assume for simplicity that the prototype is the square pyramid with base length 200 meters and height 140 meters, consisting of cubic blocks, each with the side length 1 meter and the weight 2.5 tonnes. Let us call the compressive strength simply as "strength", and assume also that the strength of blocks is uniform and is equal to that of the bedrock, so that we can call this same value S_p as "the strength of the Pyramid". So, all blocks are uniform in size, weight and strength. Thence, the model **M** (10^{-3}) has the base length 20 cm and height 14 cm, and consists of very small cubic blocks, each of which has the side length $L_m = 1\,\text{m} \times 10^{-3} = 1\,\text{mm}$, the mass $M_m = 2.5\,\text{tonnes} \times 10^{-9} = 2.5\,\text{milligrams}$, and the strength $S_m = S_p \times 10^{-3}$. Let us note here about the strength of blocks of the Great Pyramid. According to Arnold (1991), "porous" limestone can endure the pressure 20 - 90 MPa and "dense" limestone can endure 80 - 180 MPa, so, a typical limestone would be able to endure the pressure about 100 MPa, as we assumed in Section 5. On the other hand, some backing limestone samples were recently collected from the Great Pyramid (Hemeda & Sonbol, 2020) to examine their strength. The result was about 15 MPa, very low value, probably due to the weathering over four millennia. So, precisely speaking, the strength S_p is a decreasing function of the time. In case $S_p = 100\,\text{MPa}$, we have $S_m = 0.1\,\text{MPa} = 1\,\text{atm}$, which means each block of size 1 mm in the model can support the weight of only 10 grams, and in case $S_p = 15\,\text{MPa}$, only 1.5 grams. So, we may be able to make such blocks using some soft granular material. Then recall the rheological fact in our daily life that granular materials, like sands, grains of wheat, rice or corn, can flow like a liquid under the gravitational force. Hence, our model **M** (10^{-3}) is quite similar to the Mendelssohn's model **Figure 29**, not only geometrically but also dynamically. The flow of grains is generated by the gravitational force conducting stress by "force chain" formed by grains resting on one another. Inside the Pyramid this "force chain", formed by stones (of irregular shape) resting on one another, generates a flow of stones which would be quite slow, maybe a millimeter a year. Direction of this flow would be essentially the same as that of rainwater illustrated in **Figure 18** and **Figure 19**, since both force chain and rainwater are governed by the gravity. Note that the flow of force along the blue curved arrows can be sustained by the reinforced corner structure like the corner sockets (see **Figure 15**), so that the stones would be moved by the force chain, only along the blue "straight" arrows in either figure. Note also that such movement of stones along the straight arrows in **Figure 19** is essentially a compression and would eventually cease since all of them direct to the terminal near the center of the Pyramid. Thus, we may conclude, via the model **M** (10^{-3}), that stones would move laterally to flatten the Pyramid if we assume it were made only of horizontal courses, while stones would be concentrated around the center of the Pyramid to tighten its whole structure if we assume it were made only of inclined courses. Both **Figure 12** and **Figure 30** are almost to scale so that, assuming $\overline{A_2A_6} = 20\ \text{cm}$, they can be viewed as illustrations of the cross section of the model **M** (10^{-3}) in case of inclined courses and in case of truly level courses, respectively. These figures show well that the blocks are very small compared with the whole Pyramid so that they can be viewed naturaly as "fine grains" in the model **M** (10^{-3}).

As mentioned before, after we made an appropriate pyramid for the model **M** (10^{-3}), there remains a difficult task to observe it for $T_m = 140$ long years in a laboratory. But this would be almost impossible to accomplish since "140 years" is much longer than our lifespan. So, we should be satisfied with a thought experiment, or observe the model during the first few years to imagine the rest of the experiment. In spite of this defect, still we can say that the term of 140 years is much easier to imagine than the long term of 4500 years. For example, it is not easy for us to imagine the rheological accumulation over four millennia of the very slow flow of stones by "force chain" inside the Pyramid, but we can expect by intuition that such a flow in the small model **M** (10^{-3}) of fine grains of low strength might happen during the observation of 140 long! years. Deriving such proper intuition is the crucial role of the scaled-down model. Note further that in this thought experiment of "140 years", the model should experience the

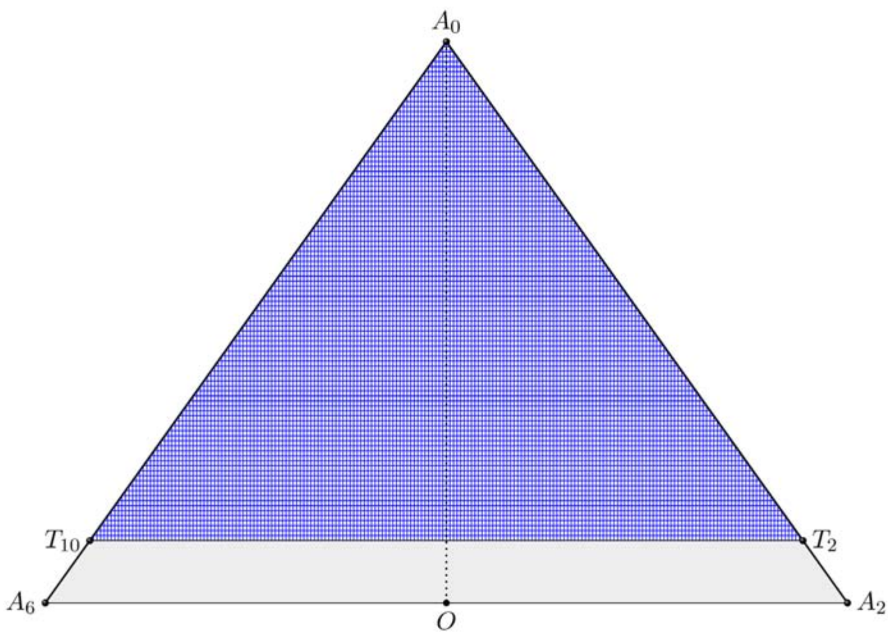

Figure 30. Vertical cross section $A_0A_2A_6$ of the Great Pyramid in case the Pyramid consisted only of truly level courses. This illustration is almost to scale, hence can be the cross section of the model **M** (10^{-3}) if we suppose $\overline{A_2A_6} = 20\ \text{cm}$.

downsized versions of all the ground shakings (caused by the earthquakes) and rainstorms that the Great Pyramid has experienced, in a historically similar timing. As mentioned before, damage to buildings due to earthquake can be measured by the maximum ground acceleration called "Peak Ground Acceleration (PGA)", rather than the energy of earthquake (the Richter scale). Then we can take the advantage of our convention that the ratio of the acceleration is one, that is, PGA in the model should be the same as PGA in the prototype. An additional remark in transferring an earthquake into the model is that we have to scale down everything around the Pyramid. So, not only the blocks of the Pyramid, but also its bedrock should be replaced by the one with the low strength reduced by the scale $S_r = 10^{-3}$. Thence we can let the model, together with its bedrock, experience the same (w.r.t. PGA) ground shakings that the Great Pyramid have experienced, in a historically similar timing.

As for rainstorms, by the ratio $T_r = 0.0316\cdots \approx 1/30$ for the time, "a few times in 20 years during the 4500 years" in the prototype would be converted into "several times in every year during the 140 years" in the model. Since (Velocity) = (Acceleration) × (Time), the ratio v_r for the velocity is the same as that of the time: $v_r = a_r T_r = T_r \approx 1/30$. Hence, a storm at the speed of 30 meters/sec in the prototype should be converted into light winds of 1 meter/sec in the model, so that each severe rainstorm in the prototype would turn into a gentle spray of water in the model. So, for instance, if the rainstorm lasted two days, then water should be sprayed onto the model for about one and a half hours: $48\ \text{hours} \times 0.0316\cdots \approx 1.5\ \text{hours}$. Here again, we point out that "several times in every year during 140 years", or equivalently, "once in a few months during 140 years" is much easier to understand than "a few times in 20 years during 4500 years". We note here that it is not an easy task to maintain strict dynamical similarity between the proptotype and the model when we need to evaluate multiple kinds of force including non-mechanical one. For example, "the erosion of limestone by rainwater" is not only the mechanical detachment of tiny particles from the surface, but it also includes a chemical reaction, i.e., a dissolution along micron-scale grain boundaries of limestone. So, we must be very careful about the choice of material for the model if we want strict similarity of erosion between the proptotype and the model. We have disregarded such an intricate problem in the above argument.

Models not so small are also useful in understanding how the long-term dynamical behavior of the Pyramid depends upon its inner structure. For example, let us consider **M** (10^{-2}), **M** (10^{-1}), **M** (1/2) and **M** (5/8).

1) The model **M** (10^{-2}): This model is of size about 2 meters and consists of blocks of size about 1 cm, which would be quite an appropriate size to to be handled with; for example, we can lay blocks of size 1 cm to make horizontal or inclined courses, which we can not do in the model **M** (10^{-3}) since blocks of size 1 mm are too small. The strength of blocks in this model should be $1\ \text{MPa} = 10\ \text{atm}$, which is about the half of the strength of "sun dried brick". (It is known that the strength of "sun dried brick" is about 2 MPa, while that of "first class brick" is

about 10 MPa.)

2) The model **M** (10^{-1}): This model is of base length 20 m and height 14 m, and consists of blocks of size about 10 cm, so its external appearance is almost the same as that of the satellite pyramid (G1-d) within the Great Pyramid complex, whose original dimensions are of base length 21.75 m, and of height 13.8 m. But, a notable difference is that the model **M** (10^{-1}) is made of small blocks of size about 10 cm, while the blocks in (G1-d) would be large as one meter. Further, the strength of each block in the model should be reduced to one-tenth of the strength of the corresponding block in the Great Pyramid, but the blocks in (G1-d) would have the same strength as those of the Great Pyramid. Some core of (G1-d), consisting of horizontal courses, can be seen in its remains (Hawass, 1996). So, to make the model **M** (10^{-1}) of horizontal courses we need to replace the stones of the satellite pyramid (G1-d) by "first class bricks" (with the strength 10 MPa) of size about 10 cm. We here want to remark that the original satellite pyramid (G1-d) could be quite strong and stable since its size is small, which means for example that each cubic block of size one meter at the base of (G1-d) needs only to endure the low gravitational pressure at most 0.35 MPa since (G1-d) is only 14 m heigh, compared with the case 3.5 MPa of the Great Pyramid of 140 m heigh (as mentioned in Section 5). The formulation of the scaling theory was first introduced by (Hubbert, 1937), where Hubbert notes conclusively that "quite generally, for a body of material having a given specific strength, the over-all strength of the body taken as a whole decreases with increase of size. Thus small bodies of a given material are strong; large bodies of the same material are weak, and larger the body the greater its weakness." This applies well to our case: The small (G1-d) could be strong but the large Great Pyramid could be weak, as long as we assume in both the same structure of horizontal courses made of the same material, i.e., a cubic limestone of size one meter. So, we can believe that in spite of the structure of horizontal courses, the original satellite pyramid (G1-d) could have remained intact until now if its blocks were not looted.

3) The model **M** (1/2): A bit surprisingly, we could find the candidate of this model. We next show that the Step Pyramid of Djoser (the Third Dynasty) on the Saqqara plateau can be identified essentially as the model **M**(1/2) in case the Great Pyramid was assumed to be made entirely of truly level courses. The Step Pyramid was built as the first monumental structure made of stone, about 4600 years ago, i.e., about a century before the Great Pyramid. Originally the building was 62 meters high with a base of 109 × 125 meters, and its blocks are of limestones of size 30 - 50 cm. Its core consists of six mastabas of horizontal courses, built on top of each other, and is surrounded by inward-leaning accretion layers (Isler, 2001). On the other hand, the pyramid of the model **M**(1/2) is 70 meters high with a base of 100 × 100 meters, and consists of blocks, each of which is a cube of size 50 cm, weight 2.5/8 tonnes ≈ 300 kg, and of strength $S_p/2$. Since the ratio for the time is $T_r = L_r^{1/2} = 1/\sqrt{2} = 0.707\cdots$, as a model for the Great Py-

ramid we need to observe it during $4500 \times 0.707 \cdots \approx 3200$ years. Now compare the Step Pyramid with the model **M** (1/2). Their appearance is almost the same, including the size of blocks. Their inner structure is also similar as long as we assume the Great Pyramid consisited of truly level courses. A slight difference is that the strength of the model **M** (1/2) is about a half of the strength of the Step Pyramid. Thence, we may roughly conclude that (i) observing the model **M** (1/2) of "lower" strength during "shorter" period (3200 years), and (ii) observing the Step Pyramid of "higher" strength during "longer" period (4600 years), would reach almost the same result. And the result of (iii) is the present status of the Step Pyramid. As reported in (Kukela & Seglins, 2013) and (Ewais et al., 2016), the Step Pyramid has been deteriorated seriously by weathering, and heavily by the earthquakes. (It seems the outer faces of the Step Pyramid were deteriorated especially by the erosion of wind carrying sands, but what we concern is the deterioration of its core due to the structure of level courses.) In particular, the 1992 Cairo earthquake caused severe damage to this pyramid on the Saqqara plateau so that, due to the risk of collapse, the pyramid had been closed to visitors for nearly 14 years, and reopened in March, 2020. (This 1992 earthquake was "moderate", of magnitude 5.8, but unfortunately, the focus was quite near, about 14 km from the Step Pyramid (Khalil et al., 2017).) **Figure 31** shows the photo, taken in 2019, of the Step Pyramid under the restoration work. In short, the result of the observation (ii) is that the Step Pyramid has almost collapsed. Consequently the model **M** (1/2) would collapse similarly, after the observation (i). Therefore, we can conclude that the Great Pyramid would have almost collapsed until now if its core were made only of truly level courses.

4) The model **M** (5/8): The Meidum Pyramid (mentioned in Section 1), the second pyramid after the Step Pyramid, has its unique appearance due to its partial collapse before its completion. It has a base with the side length 144 m and its present height is 65 m, but 91.65 m if finally fully cased, so its original shape

Figure 31. The Djoser Step Pyramid at Saqqara under the restoration work, in April, 2019. A photo in BBC News: https://www.bbc.com/news/uk-wales-47828999.

is proportional to the Great Pyramid. Seyfzadeh (2017) describes that the exterior of the Meidum Pyramid was a scaled-down version of the Great Pyramid by a factor of 5/8. So, we may say that the model **M** (5/8) has the shape of the (intended) Meidum Pyramid, but we can not identify it with the Meidum Pyramid because of the difference of their inner structures. The inner structure of the Meidum Pyramid is exceptionally well known: The Meidum Pyramid has a central core of 60 cubits width, against which 9 accretion layers lean, and such entity was further surrounded with thick outer mantle (about 7 m) of packing stones laid horizontally. Roughly speaking, it is made of the nucleus of "accretion layers" surrounded by the mantle of "horizontal courses". One of the reasons of its collapse was suspected to be due to the fact that the outer mantle was built on sand instead of solid rock, unlike the Great Pyramid (Mendelssohn, 1973). Though the Meidum Pyramid can not be the dynamical model **M** (5/8), we can learn from its partial collapse that the "inclined" core of accretion layers is stronger than the mantle of "horizontal courses" since the most of the core "remains as a tower of three great steps" (Isler, 2001).

Isn't it amazing that some conceptional ties emerge among isolated pyramids through "models", as we have seen in the above (2), (3) and (4)?

In Cacciola et al. (2022) we can see a "gelatin" model of the Step Pyramid, down-sized by the scale of 1/500. This model was made for the experimental test of the Vibrating Barriers (device for the seismic protection of the Step Pyramid), and built with "gelatin", precisely: "The model has been made of a mix of gelatine/glycerine/cold water/hot water with weight proportions 1/3/2/3 and cured for 3 days." Since the Step Pyramid itself can be seen as a model of the Great Pyramid reduced by 1/2, this gelatin model actually reduces the Great Pyramid by $1/2 \times 1/500 = 10^{-3}$, so that it can be regarded as the model **M** (10^{-3}) of the Great Pyramid consisting of truly level courses. Hence, this exemplifies that it is possible to make our model **M** (10^{-3}) using the gelatin, which would be quite similar to the Mendelssohn's model **Figure 29**. See Merle (2015) about gelatin as a material for experiment.

7. Concluding Remarks

We have shown that the concavity of the Great Pyramid could be derived from the geometry of its core of inclined courses gently sloping inwards, and such inclined structure was quite needed for the long-term stability of the Pyramid against high gravitational pressure, earthquakes and rainstorms. It was often asserted only from the external appearance of pyramids that "in the major shift from step to true pyramid, the earlier pyramids were built with slanting accretion layers, but the later ones were built with horizontal courses." To turn this assertion into a true statement in our sense, the term "horizontal" should be replaced by "almost horizontal, but slightly inclined". We believe the "immortal" stability was the most important aspect of the Great Pyramid for the pharaoh Khufu and his people, and they were smart enough to introduce some structure in order to stabilize this huge monument, respecting the traditional one of accretion layers. What we have actually shown in this article is that the inner structure of the inclined courses can incorporate the natural forces to compact the core of the Pyramid towards the center, thus to strengthen it over time, so that we can believe that the Great Pyramid will keep standing upright almost forever though its outer faces will be weathered further. This is similar to the case of "the Roman concrete" which tightens over time by thriving in open chemical exchange with seawater, interlocking crystals. If someone will ask us why the Great Pyramid is so stable, we can answer simply, "because it gets stronger over time".

Remark 1. *Possible modified inner structure of the Great Pyramid:*

There would be various modified cores of inclined courses. Figure 32 shows an example of modified inner structure of the Great Pyramid including a thin pyramid (with the cross-section $S_2A_0S_{10}$) around the central axis, consisting of horizontal courses. Such horizontal courses would be very helpful in constructing internal structure like the King's and Queen's Chamber, and for such construction the top angle $\angle S_2A_0S_{10} = 2\theta \approx 23^\circ$ where $\tan\theta = 1/5$ would be wide enough. We note that Figure 32 is a two-dimensional figure of cross-section so that this modified part looks relatively large, but its actual three-dimensional size, i.e., volume, is very small: Let V_0 be the volume of the thin inner pyramid with the cross-section $S_2A_0S_{10}$, and V_1 be the volume of the pyramid with the

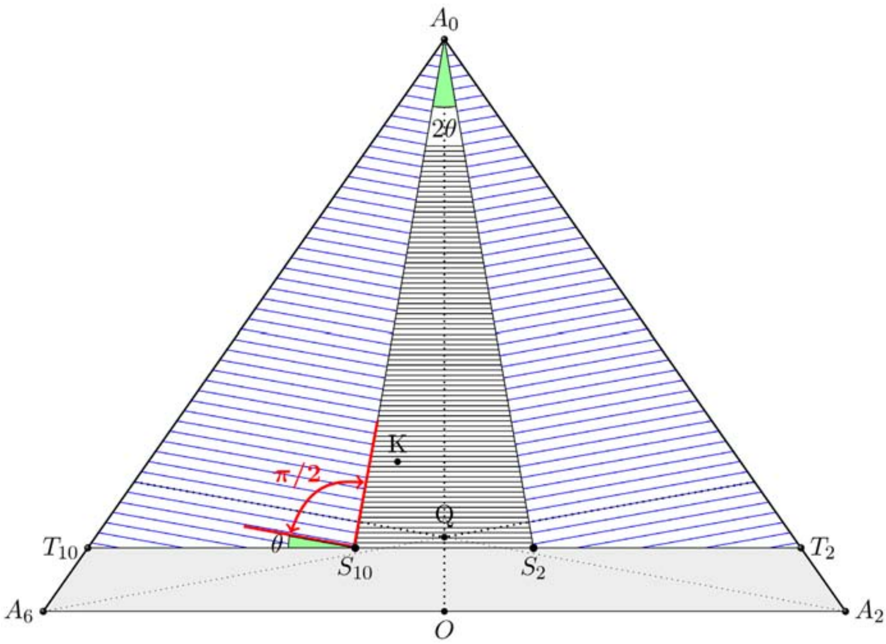

Figure 32. Cross-section of the Great Pyramid with the possible modified inner structure, including a central core of thin pyramid consisting of horizontal courses, with the vertical cross-section $S_2A_0S_{10}$ (its horizontal cross-section is like the white part of Figure 8). This thin inner pyramid has the top angle $\angle S_2A_0S_{10} = 2\theta \approx 23^\circ$ and the face angle $\angle A_0S_2S_{10} = A_0S_{10}S_2 = \pi/2 - \theta \approx 79^\circ$, where $\theta = \arctan(1/5) = 11.3\cdots^\circ$. K and Q show the positions of the King's and the Queen's Chamber, respectively, as in Figure 12; see (Creighton & Osborn, 2008) about their positions.

cross-section $T_2A_0T_{10}$ (i.e., above the light-gray part). Put $\angle OA_0A_2 = \angle OA_0A_6 = \phi$. Then, since the face angle of the Pyramid is "seked" 5 palms 2 digits, we have $\tan\phi = 5.5/7$. Hence

$$\frac{V_0}{V_1} = \frac{\overline{S_2S_{10}}^2}{\overline{T_2T_{10}}^2} = \frac{(2\tan\theta)^2}{(2\tan\phi)^2} = \left(\frac{\tan\theta}{\tan\phi}\right)^2 = \left(\frac{1/5}{5.5/7}\right)^2 = 0.064\cdots.$$

Thus, the volume of the inner thin pyramid is only about 6.5 percent of V_1, so, surely less than 6 percent of the total volume of the Great Pyramid.

Remark 2. *About the concavity in the Khafre and the Menkaure Pyramid:*

The three big pyramids of Khufu, Khafre and Menkaure were built in this order during the same Fourth Dynasty period around 2500 BC, so it would be quite natural to expect that all of their fundamental structure would be the same, i.e., all of them have the core of inclined courses. As mentioned in Section 1, Biondi & Malanga (2022) revealed the concavity of all the three pyramids, and it seems their result shows that the degree of the concavity of the Menkaure is almost the same as that of the Khufu's, but the concavity of the Khafre's is a bit shallower than the two neighboring pyramids. So, we may infer from **Table 1** that the slope of courses of the Menkaure pyramid would be the same as that of the Great Pyramid, $\tan\theta = 1/5, \theta \approx 11^\circ$, but that of the Khafre's would be about $\tan\theta = 1/8, \theta \approx 7^\circ$; then the maximal indent of the Khafre pyramid is less than 40 cm, and this small amount would be the reason why the concavity of the Khafre pyramid was not captured until now even by any Earth observation satellites, like the Quick Bird. Compared with the Great Pyramid, it is known that the internal structure of Khafre's is very simple. So, if we draw an illustration like **Figure 32**, of the Khafre's Pyramid, we do not need a wide top angle 23˚ for the inside pyramid; instead, 14˚ would be enough. Therefore, the simple structure around the central axis may be one of the reasons for the Khafre's Pyramid to have the very gentle slope of courses, about 7˚. Further we want to note that the slopes 1/5 and 1/8 would be very favoured by ancient Egyptians since, according to (Seyfzadeh, 2018b: p. 320), "the numbers five and eight were likely of special significance to the ancient Egyptians of Khufu's time originating from astronomic periods, converted to theological teaching, and possibly architecturally expressed in pyramids and mastabas".

Remark 3. *Other explanations in literatures:*

Various explanations, different from ours, have appeared about the concavity of the Great Pyramid. Let us mention six of those.

1) Mendelssohn (1973) asserts, with **Figure 33**, that "In each horizontal row of blocks a gentle grading was carried out by which the blocks at the edges were very slightly higher than those in the middle of the face. In this way the corners of each layer of packing blocks was somewhat lifted, making the whole layer slightly concave towards the apex. This method provided an addtional inward thrust which further counteracted any tendency of lateral forces to develop". This mechanism would be quite true as it is almost the same as **Figure 17**, but he believes this delicate construction was carried out throughout the whole structure,

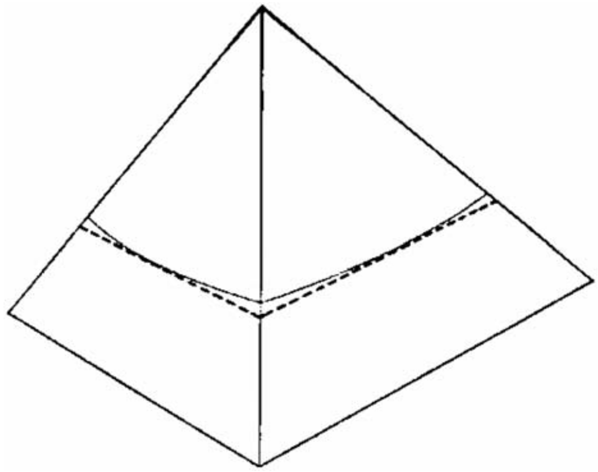

Figure 33. Illustration in (Mendelssohn, 1973) with the caption: "In order to provide additional stability, the masonry courses of the Khufu Pyramid were made slightly concave towards the apex".

as he continues that "This last mentioned safeguard was clearly a laborious and time-consuming device, requiring selection and grading of the blocks before they could be laid. It seems to have been regarded as an unnecessary precaution and was not employed at the next Giza pyramid, that of Khafre." We cannot believe such "laborious and time-consuming" efforts were made from the viewpoint of energy efficiency. It seems he also assumes that the most of blocks were "well-squared" to prevent the lateral forces, as illustrated in (a) of **Figure 22**, which we deny also from the viewpoint of energy efficiency.

2) Isler (1983) explains that the concavity is due to the efforts by the builders to control the alignment of the sides by using long cords, which led to slight variations in the levels of layers and a slight error in the alignment of the planes on each side of the faces. Our theory excludes this idea because we believe the builders of the Pyramid measured "angle" rather than "distance" knowing well that such long, hence heavy, cords cause errors in measurement.

3) Monnier (2022) insists that "the indentation of the faces of the Great Pyramid is very probably the consequence of relatively recent activities affecting the monument", which means that the cumulative effect of the repeated falls of casing blocks due to the dismantling of the casing by the Arab quarrymen, from the end of the 12th century until the 16th century, had made each surface look concave, together with the additional damage resulting from the tourists. We reject this idea because of the following reason. The dismantling of the casing was to reuse the large fine white limestones, intricately cut and beautifully polished, in order to build mosques and fortress in nearby Cairo. Then, the dismantling of the casing by quarrymen must be carried out very carefully, using some device like ropes, not to cause any damage to the polished surface of stones. Therefore, we do not think they fell down the casing stones, hitting and bumping many blocks on the way to the ground. The debris of casing stones around the base would be due to the earthquake, not due to the intentional dismantlement by the

quarrymen. Note also that quarrymen used backing stones as steps of a "ladder" to climb up or down; then it would be quite a foolish act to destroy the "ladder". We do not exclude the case that the casing was dismantled from the top to the bottom rather than from the bottom to the top, since the former would be much safer than the latter. The 1303 AD earthquake fell down or loosened almost all casing blocks of the Great Pyramid so that it was possible for quarrymen to climb up to the apex, which means they could do the dismantlement from the apex to the bottom. It seems the Khafre's Pyramid was not so disturbed by the same earthquake, but we suspect that some casing stones fell down or loosened so that the quarrymen could climb up near to the apex, from where they could start the the dismantlement towards the bottom. The dismantlement from the top to the bottom needs further care not to cause any damage to the remained casing blocks.

4) Edwards (2016) proposed that workers used the angled faces of the outer casing blocks as surfaces on which to transport block-and-sledge assemblies, and the concavity was a side effect of the construction that the external lateral forces induced by hauling block-and-sledge assemblies up the angled faces of the Pyramid. We can not believe such side effect generated the concavity with clear division of each face into two right triangular planes both of which look quite "flat" in **Figure 1** and **Figure 2**. We proposed in (Kato, 2020) another simple way to lift stones using a very simple lift (made of poles, posts and ropes) and a well (an empty column surrounded by walls of stones, like a chimney).

5) Bauval (2016)[8] proposes that the concavity encodes a "virtual space" at the top of the monument on which might have been placed a spherical object. We need more theory behind the coincidence of numbers to understand such a proposal.

6) A spiritual reason was proposed in (Seyfzadeh, 2017, 2018a: p.165) that the concavity was one of features of the Great Pyramid intentionally designed by the architect "Hemiunu" to embedd theological meaning into the Pyramid, and that the maximal indent "0.92 meters" estimated by Pochan (**Figure 4**) can be interpreted as 8 ("Khemenu") ×1/1000 ("Re-Kha"; Egyptian unit fractions were expressed with the mouth symbol Re over some denominator; kha also means "thousand") ×220 cubits (the half-base). As mentioned in the above Remark 2, or in the model **M** (5/8), it is believed (Seyfzadeh, 2018b: p. 320) that the numbers 5 and 8 were deeply embedded in Egyptian religious thought. Though we do not know if this Seyfzadeh's interpretation is more than the coincidence of numbers, we can believe the idea that the 8 sided core structure was accepted by the ancient Egyptian in favor of the number 8.

In the above six ideas, only the Mendelssohn's idea (1) treats the concavity as an intentional design for the structural stability of the Pyramid, and is closest to our's.

Remark 4. *Can we test our theory?*

How our theory of "gently inclined courses in the Great Pyramid" can be

[8]This paper misquotes the year the photo Figure 1 was taken, as noted in Footnote 1.

tested? This would be quite a difficult task. Or, we can rather say that, this difficulty made us to write down this article in order to guess the possible inner structure of the Pyramid scientifically. The perfect masonry keeps us away from seeing the internal structure of the Great Pyramid. Even though there exits some visible inner structure like passages and chambers, various adjustments or modifications would be probably done in setting blocks in order to construct such fine inner structures, so that any "local" seams on the walls of passages or chambers would not be easily identified with the "global" ones for the inclined courses. For example, in **Figure 32**, any horizontal seams on the walls of the King's and the Queen's Chamber cannot be the evidence that the Great Pyramid was built with horizontal courses. The only test we can imagine presently is to detect somehow the flow of rainwater through the Pyramid to confirm the flow like **Figure 19**.

Acknowledgements

We would like to thank the referee for pointing out the recent paper (Biondi & Malanga, 2022).

Conflicts of Interest

The author declares no conflicts of interest regarding the publication of this paper.

References

Alharbi, M. M. E. A. (2018). *Analysis of Extreme Precipitation Events over the Eastern Red Sea Coast for Recent and Future Climate Conditions.* Ph.D. Thesis, University of Birmingham.

Andrade, F. O. (1992). La construcción en Egipto. Primera Parte. *Re. Revista de Edificación, 10,* 55-65. https://doi.org/10.15581/020.10.35028

Arnold, D. (1991). *Building in Egypt, Pharaonic Stone Masonry.* Oxford University Press.

Badawy, A. (1999). Historical Seismicity of Egypt. *Acta Geodaetica et Geophysica Hungarica, 34,* 119-135.

Bauval, J. P. (2016). *The Concavity of the Great Pyramid: A Design Feature? Did the Designer Know the Meter Unit?* https://www.academia.edu/27553148

Bell, B. (1975). Climate and the History of Egypt: The Middle Kingdom. *American Journal of Archaeology, 79,* 223-269. https://doi.org/10.2307/503481

Biondi, F., & Malanga, C. (2022).Synthetic Aperture Radar Doppler Tomography Reveals Details of Undiscovered High-Resolution Internal Structure of the Great Pyramid of Giza. *Remote Sensing, 14,* Article No. 5231. https://doi.org/10.3390/rs14205231

Butzer, K. W., Butzer, E. B., & Love, S. (2013). Urban Geoarchaeology and Environmental History at the Lost City of the Pyramids, Giza: Synthesis and Review. *Journal of Archaeological Science, 40,* 3340-3366. https://doi.org/10.1016/j.jas.2013.02.018

Cacciola, P., Shadlou, M., Ayoub, A., Rashed, Y. F., & Tombari, A. (2022). Exploring the Performances of the Vibrating Barriers for the Seismic Protection of the Zoser Pyramid. *Scientific Report, 12,* Article No. 5542. https://doi.org/10.1038/s41598-022-09444-x

Creighton, S., & Osborn, G. (2008). *The Great Pyramid and the Axis of the Earth—Part 2.* Graham Hancock. https://grahamhancock.com/creightons4/

Dash, G., & Paulson, J. (2015). The 2015 Survey of the Base of the Great Pyramid. *The Journal of Egyptian Archaeology, 102,* 186-196. https://www.academia.edu/36742756 https://doi.org/10.1177/030751331610200114

De Vries, A. J., Tyrlis, E., Edry, D., Krichak, S. O., Steil, B., & Lelieveld, J. (2013). Extreme Precipitation Events in the Middle East: Dynamics of the Active Red Sea Trough. *Journal of Geophysical Research: Atmospheres, 118,* 7087-7108. https://doi.org/10.1002/jgrd.50569

Deus, H. M., Bolacha, E., Vasconcelos, C., & Fonseca, P. E. (2010) Analogue Modelling to Understand Geological Phenomena. In *Proceedings of the GeoSciEd VI.* University of Witwatersrand. https://www.researchgate.net/publication/266375082

Edwards, J. F. (2016). The Concave Faces of the Great Pyramid: An Explanation. *Technology and Culture, 57,* 909-925. https://doi.org/10.1353/tech.2016.0111

Ewais, A. Y., Ahmed, M. A., & Faried, M. (2016). *A Close Look at the Step Pyramid Restoration Project, JCHC 4.*

Groves, P. R. C., & McCrindle, J. R. (1926). Flying over Egypt, Sinai, and Palestine, In *The National Geographic Magazine 1926-09* (Vol. 10, No. 3, pp. 312-355). National Geographic. https://www.scribd.com/document/46834946/National-Geographic-1926-09

Hawass, Z. (1996). The Discovery of the Satellite Pyramid of Khufu (G1-d). In P. Der Manuelian (Ed.), *Studies in Honor of William Kelly Simpson* (pp. 379-398). Museum of Fine Arts.

Hemeda, S., & Sonbol, A. (2020). Sustainability Problems of the Giza Pyramids. *Heritage Science, 8,* Article No. 8. https://doi.org/10.1186/s40494-020-0356-9

Hubbert, M. K. (1937). Theory of Scale Models as Applied to the Study of Geologic Structures. *Geological Society of America Bulletin, 48,* 1459-1520. https://doi.org/10.1130/GSAB-48-1459

Isler, M. (1983). Concerning the Concave Faces of the Great Pyramid. *Journal of the American Research Center in Egypt, 20,* 27-32. https://doi.org/10.2307/40000899

Isler, M. (2001). *Sticks, Stones, and Shadows: Building the Egyptian Pyramids.* University of Oklahoma Press.

Kato, A. (2020). How They Moved and Lifted Heavy Stones to Build the Great Pyramid. *Archaeological Discovery, 8,* 47-62. https://doi.org/10.4236/ad.2020.81003

Khalil, A. E., Hafiez, H. E. A., Girgis, M., & Taha, M. A., (2017). Earthquake Ground Motion Simulation at Zoser Pyramid Using the Stochastic Method: A Step toward the Preservation of an Ancient Egyptian Heritage. *NRIAG Journal of Astronomy and Geophysics, 6,* 52-59. https://doi.org/10.1016/j.nrjag.2016.11.003

Kukela, A., & Seglins, V. (2013). Assessment of Stone Material Deterioration of the Exposed Surfaces of the Step Pyramid in Saqqara. *Journal of Earth Science and Engineering, 3,* 238-244.

Mendelssohn, K. (1971). A Scientist Looks at the Pyramids: Engineering Evidence Connected with the Building of the Great Pyramids Suggests Conclusions That Go Far beyond the Problems of Pyramid Design. *American Scientist, 59,* 210-220.

Mendelssohn, K. (1973). A Building Disaster at the Meidum Pyramid. *The Journal of Egyptian Archaeology, 59,* 60-71. https://doi.org/10.1177/030751337305900108

Mendelssohn, K. (1976). *The Riddle of the Pyramids.* Thames & Hudson.

Merle, O. (2015). The Scaling of Experiments on Volcanic Systems. *Frontiers in Earth Science, 3,* Article 26. https://doi.org/10.3389/feart.2015.00026

Monnier, F. (2022). The So-Called Concave Faces of the Great Pyramid. *Interdisciplinary Egyptology, 1,* 1-18.

Morsy, S. W., & Halim, M. A., (2015). Reasons Why the Great Pyramids of Giza Remain the Only Surviving Wonder of the Ancient World: Drawing Ideas from the Structure of the Giza Pyramids to Nuclear Power Plants. *Journal of Civil Engineering and Architecture, 9,* 1191-1201. https://doi.org/10.17265/1934-7359/2015.10.007

Ogilvie-Herald, C. (2020). *Climate Change and the Age of the Great Sphinx.* https://www.academia.edu/43952795/

Petrie, W. M. F. (1883). *The Pyramids and Temples of Gizeh.* Histories & Mysteries of Man Ltd.

Pochan, A. (1971). *L'énigme de la grande pyramide.* Robert Laffont.

Pollard, D. D., & Fletcher, R. C. (2005). *Fundamentals of Structural Geology.* Cambridge University Press.

Raynaud, S., de La Boisse, H., Makroum, F. M., & Bertho, J. (2008). *Geological and Geomorphological Study of the Original Hill at the Base of Fourth Dynasty Egyptian Monuments.* HAL ID: hal-00319586. HAL.

Ritner, R. K., & Moeller, N. (2014). The Ahmose "Tempest Stela", Thera and Comparative Chronology. *Journal of Near Eastern Studies, 73,* 1-19.
https://doi.org/10.1086/675069
http://www.jstor.org/stable/10.1086/675069

Schellart, W. P., & Strack, V. (2016). A Review of Analogue Modelling of Geodynamic Processes: Approaches, Scaling, Materials and Quantification, with an Application to Subduction Experiments. *Journal of Geodynamics, 100,* 7-32.
https://doi.org/10.1016/j.jog.2016.03.009

Seyfzadeh, M. (2017). The Mysterious Pyramid on Elephantine Island: Possible Origin of the Pyramid Code. *Archaeological Discovery, 5,* 187-223.
https://doi.org/10.4236/ad.2017.54012

Seyfzadeh, M. (2018a). Essential Design of the Great Pyramid Encoded in Hemiunu's Mastaba at Giza. *Archaeological Discovery, 6,* 162-172.
https://doi.org/10.4236/ad.2018.62008

Seyfzadeh, M. (2018b). Hemiunu Used Numerically Tagged Surface Ratios to Mark Ceilings inside the Great Pyramid Hinting at Designed Spaces Still Hidden within. *Archaeological Discovery, 6,* 319-337. https://doi.org/10.4236/ad.2018.64016

Weeks, K.R. (1995). The Work of the Theban Mapping Project and the Protection of the Valley of the Kings. In R. H. Wilkinson (Ed.), *Valley of the Sun Kings* (pp. 122-128). University of Arizona Egyptian Expedition.

Yasseen, A. (2018) Architecture of the Great Pyramid of Giza Concept and Construction. *Proceedings of Science and Technology, 1,* 97-108,

Zalewski, F. (2017). Petrographic Observations of the Building Stones of the Great Pyramid of Giza. *Journal of Geological Resource and Engineering, 4,* 153-168.

Archaeological Discovery, 2023, 11, 107-132
https://www.scirp.org/journal/ad
ISSN Online: 2331-1967
ISSN Print: 2331-1959

Lapis Lazuli Particles on the Turin Shroud: Microscopic Optical Studies and SEM-EDX Analyses

Gérard Lucotte[1], Thierry Thomasset[2]

[1]Institute of Molecular Anthropology, Paris, France
[2]Laboratory of Physico-Chemical Analyses, UST of Compiègne, France
Email: lucottegerard@outlook.fr

How to cite this paper: Lucotte, G., & Thomasset, T. (2023). Lapis Lazuli Particles on the Turin Shroud: Microscopic Optical Studies and SEM-EDX Analyses. *Archaeological Discovery, 11,* 107-132.
https://doi.org/10.4236/ad.2023.112005

Received: January 12, 2023
Accepted: April 1, 2023
Published: April 4, 2023

Abstract

We have studied by optical microscopy and SEM-EDX lapis lazuli particles adhering to a sample of the Turin Shroud. A total number of seventy lapis lazuli particles (and sub-particles) were found on the surface of this sample, and were characterized in details: they are little particles (of between 0.1 and 15 μm of maximal length), of blue colour, and with a spectrum of chemical elements identical to that of the lapis Lazuli mineral. We hypothetise that these particles are residues of painting layers of lapis lazuli that covered initially the Turin Shroud.

Keywords

Turin Shroud, Lapis Lazuli (LL) Particles, Optical and SEM-EDX Studies

1. Introduction

The Turin Shroud (TS) is a well known object in which a body image is imprinted. In 1978, G. Riggi di Numana took some samples of the TS, in particularly corresponding to the Face area, and deposited it on a special sticky-tape; we had access to this sticky tape (cut up in a triangular form) and realized on it preliminary investigations concerning mineral particles (Lucotte, 2012). We have since published some other studies on the triangle, concerning linen fibers (Lucotte, 2015a), pollens and spores (Lucotte, 2015b), red blood cells (Lucotte, 2015c) and hematite, biotite and cinnabar particles (Lucotte et al., 2016).

The mineral LL (Hermann, 1968) contains grains of the cubic lazurite which accounts for the deep blue colour of the ground mineral pigment. As a mineral deposit lazurite is commonly associated with other silicate minerals such as diopside ($CaMgSi_2O_6$), wollastonite ($CaSiO_3$), together with calcite ($CaCO_3$) and iron pyrite. Generally lapis lazuli can be recognized with optical microscopy or under high-magnification scanning electron microscopy and Energy Dispersive X-ray (EDX) analysis. The approximate formula of LL is $(Na, Ca)_8(Al, Si)_{12}O_24S_2$-FeS-$CaCO_3$; that of lazurite is $Na_6Ca_2Al_6Si_6O_{24}[(SO_4), S, Cl(OH)]_2$.

We have already described a little lapis lazuli particle neighbouring the P3 skin debris on the TS triangle sample (Lucotte, 2016). We report now in this study a total number of seventy particles of lapis lazuli found in different areas of the triangle surface.

2. Material and Methods

The material is a small (1.36 mm high, 614 μm wide) sticky-tape triangle (Lucotte, 2017), at the surface of which more than 2500 TS particles were deposited. For practical reasons, the surface of the triangle was subdivided into 19 areas (A to S), the E area being subdivided again in five sub-areas (Ea to Ee).

All the particles described here were studied by optical microscopy and by SEM (Scanning Electron Microscopy)-EDX analysis. Particles of interest were first observed by optical microscopy using a photo-microscope Zeiss, model III 1972. The SEM apparatus used was a Philips XL instrument (an environmental version); GSE (Gaseous Secondary Electrons) and BSE (Bask Scattered Electrons) procedures are used, the last one detecting heavy elements.

Elemental analysis for each particle were realized by EDX, this SEM apparatus being equipped with a Bruker probe AXS-EDX (the system analysis is PGT: Spirit Model, of Princeton Gamma Technology).

Each elemental analysis is given in the form of a spectrum, with kiloelectrons/Volts (ke/V) on the abscissa and elemental peak heights in ordinates. Highly-resolutive (HR) spectras are those where values along the Y axis are enhanced, that permitting a better study of small peaks.

The minimal surface necessary to an EDX analysis is of about 1 μm^2; so, particles which surfaces are below this limit give also EDX analysis of neighbouring particles.

3. Results

The 70 particles (or sub-particles) of LL found are small (of between 0 - 5 μm and 15 μm of maximal length) particles, of various forms (generally with angulous outlines). Their colours are mainly blue or clear-blue; their spectras are those of lapis lazuli particles, but they had also various contents in phosphorous.

Table 1 gives the characterisations of the first twenty-five lapis lazuli particles detected.

There is only one LL particle (a19') in the A area of the triangle. It is a small (1.5 μm of maximal length) particle, of a rectangular form. The colour observed in optic is blue and the spectrum is that of a typical LL particle. The a19' micro-particle is a small scale of lapis lazuli deposited on the a19 particle surface (which is a painting, containing barium sulphate and iron notably).

Table 1. List and characterisations of the first twenty-five lapis lazuli particles.

Numbers	Particles	Areas	Forms	Maximal dimensions	Colours	Spectras	Distinctive features
1	a19’	A	rectangular	1.5 µm	blue	in accordance	scale on a 19
2	b5’	B	squared	3 µm	blue	in accordance	Scale on b5
3	b15	B	ovoid	10 µm	clear-blue	Ca ↗	linked to b16
4	b16	B	ovoid	15 µm	clear-blue	Si, Ca ↗	Linked to b15 and b17
5	b17	B	rectangular	8 µm	dark-blue	Si, Ca, Fe ↗	linked to b16
6	b21’	B	ovoid	6 µm	non-visible	in accordance	near b21; isolated
7	b54’	B	rectangular	2.5 µm	non-visible	Na ↗	near b54; isolated
8	d11	D	ovoid	5 µm	blue	in accordance	near d12; isolated
9	d16	D	triangular	8 µm	non-visible	in accordance	isolated
10	e21	Eb, above	squared	2 µm	blue	in accordance	isolated
11	e9	Eb, below	angulous	4 µm	clear-blue	Si, Ca ↗	linked to e10
12	e10	Eb, below	angulous	4 µm	blue	in accordance	linked to e9
13	e15	Eb, below	triangular	5 µm	blue	in accordance	linked to e10
14	e16	Eb, below	angulous	6 µm	clear-blue	Si, Ca ↗	part of e14
15	e42	Ec, above	angulous	4.5 µm	clear-blue	Si, Al ↗	Stuck up to e41
16	e52	Ec, below	angulous	7 µm	blue	in accordance	linked to e53
17	e53	Ec, below	angulous	9.5 µm	clear-blue	Si, Ca ↗	linked to e52
18	e102	Ee, left	angulous	3.5 µm	blue	in accordance	linked to e102’
19	e102’	Ee, left	elongated	4.5 µm	blue	in accordance	linked to e102
20	e106	Ee, right	triangular	9 µm	clear-blue	Si, Ca ↗	linked to e105, isolated
21	e108	Ee, right	stared	7 µm	clear-blue	Si, Ca ↗	linked to e109
22	e109	Ee, right	squared	4 µm	clear-blue	Si, Ca ↗	linked to e108 and e110
23	e110	Ee, right	triangular	6 µm	clear-blue	Si, Ca ↗	linked to e109 and e112
24	e111	Ee, right	triangular	3 µm	blue	in accordance	linked to e112
25	e112	Ee, right	rectangular	7 µm	blue, with a yellow red center	Fe ↗	linked to e110 and e111

There are six lapis lazuli particles in the B area. Particle b5’ is a square particle of 3 µm of length, of blue colour and with a typical spectrum. The b5’ micro-particle is a small scale of LL deposited on the b5 particle surface (which is a phosphorite).

Particles b15, b16 and b17 are ovoid and rectangular particles of 10 µm, 15 µm and 8 µm of length, respectively. The colour of b15 is clear-blue and its spectrum is relatively rich in silicium and calcium.; the colour of b17 is dark-blue and its spectrum is relatively rich in silicium, calcium and iron (**Figure 1** and **Figure 2**).

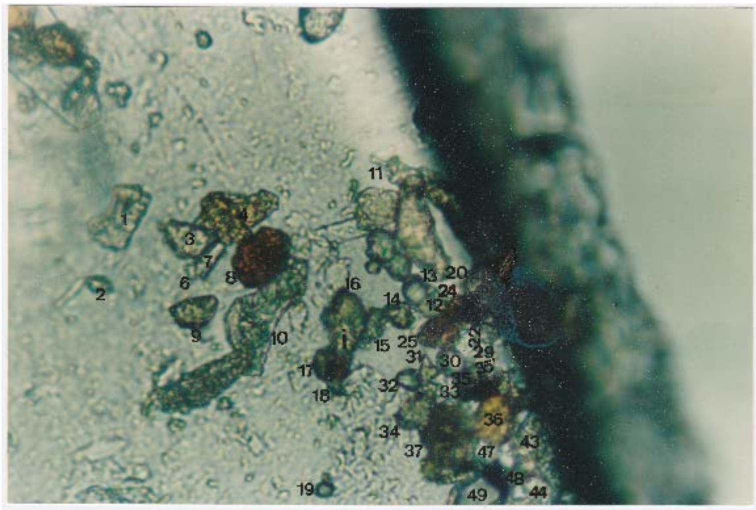

Figure 1. Optical photography (1000×) of the B area of the triangle, showing lapis lazuli particles b15, b16 and b17 (b10 and b11 are linen fibers).

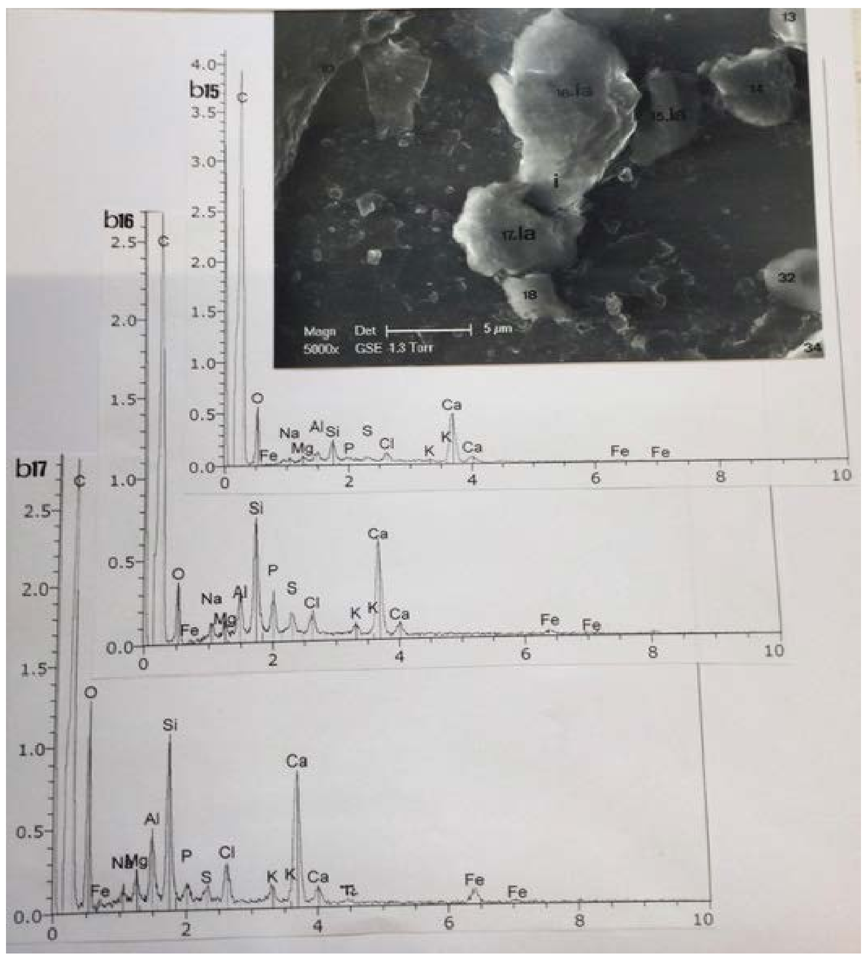

Figure 2. *Above*: SEM photograph (5000×), in GSE, showing lapis lazuli particles b15, b16 and b17 (i: the intermediate part between b16 and b17). *Below*: HR spectras of b15, b16 and b17. C: carbon; O: oxygen; Fe (three peaks): iron; N: sodium; Mg: magnesium; Al: aluminium; Si: silicium; P: phosphorous: S: sulphur; Cl: chlorine; K (two peaks): potassium; Ca (two peaks): calcium; Ti (traces): titanium.

The intermediate (i) region between b16 and b17, which is of yellow colour, is relatively rich in sulphur and iron (**Figure 3**). Particles b15, b16 and b17 are linked together.

Particle b21' is ovoid and of 6 µm of length. The colour is non-visible (because of border effect) and its spectrum is typical. The b21' particle is an isolated form, located near the b21 particle (a ceramic).

Particle b54' is rectangular and of 2.5 µm of length. The colour is also non-visible and its spectrum is relatively rich in sodium. The b54' is isolated and is a micro-scale on the b54 (a pollen) surface (Lucotte, 2015*b*).

There is no lapis lazuli in the C area. Two lapis lazuli particles (d11 and d16) are in the D area. Particle d11 is ovoid and of 5 µm of length; the colour is blue and the spectrum is typical. It is an isolated form, located near the linen fiber d12 (Lucotte, 2015a). Particle d16 is triangular and of 8 µm of length; it is an isolated form. Colour is non-visible (because it is located near the triangular border) and the spectrum is typical.

With sixteen particles (e21, e9, e10, e15, e16, e42, e52, e53, e102, e102', e106, e108, e109, e110, e111 and e112), the E area of the triangle is the richest area in LL particles.

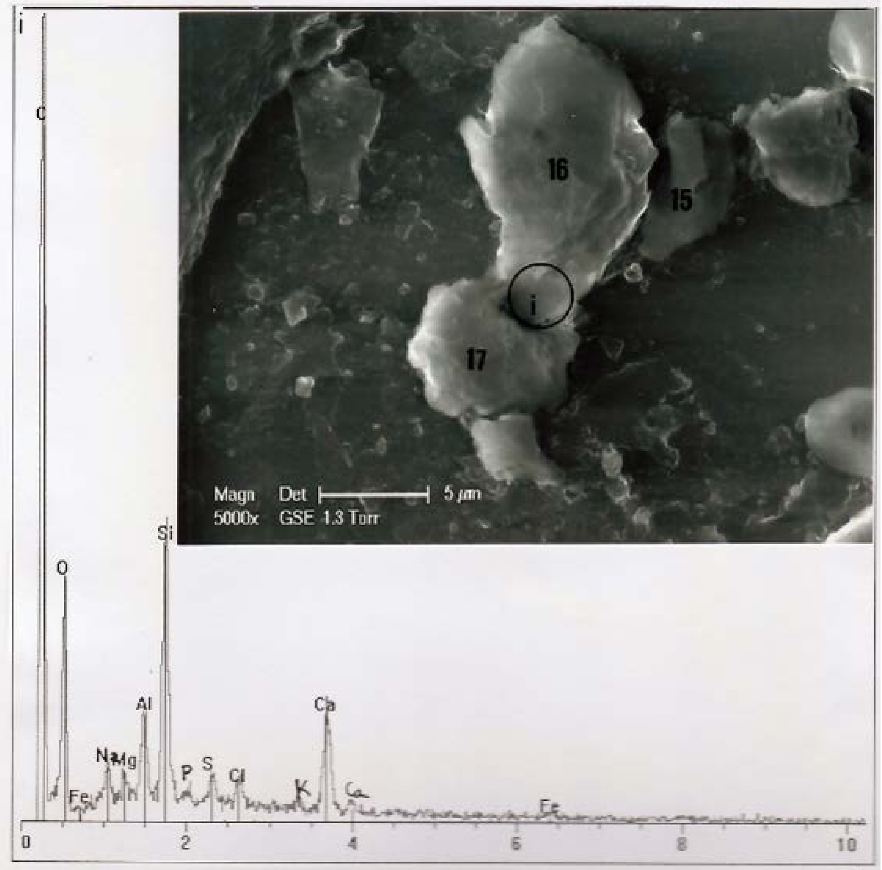

Figure 3. *Above*: SEM photograph (5000×), in GSE, showing particles b15, b16 and b17 (i is the intermediate part between b16 and b17, the circle indicating the surface being studied by EDX). *Below*: HR spectrum in the circle.

The e21 particle (located in Eb, above) is square and of 2 μm; the colour is blue and its spectrum is typical. It is an isolated form.

The e9 particle (located in Eb, below) and the e10 particle (in the same sub-area part) are angulous and of 4 μm of lengths; the colour of e9 is clear-blue and its spectrum is relatively rich in silicium and calcium. The colour of e10 is blue and its spectrum is typical. The e15 particle (also located in Eb, below) is triangular and of 5 μm of length; the colour is blue and its spectrum is typical. The e16 (in the same sub-area part) is angulous and of 6 μm of length; the colour is clear-blue and its spectrum is relatively rich in silicium and calcium. Particle e9 is linked to e10 and particle 15 to e10 also. Particle e16 is some part of e14 (which is a calcium carbonate).

Particle e42 (located in Ec, above) is angulous and of 4.5 μm of length. The colour is clear-blue and its spectrum is relatively rich in silicium and aluminium. The e42 particle is stuck up to e41 (which is an alumino-silicate of potassium, poor in iron).

The particles e52 and e53 (located in Ec, below) are angulous, with lengths of 7 μm and 9.5 μm respectively (**Figure 4**). The colour of e52 is blue and its spectrum is typical; the colour of e53 is clear-blue and its spectrum is relatively rich in silicium and in calcium. The e52 and e53 particles are linked together.

The particles e102 and e102' (located in Ee, left) are two angular and elongated

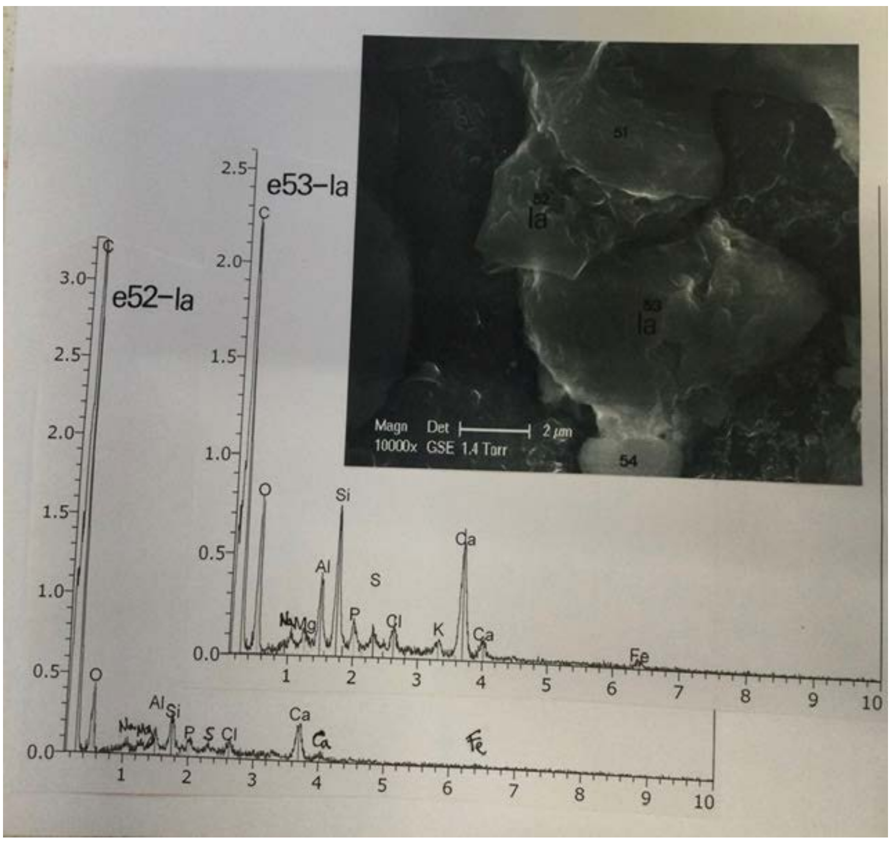

Figure 4. SEM photograph (10,000×), in GSE, showing particles e51, e53 and e54 (e51 is a Diatom and e54 a calcite). *Below*: HR spectras of e52 and e53.

particles, of respectively 3.5 µm and 4.5 µm of lengths. Their colours are blue and their spectras are typical (**Figure 5** and **Figure 6**). The e102 and e102' are linked together.

The particle e106 is triangular and of 9 µm of length (**Figure 5**). The colour is clear-blue and its spectrum is relatively rich in silicium and calcium (**Figure 6**). The e106 particle is located near linen fiber e105 (Lucotte, 2015a).

Particles e108, e109, e110, e111 and e112 (also in Ee, right) are stared, squared, triangular and rectangular, with respectively 7 µm, 4 µm, 6 µm, 3 µm and 7 µm of lengths (**Figure 5**). The colours of e108, e109 and e110 are clear blue and their spectras are relatively rich in silicium and calcium (**Figure 6** and **Figure 7**). The colour of e112 is blue with a yellow-red center and its spectrum is relatively rich in iron (**Figure 7**). The e108, e109, e110, e111 and e112 particles are linked together.

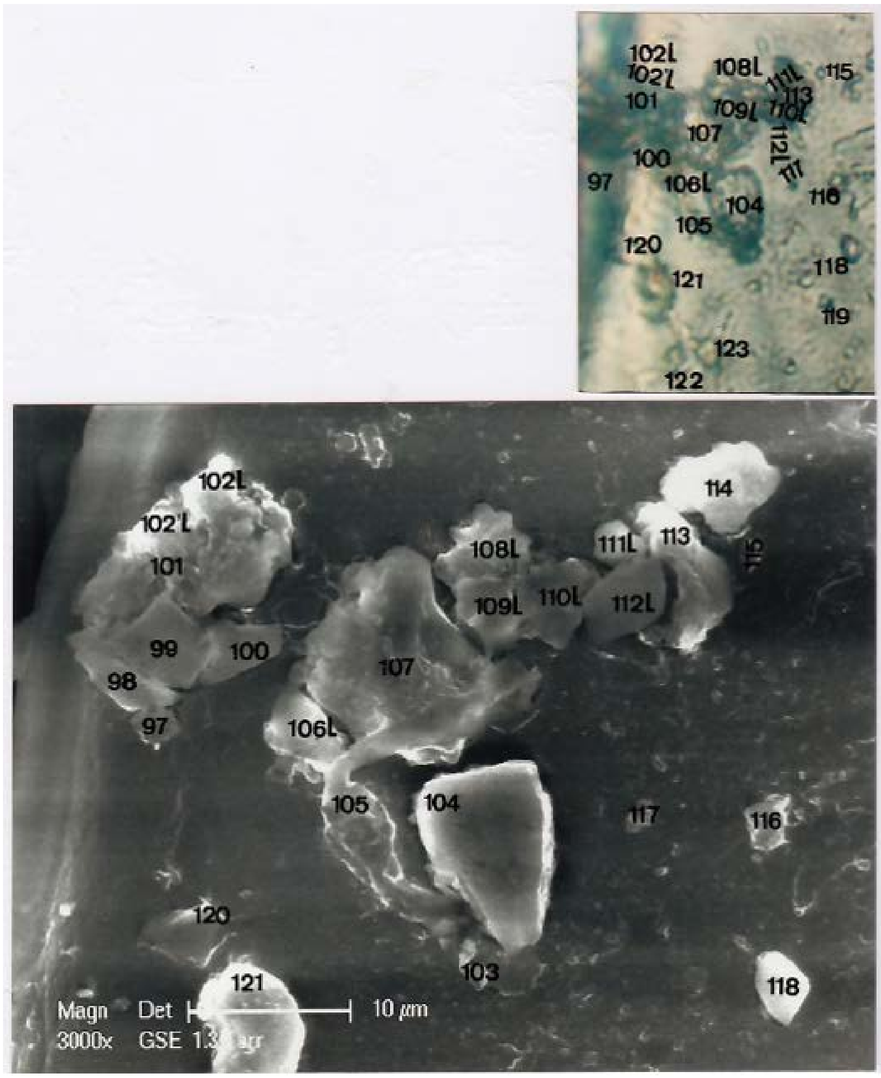

Figure 5. *Above*: optical view (1000×) of the Ec area. Below: SEM photograph (3000×), in GSE, of the Ee area showing the particles e102, e102', e106, e108, e109, e110, e111 and e112.

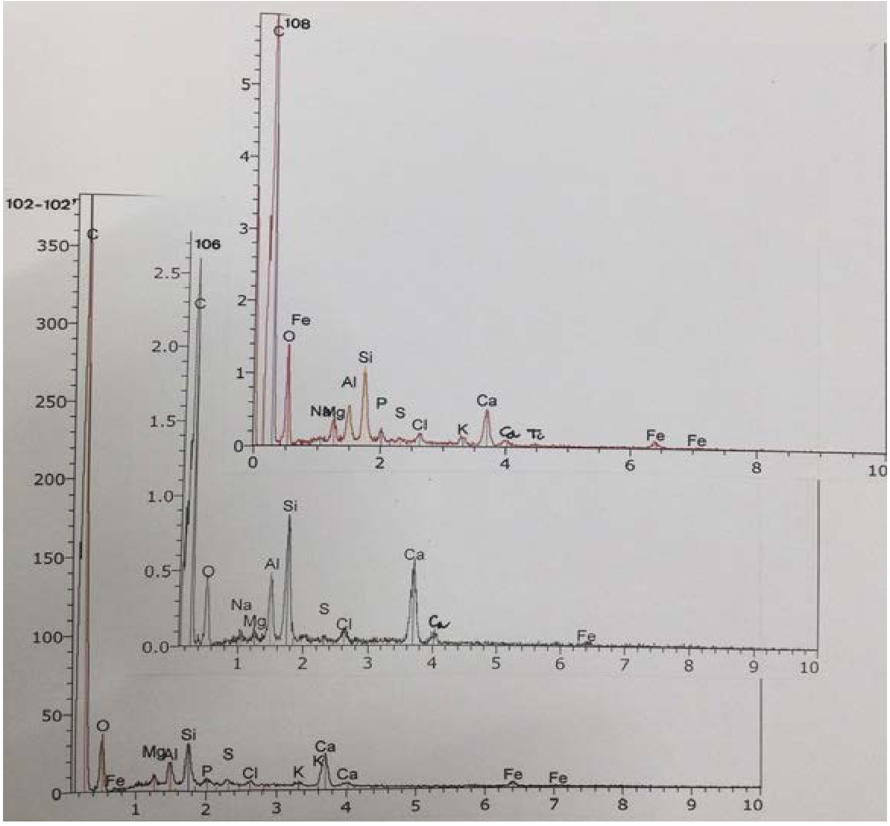

Figure 6. HR Spectras of particles e102-e102', e106 and e108.

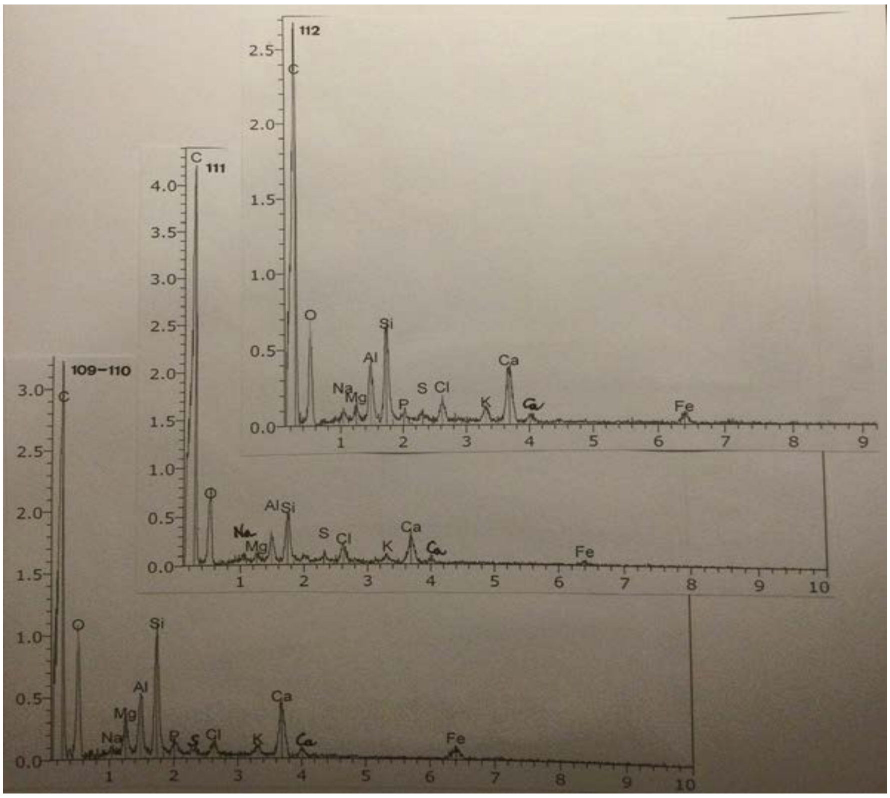

Figure 7. HR Spectras of particles e109-e110, e111 and e112.

The e98, e99 and e100 particles, linked to e101 (a red clay, rich in iron and titanium), have a special morphology (**Figure 5** and **Figure 8**): they are elongated in form, with angulous outlines and their surfaces are smooth. Their colours are intense-blue and their spectras contain copper. They are also lapis lazuli particles, but specially coloured with the blue pigment azurite, of chemical formula: $Cu_3(CO_3)_2(OH)_2$.

There is no lapis lazuli in the F area. **Table 2** gives the characterisations of the LL particles numbers 26 to 49.

Particles g72, g74, g76 and g77 (located in the G area) are angulous, triangular, quadrangular and rounded particles, of 6.5 µm, 5 µm, 6 µm and 4 µm of lengths. The colour of g72 is blue (**Figure 9**) and its spectrum is typical (**Figure 10**). The colour of g74 is clear-blue, and its spectrum is relatively rich in calcium (**Figure 11**). The colours of g76 and g77 are clear-blue, and their spectras also relatively rich in calcium (**Figure 12**). Particles g72, g74, g76 and g77 are lined

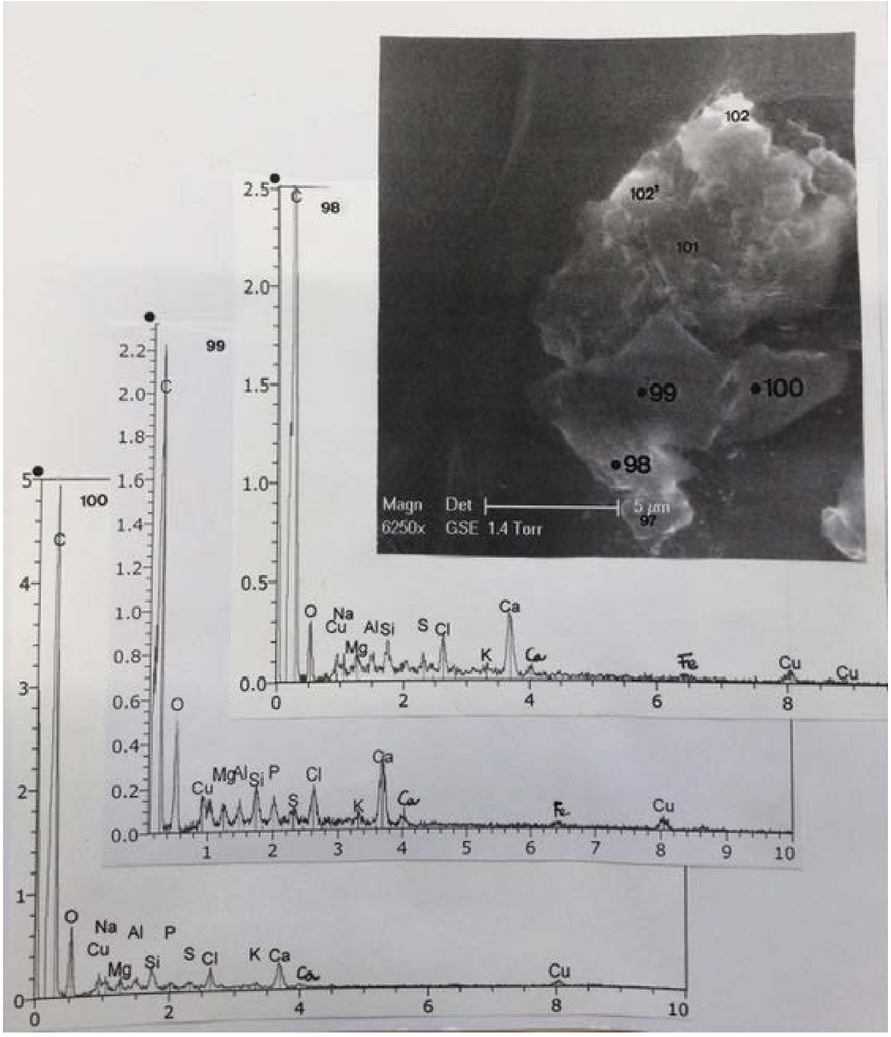

Figure 8. *Above*: SEM photograph (6250×), in GSE, showing particles e98, e99 and e100 (e102 and e102' are lapis lazuli particles; e101 is a montmorillonite; e97 is a calcium carbonate). *Below*: e98, e99 and e100 HR spectras. Cu (three peaks): copper.

Table 2. List and characterizations of the lapis lazuli particles numbers 26 to 49.

Numbers	Particles	Areas	Forms	Maximal dimensions	Colours	Spectras	Distinctive features
26	g72	G	angulous	6.5 µm	blue	in accordance	form of a crystal
27	g74	G	triangular	5 µm	clear-blue	Ca ↗	
28	g76	G	quadrangular	6 µm	clear-blue		
29	g77	G	rounded	4 µm	clear-blue		
30	g85	G	angulous	9 µm	blue border, yellow center	**Ca Fe**	isolated
31	h48	H	angulous	7 µm	blue	in accordance	isolated
32	i7'	I	triangular	1.5 µm	blue border	Si ↗	isolated
33	i50	I	rounded	5 µm	blue border	in accordance	isolated
34	i55	I	angulous	3 µm	blue border, white center	Ca ↗	isolated
35	j21-1	J right	angulous	2 µm	clear blue	in accordance	sub-particle on j21
36	j21-3	J right	squared	3 µm	blue border	in accordance	sub-particle on j21
37	j21-4	J right	elongated	4 µm	blue with yellow center	Fe ↗	sub-particle on j21
38	j24-1	J right	angulous	4 µm	clear blue	Si Ca ↗	sub-particle on j24
39	j26	J right	ondulated	3 µm	clear blue	Si Ca	linked to j28
40	j28	J right	angulous	9 µm	black-blue	Fe ↗	linked to j26
41	j28	J right	rounded	0.5 µm	clear-blue	Fe ↗	scale on j28
42	j34	J right	squared	3.5 µm	blue border with white center	Ca Fe ↗	linked to j34'
43	j34'	J right	rounded	1.5 µm	blue border with white center	CaFe ↗	linked to j34
44	j38	J left	angulous	3.5 µm	blue	in accordance	near j38
45	j39	J left	rounded	1.5 µm	blue	in accordance	near j39
46	j40	J left	rounded (bipartite)	3.5 µm	clear blue	Ca ↗	near j39
47	k64	K left	angulous	3 µm	clear-blue	Ca ↗	linked to k66
48	k65	K left	angulous	6.5 µm	blue border, with a yellow center	Ca, Fe ↗	linked to k66
49	k66	K left	angulous	5 µm	blue	in accordance	linked to k64 and k65

up; intermediate particles g72' (adjacent to g72) and g78 (adjacent to g77) are colourings containing copper.

Particle g85 (also located in the G area) is an isolated LL particle which is angulous and of 9 µm of length. Its colour is with a blue border and a yellow center; its spectrum is relatively rich in calcium and iron.

There is only one lapis lazuli particle in the H area: h48. It is angulous and of 7 µm of length. The colour is blue and the spectrum typical.

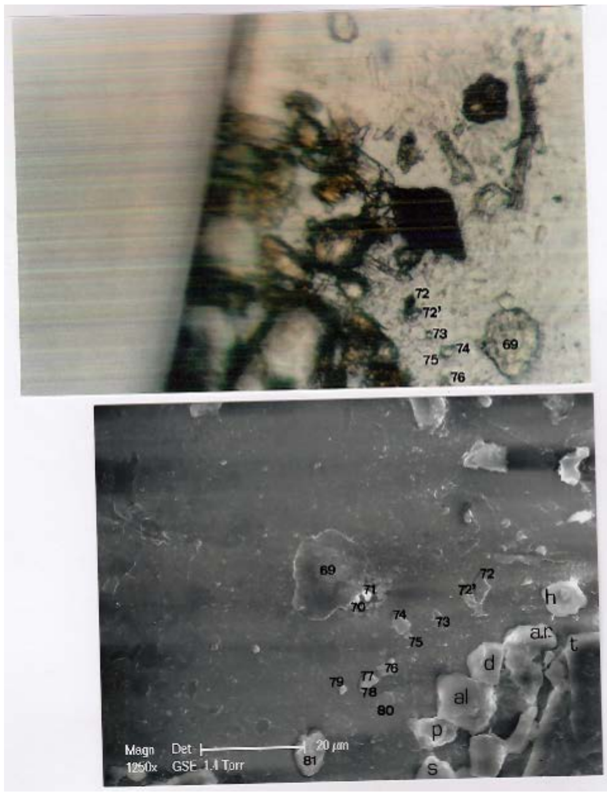

Figure 9. *Above*: inverted optical view (1000×) of the G area, showing particles g72, g72’, g73, g74, g75 and g76. *Below*: SEM photograph (1250×), in GSE, of the part of the area G showing particles g72, g72’, g73, g74, g75, g76, g77 and g78 (g78’ is a colourant, with copper, g73 is a Diatom, g75 is a dolomite; g78 is a colourant; g79 is a ceruse; g80 is a colourant, with copper).

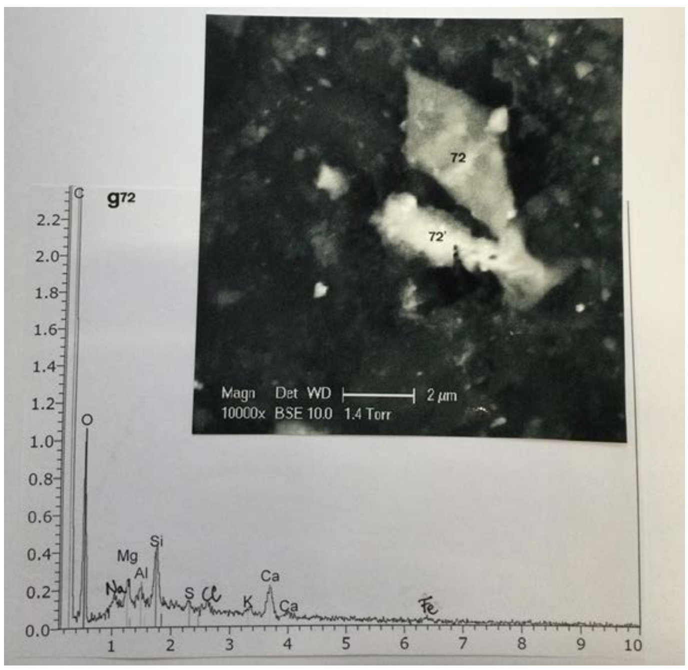

Figure 10. *Above*: SEM photograph (10,000×), in BSE, showing particles g72 and g72’. *Below*: the g72 HR spectrum.

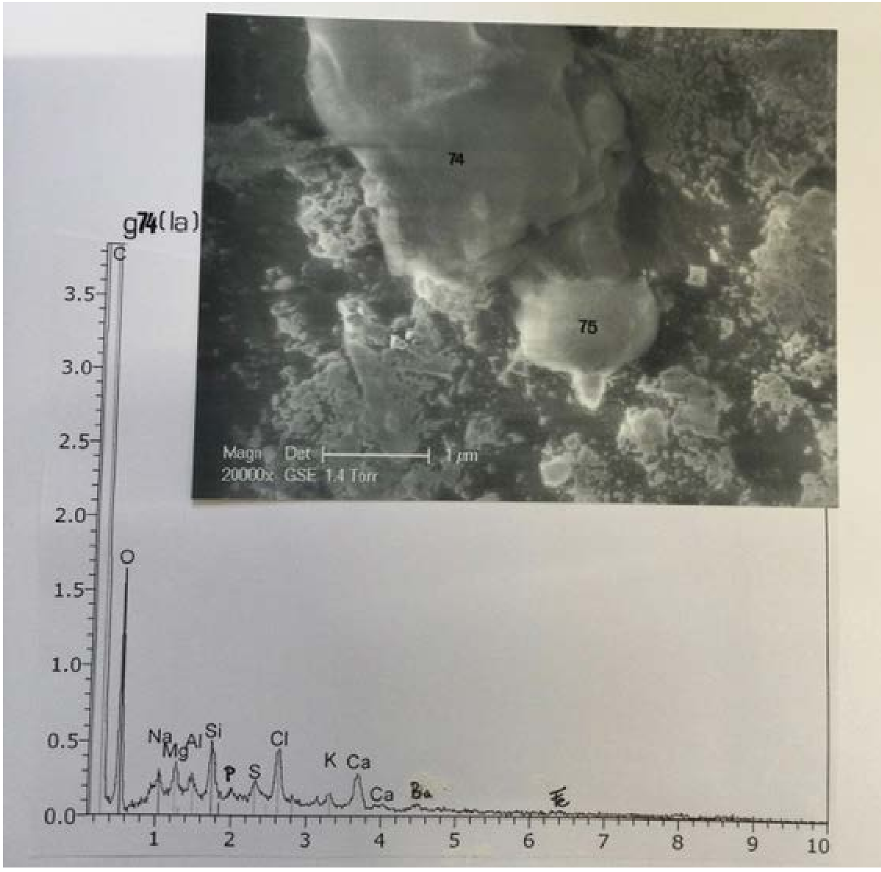

Figure 11. *Above*: SEM photograph (20,000×), in GSE, showing particles g74 and g75. *Below*: the g74 HR spectrum. Ba: barium.

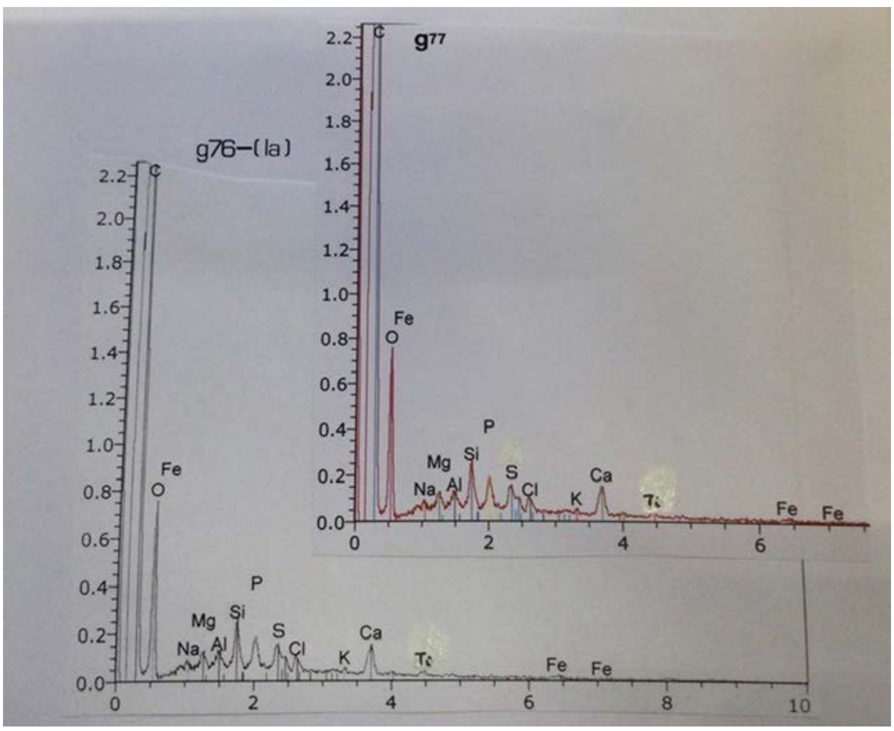

Figure 12. HR Spectras of g76 and g77 particles.

There are three lapis lazuli particles (each are isolated forms) in the I area: i7', i50 and i55. Particle 7' (**Figure 13**) is triangular and of 1.5 µm of length; its colour is with a small blue border and its spectrum relatively rich in silicium. Particle i50 (**Figure 14**) is round and of 5 µm of length, its colour is with a blue border also and its spectrum is typical. The particle i55 is angulous and of 3 µm of length; its colour is also with a blue border but with a white center; its spectrum is relatively rich in calcium.

There are twelve lapis lazuli particles (j21-1, j21-3, j21-4, j24-1, j26, j28, j28', j34, j34' located in J-right, and j39 and j40 (located in J left) in the J area. The j21-1, j21-3 and j21-4 are angulous, squared and elongated, of 2 µm, 3 µm and 4 µm of lengths respectively. Colour of j21-1 is clear-blue and its spectrum is typical. Colour of j21-3 is with a blue border, and its spectrum is also typical. Colour of j21-4 is with a blue border and with a yellow center, and its spectrum is relatively rich in iron. Particles j21-1, j21-3 and j21-4 are sub-particles loaded on the J21 particle (which is a PVC plastic).

The particle j24-1 is angulous and of 4 µm of length. The colour is clear-blue and its spectrum is rich in silicium and in calcium. Particle j24-1 is a sub-particle loaded on the j24 particle (another PVC plastic).

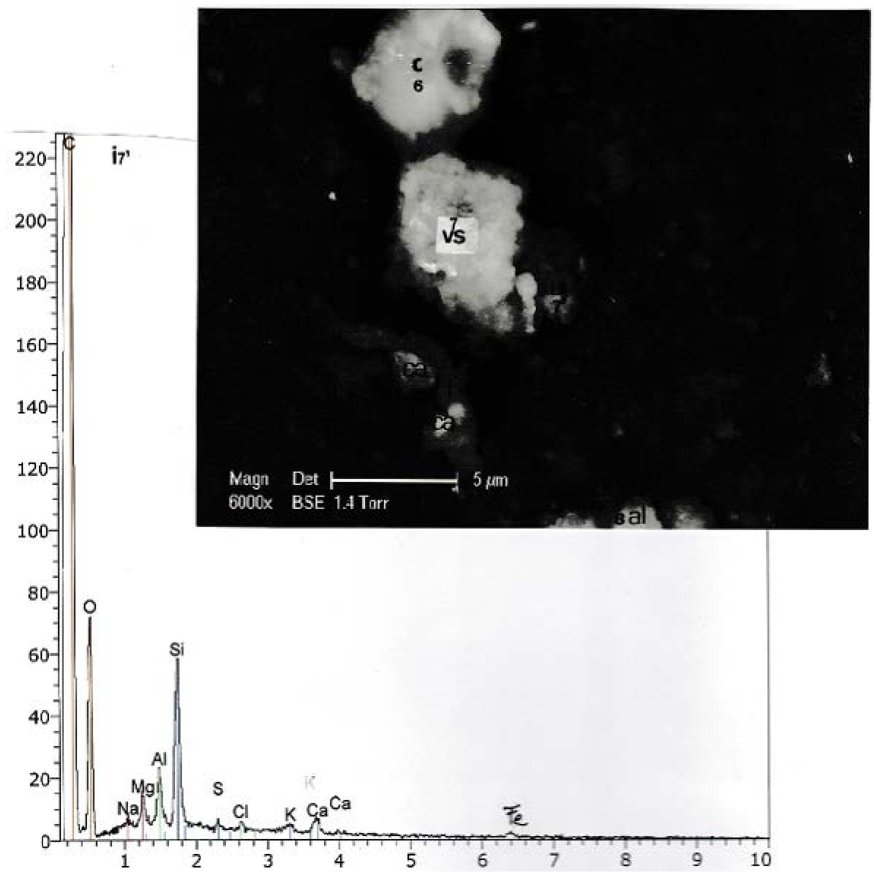

Figure 13. *Above*: SEM photograph (6000×), in BSE, of a part of the I area showing the i7' particle (i6 is a calcium carbonate, i7 is a sodic glass; ca: calcites; f is a fiber; i8 is an alumine. *Below*: the i7' spectrum.

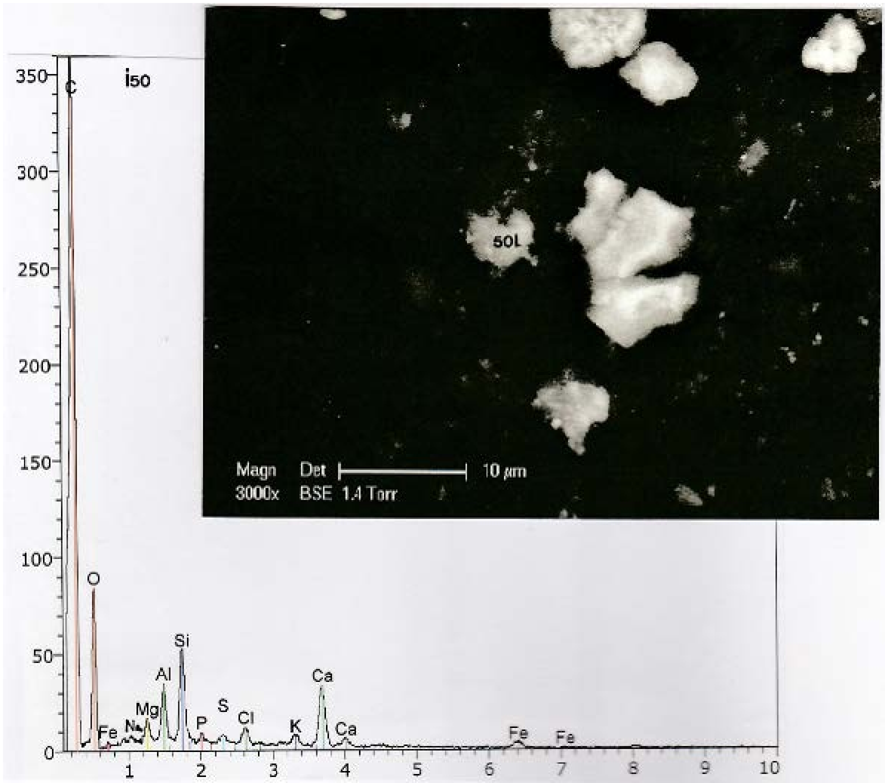

Figure 14. *Above:* SEM photograph (3000×), in BSE, of another part of the I area showing the i50 particle. *Below*: the i50 HR spectrum.

Particles j26, j28 and j28' are ondulated, angulous and round particles, of respectively 3 µm, 9 µm and 0.5 µm of lengths. (**Figure 15**). The colour of j26 is clear-blue and its spectrum relatively rich in silicium and calcium (**Figure 15**). The j26 particle is linked to j28. The j28 colour is black-blue and its spectrum is relatively rich in iron (**Figure 16**). The j28' colour is clear-blue and its spectrum is relatively rich in iron (**Figure 16**). The j28'particle is a little scale located on the inferior right part of j28.

Particles j34 and j34' are squared and rounded, with respectively 3.5 µm and 1.5 µm of lengths (**Figure 17**). Colour of j34 is with a blue border and a white center, and its spectrum is relatively rich in calcium and iron. Colour of j34'is clear-blue and its spectrum is also relatively rich in calcium and in iron. The j34 and j34'particles are linked together; at their proximity, the j32 particle is a colouring containing copper.

Particles j38, j39 and j40 (located in J, left) are neighbouring angulous and round particles, of respectively 3 - 5 µm, 1.5 µm and 3.5 µm of lengths (**Figure 18**). The j 38 and j39 colours are blue and their spectras typical. Colour of j40 (**Figure 19**) is clear-blue and its spectrum is relatively rich in calcium.

Particles k64, k65 and k66 (located in the K left part) are angulous particles linked together, respectively of 3 µm, 6.5 µm and 5 µm of lengths (**Figure 20**). The k64 colour is clear-blue and its spectrum relatively rich in calcium. The k64 colour is with a blue border and its spectrum relatively rich in calcium. The k65

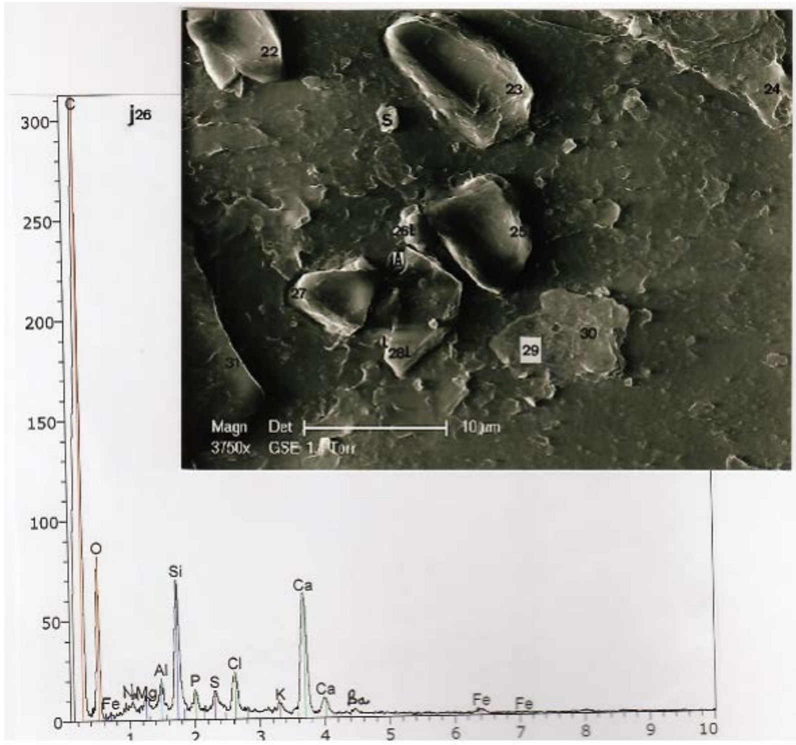

Figure 15. *Above*: SEM photograph (3750×), in GSE, showing the j26, j28 and j28' particles. *Below*: HR spectrum of j26.

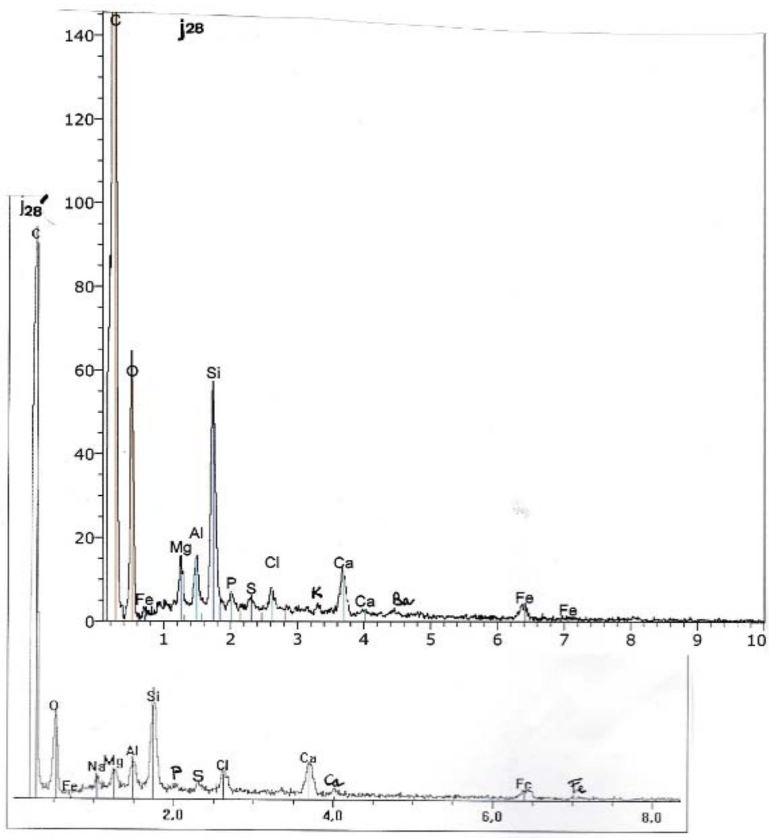

Figure 16. HR spectras of j28 and j28' particles.

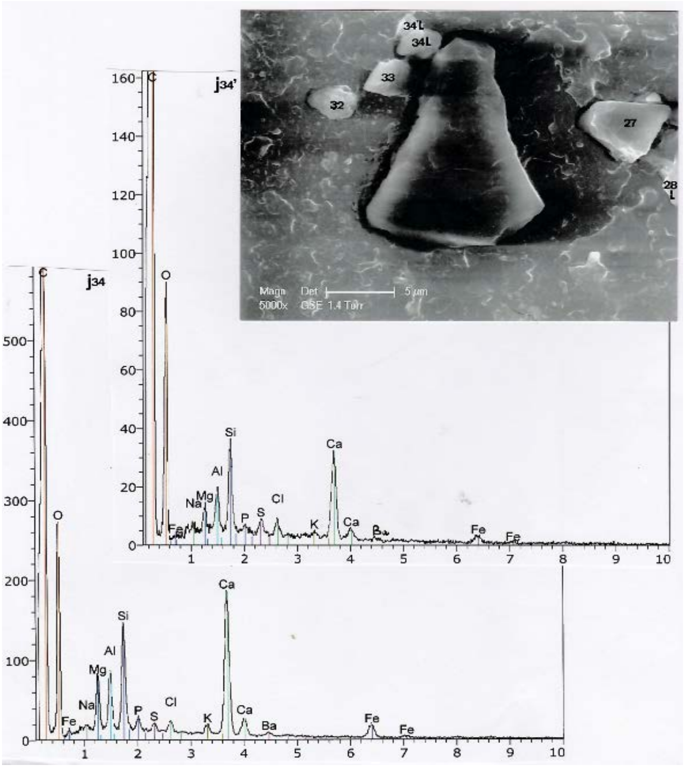

Figure 17. *Above*: SEM photograph (5000×), in GSE, of some part of the J area (J right), showing particles j34 and j34' (j27 is a silice particle; j28 is a lapis lazuli; j32 is a colourant, with copper, j33 is a calcium carbonate). *Below*: HR spectras of j34 and j34' particles.

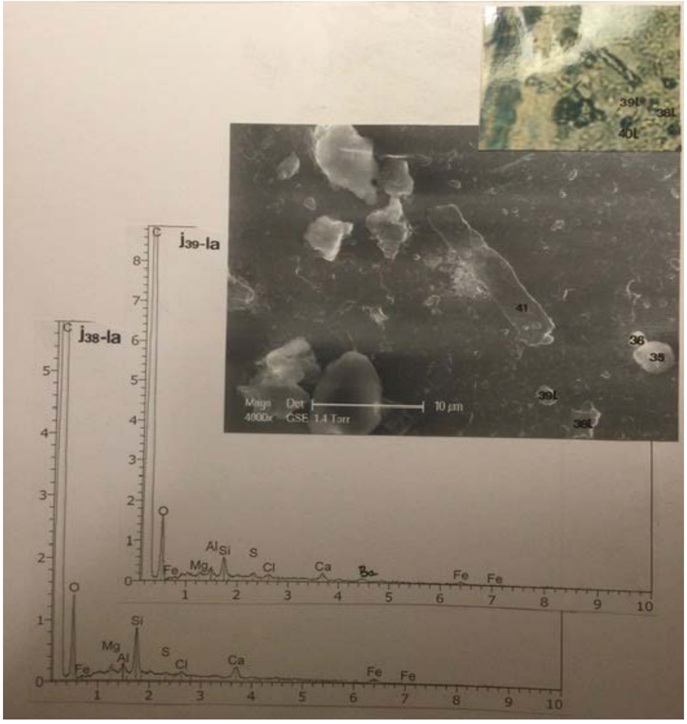

Figure 18. *Above*: optical photograph (1000×), in GSE, of some part of the J area (J left). *Middle*: SEM photograph (1000×) of some part of this I left area showing particles j38 and j39. *Below*: spectras of j38 and j39 particles.

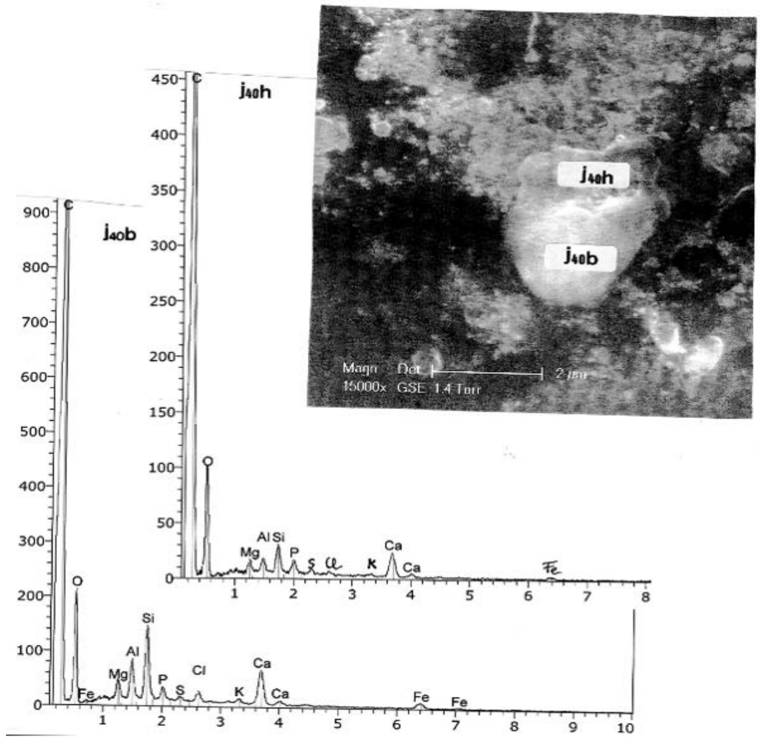

Figure 19. *Above*: SEM photograph (15,000×), in GSE, of the j40 particle (in two parts: j40h and j40b). *Below*: HR spectras of j40h and j40b.

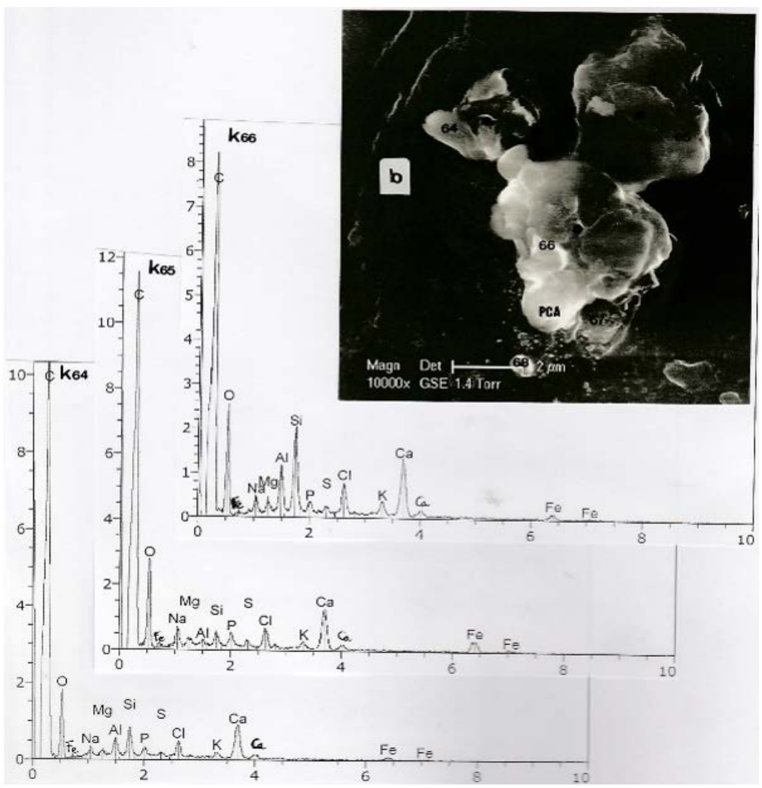

Figure 20. *Above*: SEM photograph (10,000×), in GSE, showing k64, k65 and k66 particles (b is the triangle border of the K area; k67 is a calcium carbonate; k68 is a double carbonate; PCA is a region rich in calcium phosphate. *Below*: spectras of k64, k65 and k66 particles.

colour is with a blue border and a yellow center, and its spectrum is relatively rich in calcium and in iron. The k66 colour is blue and its spectrum is typical.

Table 3 gives the characterisations of the lapis lazuli particles numbers 50 to 70.

Particles l36, l38-15 and l38', located in area L, are angulous and round, and respectively of 2.5 µm, 1 µm and 4 µm of lengths. The l36 colour is clear-blue and its spectrum is relatively rich in calcium. The colours of l38-15 and l38' are blue, and their spectras are typical. Particle l36 is loaded at the superior right side of l38 (a particle of wax); l38-15 is deposited on l38, and l38' is loaded at the inferior left side of l38.

Particle l60 is an isolated particle (located in part L, left) that is triangular and

Table 3. List and characterisations of the lapis lazuli particles numbers 50 to 70.

Numbers	Particles	Areas	Forms	Maximal dimensions	Colous	Spectras	Distinctive Features
50	l36	L	angulous	2.5 µm	clear-blue	Ca ↗	scale on the upper part of e38
51	l38-15	L	angulous	1 µm	blue	in accordance	scale on l 38
52	l38'	L	rounded	4 µm	blue	in accordance	scale on left part of l38
53	l60	L, left	triangular	5 µm	blue border and yellow center	Fe ↗	isolated
54	m31	M	rectangular	1.5 µm	blue	in accordance	isolated
55	m37	M	triangular	4.5 µm	blue-sky	Ca, Fe ↗	isolated
56	n2	N	elongated	5 µm	blue	in accordance	on the same line
57	n4	N	angulous	6 µm	blue	in accordance	on the same line
58	n5	N	rounded	1 µm	blue	in accordance	on the same line
59	n31	N	rounded	3 µm	blue	in accordance	isolated
60	o11	O	angulous	8 µm	clear-blue	Si ↗	linked to o11'
61	o11'	O	rounded	8 µm	clear-blue	Si ↗	linked to o11
62	o20	O	triangular	4 µm	blue	in accordance	isolated
63	p3	P	triangular	3 µm	blue and a white center	Ca ↗	isolated
64	p11	P	elongated	4 µm	blue and a white center	Ca ↗	linked to p12
65	p12	P	elongated	4 µm	blue	in accordance	linked to p11
66	p31	P	squared	5 µm	blue	in accordance	isolated
67	q2	Q	rectangular	6 µm	blue and yellow	Cl, Ca, Fe ↗	near q4a
68	q4a	Q	elongated	6 µm	blue	in accordance	under q4b
69	q4b	Q	rectangular	8 µm	black-blue	in accordance	above q4a
70	s14	S	elongated (multi-part)	15 µm	clear-blue	ClCa ↗	isolated

of 5 μm of length. Colour of l60 is with a blue limit and a yellow center, and its spectrum is relatively rich in iron.

Particles m31 and m37 are two isolated particles located in the M area. They are rectangular and triangular and with respectively 1.5 μm and 4.5 μm of lengths. Colour of m31 is blue and its spectrum is typical. Colour of m37 is blue sky and its spectrum is relatively rich in calcium and iron.

Particles n2, n4 and n5 are three neighbouring particles on the same line located in area N. These particles are elongated, angulous and round, of respectively 5 μm, 6 μm and 1 μm of lengths. Colours of these three particles are blue, and its spectras are typical.

Particle m31 is an isolated and round particle of 3 μm of length. Its colour is blue and its spectrum is typical.

Particles o11 and o11' are two linked particles located in area O. They are angulous and round, and both of 8 μm of length. Their colours are clear-blue and their spectras relatively rich in silicium.

Particle o20, also located in O, is an isolated triangular particle, with a length of 4 μm; the colour is blue and the spectrum is typical.

They are four LL particles in the P area: p3, p11, p12 and p31. Particle p3 is an isolated triangular particle of 3 μm of length; its colour is blue and white and its spectrum is relatively rich in calcium. Particles p11 and p12 are two elongated and linked particles of 4 μm of lengths. The colour of p11 is blue and white and its spectrum is relatively rich in calcium. The colour of p22 is blue and its spectrum is typical.

Figure 21 shows the p5 particle. It is a rectangular particle of about 13 μm of length. Its colour is black-blue and its spectrum is typical of that of a lazurite.

The p31 particle is an isolated and square particle of 5 μm of length. The colour is blue and the spectrum is typical.

There are three lapis lazuli particles in the Q area: q2, q4a and q4b. Particle q2 is rectangular and of 6 μm of length; the colour is with a blue border and an internal yellow micro-ball; its spectrum is relatively rich in chlorine, in calcium and in iron.

Particle q4a (neighbouring q2) is located under q4b. It is an elongated particle of 6 μm of length; the colour is blue and its spectrum typical. The particle q4b is rectangular, of 8 μm of maximal length, and with an intense black-blue colour. Its spectrum is typical.

There is no lapis lazuli in the R area.

The s14 particle is the only lapis lazuli particle found in the S area. It is a voluminous (but truly multipart) elongated particle of about 15 μm of length (Figure 22); the colour is clear-blue and the spectrum is relatively rich in chlorine and calcium.

4. Discussion

Every area of the triangle (but areas C, F and R) contains at least one (particles

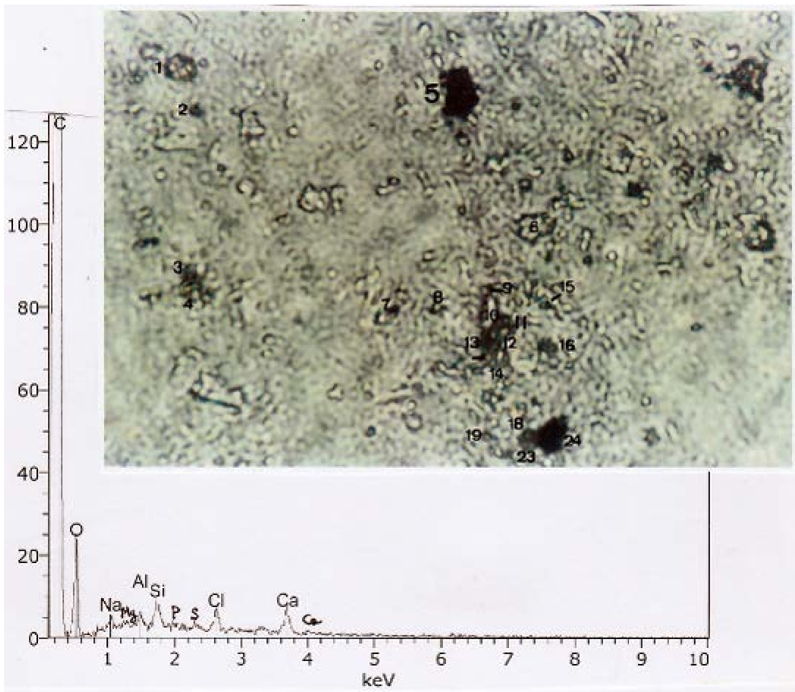

Figure 21. *Above*: optical photograph (1000×) of some part of the P area showing particles p1-p24 (p3, p11 and p12 are lapis lazuli particles). *Below*: HR spectrum of p5 (a lazurite particle).

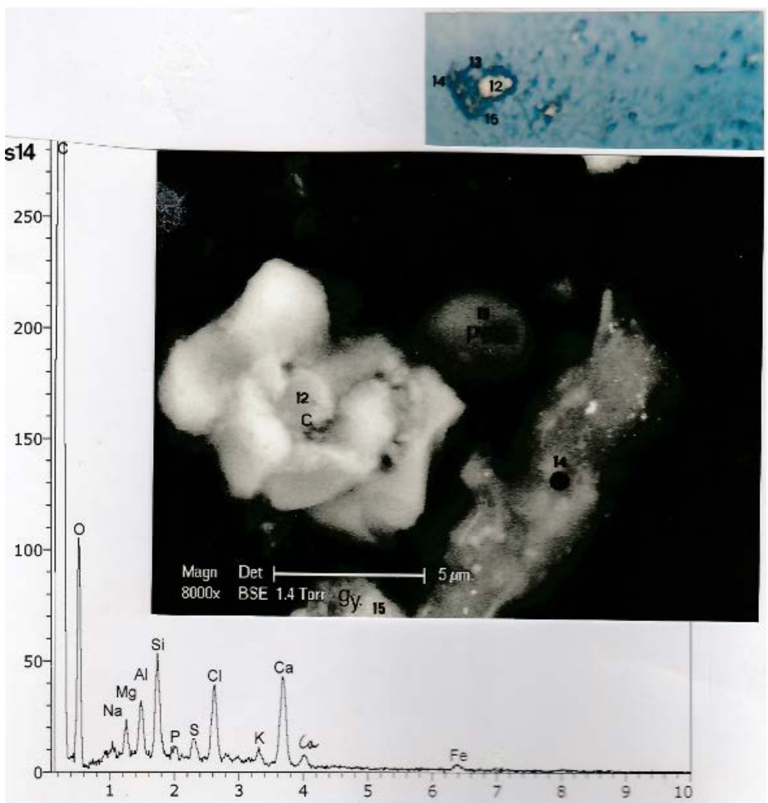

Figure 22. *Above*: inverted optical view (1000×) of some part of the S area showing s12, s13, s14 and s15 particles. *Middle*: SEM photograph (8000×), in BSE, showing the s14 particle (s12 is a Coccolith; s13 is a PVC plastic; s15 is a gypsum). *Below*: HR spectrum of s14.

h48 and s14) lapis lazuli particle. Areas containing the most important numbers of particles are area E (sixteen lapis lazuli particles) and area J (twelve particles). Figure 23 shows the locations on the surface of the triangle of all the seventy lapis lazuli detected: locations of the most important density of lapis lazuli detected (areas E and J) correspond to those richest in particles in general.

The forms of these lapis lazuli particles are generally with angulous outlines, and they are most rarely round. They are little particles, of between 0.5 µm and 15 µm of maximal lengths. Figure 24 shows the distribution of particle sizes (in each class of 2 µm of length); in this diagram the particles of 0.5 to 1.5 µm correspond to lapis lazuli sub-particles (like j28') and those of 10 to 15 µm to composite (like s14) lapis lazuli particles. The modal class of the diagram correspond to particles of between 4 and 5.5 µm of length.

When visible, lapis lazuli particles are generally of blue (or clear-blue) colour; their centers are yellow, red or white.

As a lapis lazuli jewel of reference, we studied the samples of a ring jewel. Figure 25 shows a SEM photograph of three grains of the powder scraped on the surface of this jewel. Although the proportions of the different elements varied between the three samples (Figure 25 and Figure 26), the three main components of lapis lazuli (Si, Al and Mg for the silicate; Ca for the calcite and for other minerals mainly componed of calcium; S and Fe for the pyrite FeS_2) are present

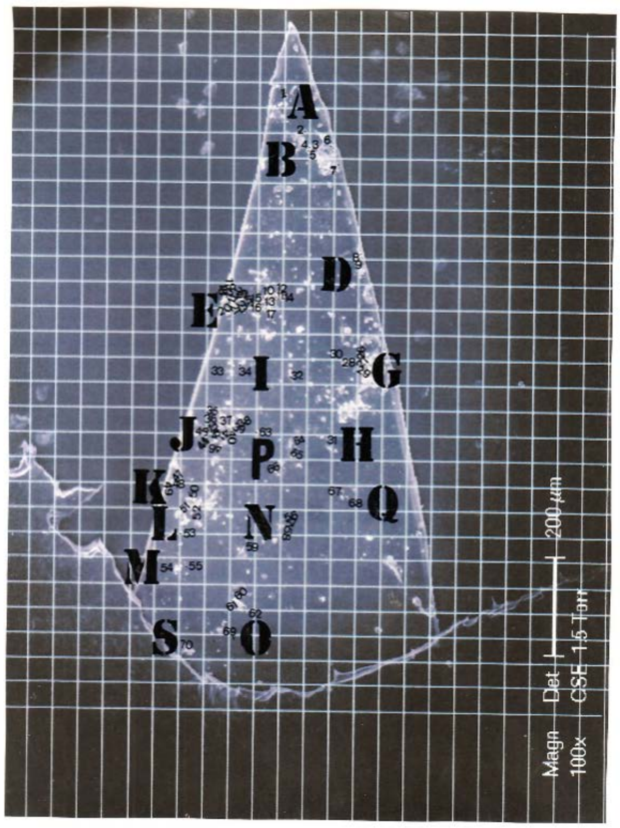

Figure 23. Locations of the 70 lapis lazuli particles detected on the areas concerned of the surface of the triangle.

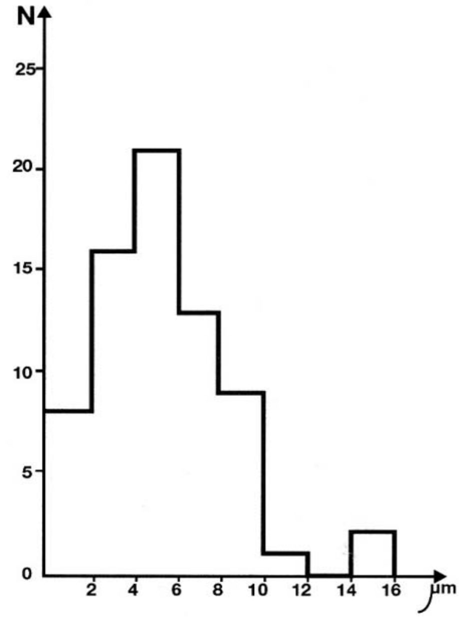

Figure 24. The modal distribution (N: numbers) of the 70 lapis lazuli particles detected among their maximal lengths (in μm).

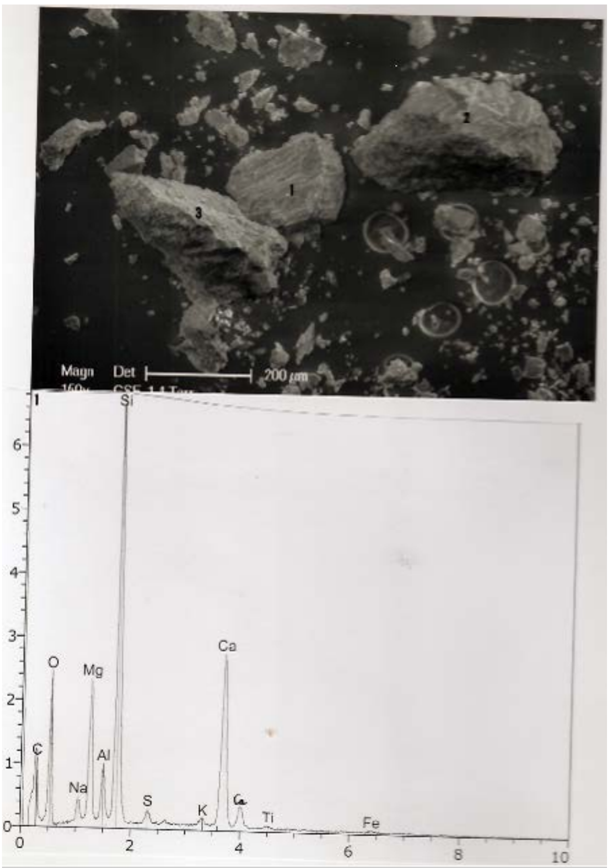

Figure 25. Powder of a ring of lapis lazuli used as reference. *Above*: SEM photograph (150×) in GSE, of three (**1**, **2** and **3**) parts of the powder. *Below*: spectrum of part **1**. C: carbon; O: oxygen; Na: sodium; Mg: magnesium; Al: aluminium; Si: silicium; S: sulphur; K: potassium; Ca (two peaks): calcium; Ti (traces): titanium; Fe (traces): iron.

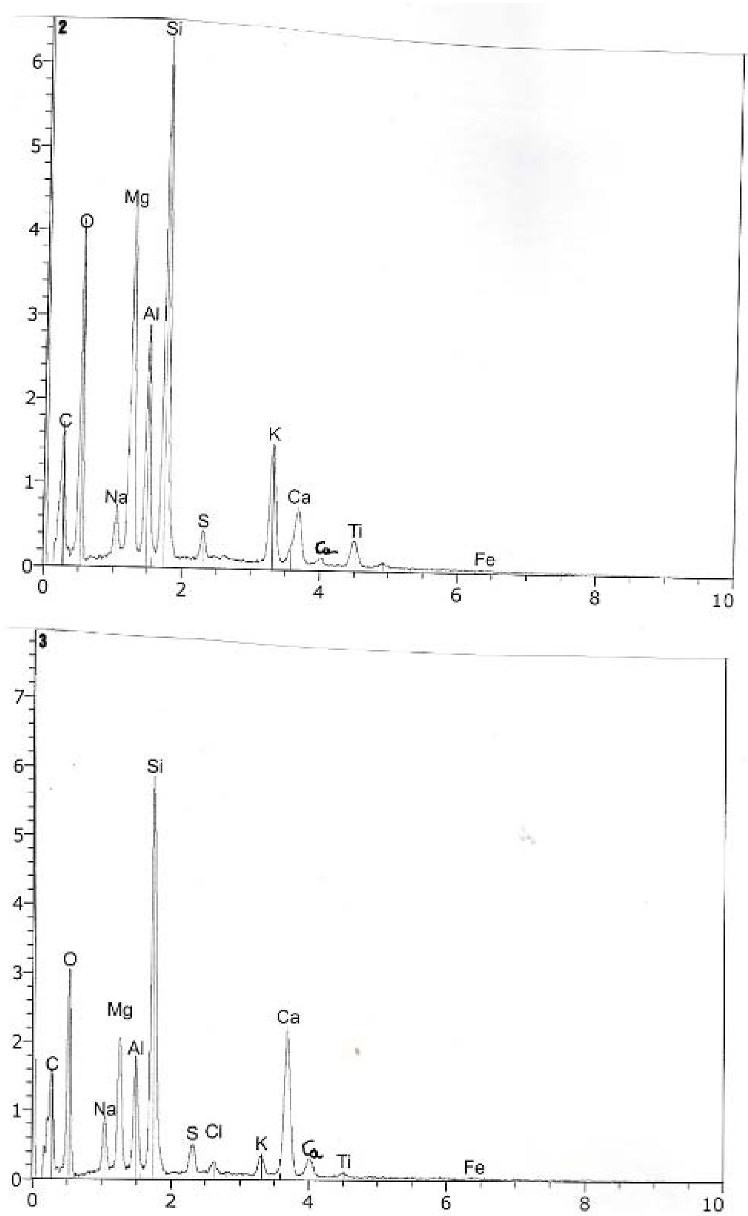

Figure 26. *Above*: spectrum of part **2**. *Below*: spectrum of part **3**.

in the three corresponding spectras.

For our seventy lapis lazuli particles of the TS observed in optical photography, we noted only a weak tendency between the blue colour of the particles with relatively small amount of the calcium element, between the clear-blue colour and relatively elevated level of this element, between the dark-blue colour and relatively elevated values of potassium and sodium, between white in the center of particles and calcium level, and between yellow and red colours in the center and relatively elevated level of iron.

Many lapis lazuli particles of the triangle (like a19', b5', b21', b54', d11, d16, e21, e42, e106, g85, h48, i7', i50, i55 and j26) are isolated, in the sense that they are not closely linked to other particles of the triangle surface. But other particles (e52 and e53, e102 and e102’, j28 and j28’, j34 and j34’, o11 and o11’, p11 and p12, and q4a and q4b) are linked in pairs, or in groups of three (b15, b16 and b17; e9, e10 and e15; k64, k65 and k66). The most numerous association between particles is that of the five particles e108, e109, e110, e101 and e112 (**Figure 5**).

But other particles -although separated—are oriented on the same line, as the three particles,n2, n4 and n5; the most numerous case of separated, but oriented particles on the same line, is that the four particles g72, g74, g76 and g77 (**Figure 9**).

These patterns of close associations between particles (or of oriented separate particles on lines) are suggestive of layers of paints formed of lapis lazuli particles on the triangle surface. In that view, isolated particles were residues of these layers covering initially the tissue, after the numerous washings of the Turin Shroud at the time of its long history.

What sort of lapis lazuli mineral pigment is it? Certainly not the artificial ultramarine pigment synthetized in 1828 by J.B. Guimet and that was subsequently adopted as blue by European artists. The approximate formula of ultramarine is $Na_{6-10}\ Al_6Si_60_{24}S_{2-4}$, and so it does not contain calcium (contrary to lazurite).

Among the lapis lazuli particles of the triangle, we observed a quasi-cubic lazurite particle with a deep blue colour (**Figure 21**). Its spectrum is identic (but Cl) to that of a lazurite mineral of reference (**Figure 27**).

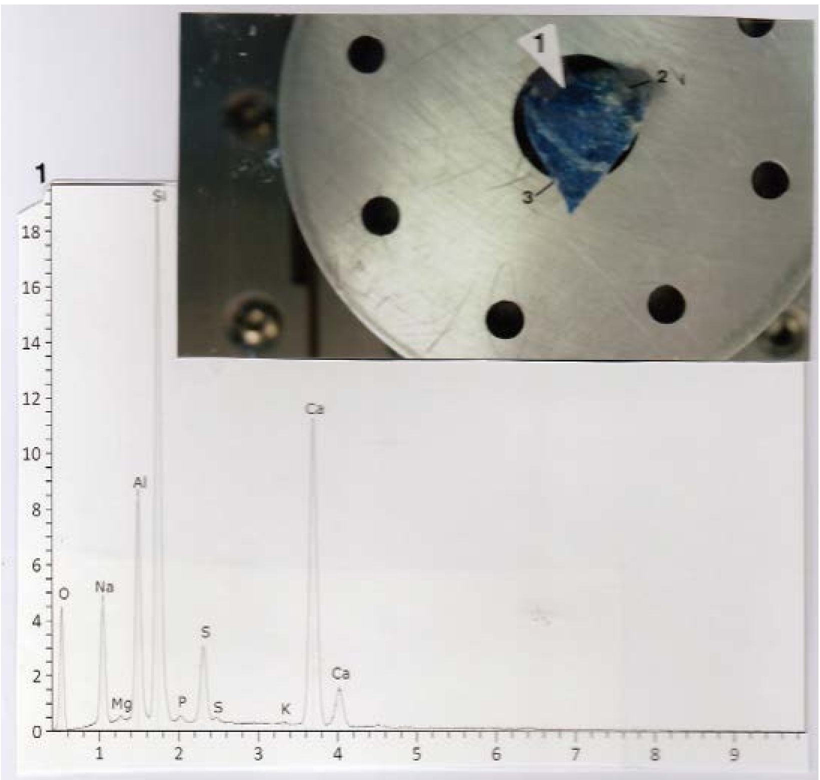

Figure 27. Above: optical photograph (10×) of a lazurite mineral of reference (**1**: the main blue part of the mineral; **2**: a golden point; **3:** a white point). *Below*: the lazurite (part **1**) HR spectrum. O: oxygen; Na: sodium; Mg (traces): magnesium; Al: aluminium; Si: silicium; P: phosphorous; S (two peaks): sulphur; K (traces): potassium; Ca (two peaks): calcium.

We know that the semi-precious stone lapis lazuli was used as glyptic as early as 7000 years ago and for painting starting from the Medieval Age.

Only few sources of lapis lazuli exist in the world, due to the low probability of geological conditions in which it came from. Historical sources of lapis lazuli are in very inaccessible places, such as Afghan and Pamir mountains (Casanova, 2013), and these stones were transported through thousand of kilometres in various trade routes.

Micro-PIXE characterisation of lapis lazuli for a provenance study was realized (Re et al., 2011). The lapis lazuli pigment is common long the Silk Road in wall in wall paint and blue ink for decorative writing (Nöller et al., 2019).

Among particles of the triangle, some lapis lazuli particles are associated with those of azurite (**Figure 8**), which is another blue colouring containing copper; this indicates that, in the Turin Shroud, the lapis lazuli pigment particles were in some case embedded in another less expensive blue material.

In the same order of ideas, we have signalled that intermediate particles g72' and g78 in the lined up g72, g74, g76 and g77 (**Figure 9**), and that the j23 particle near the j34 and j34' associated particles (**Figure 17**) are organic clear blue colourings containing also copper.

5. Conclusion

It is the first time to our knowledge that lapis lazuli minerals are found on the Turin Shroud. Pr Fanti (Fanti & Malfi, 2015) indicated that he found particles of lapis lazuli in the vacuumed dusts of the Shroud, and suspected it as external contaminations that had occurred in the course of centuries.

The seventy lapis lazuli detected on the triangle surface were characterized here for forms and sizes, for colours, and for chemical compositions. They are little particles, of blue colour, which compositions are characteristic of lapis lazuli (with silicate, calcium and pyrite components). Their sizes vary between 0.5 and 15 µm of maximal length, indicating that they are fine particles of a powder. They are present in most areas of the triangle, with a density grossly related to those of other deposited particles in general. The frequently close association observed in numerous of these particles suggests that they are residues of continuous layers of painting.

Why the Turin Shroud was so coloured in blue? The blue of the lapis lazuli (lapis: stone; lazuli: blue) evoke the blue of the sky. Informative for this subject is that the term used for "blue" was the same that for "lapis lazuli" in ancient Egyptian and Akkadian languages (Warburton, 2004). Reasons for the infatuation for the lapis lazuli mineral are due to its profound blue colour and to inclusions in its matter of little gilded fragments that can be assimilated to the starry sky at night.

Acknowledgements

We thank T. Derouin (Natural History Museum of Paris) for his assistance in optical microscopy, and Joelle Salmon for her gift of the lapis lazuli stone of the ring used as reference. The lazurite mineral of reference was purchased from the Carion SA (Paris).

Conflicts of Interest

The authors declare no conflicts of interest regarding the publication of this paper.

References

Casanova, M. (2013). *Le lapis lazuli dans l'Orient ancien.* Editions du Comité des travaux historiques et scientifiques.

Fanti, G., & Malfi, P. (2015). *The Shroud of Turin.* Jenny Stanford Publishing. https://doi.org/10.1201/b18627

Herrmann, G. (1968). Lapis Lazuli: The Early Phases of Its Trade. *IRAQ, 30,* 21-57. https://doi.org/10.2307/4199836

Lucotte, G. (2012). Optical and Chemical Characteristics of the Mineral Particles Found on the Face of the Turin Shroud. *Scientific Research and Essays, 29,* 2545-2553.

Lucotte, G. (2015a). Exploration of the Face of the Turin Shroud. Linen Fibers Studied by SEM Analysis. *International Journal of Latest Research in Science and Technology, 4,* 78-83.

Lucotte, G. (2015b). Exploration of the Face of the Turin Shroud. Pollens Studied by SEM Analysis. *Archaeological Discovery, 3,* 158-178. https://doi.org/10.4236/ad.2015.34014

Lucotte, G. (2015c). Red Blood Cells on the Turin Shroud. *Jacobs Journal of Hematology, 2,* 1-24.

Lucotte, G. (2017). *The Triangle Project* (pp. 5-14). Newsletter 85 of the British Society for the Turin Shroud.

Lucotte, G., Derouin, T., & Thomasset, T. (2016). Hematite, Biotite and Cinnabar on the Face of the Turin Shroud: Microscopy and SEM-EDX Analysis. *Open Journal of Applied Sciences, 6,* 601-605. https://doi.org/10.4236/ojapps.2016.69059

Nöller, R., Feldmann, I., Kasztovsky, Z., Szökefalti-Nagy, Z., & Kovacs, I (2019). Characteristic Features of Lapis Lazuli from Different Provenances, Revised by µXRF, ESEM, PGAA and PIXE. *Journal of Geological Resource and Engineering, 7,* 57-69. https://doi.org/10.17265/2328-2193/2019.02.003

Re, A., Lo Giudice, A., Angelici, D., Calusi, S., Giuntini, L., Massi, M., & Pratesi, G. (2011). Lapis Lazuli Provenance Study by Means of Micro-PIXE. *Nuclear Instruments and Methods in Physics Research Section B: Beam Interactions with Materials and Atoms, 269,* 2373-2377. https://doi.org/10.1016/j.nimb.2011.02.070

Warburton, D. A. (2004). Les échanges dans le domaine de la terminologie des couleurs. *Etudes Corses, 59,* 145-168.

Archaeological Discovery, 2023, 11, 133-152
https://www.scirp.org/journal/ad
ISSN Online: 2331-1967
ISSN Print: 2331-1959

The German *Stutzpunkt* Kerloich (Le Conquet-FR)

Giancarlo T. Tomezzoli

Lettre et Sciences Humaines, Université de la Bretagne de l'Ouest, Brest, France
Email: gt21949@gmx.de

How to cite this paper: Tomezzoli, G. T. (2023). The German Stutzpunkt Kerloich (Le Conquet-FR). *Archaeological Discovery, 11,* 133-152.
https://doi.org/10.4236/ad.2023.112006

Received: February 25, 2023
Accepted: April 4, 2023
Published: April 7, 2023

Abstract

The German *Stutzpunkt* (*Stp*) Kerloich on the Pointe des Renards near Le Conquet (Brittany-France) is one of the most mysterious sites of the Atlantic Wall ever explored before. Many of its components, indicated in literature, disappeared although no evidence of demolitions or destructions during or after the WWII is apparent. Some components, unknown in literature, have been discovered by analysing after WWII French aerial reconnaissance images. Different sources contradict each other about the radar systems on the Pointe during the WWII. The present article summarizes the knowledge and the lack of knowledge concerning the *Stp* Kerloich waiting for further evidences permitting to solve all the open issues.

Keywords

Conflict Archaeology, WWII, Atlantic Wall, Le Conquet, Pointe des Renards, Kerloich, German Radars

1. Introduction

In a past publication (Tomezzoli, 2020) concerning the German defences of the Kermorvan peninsula near Le Conquet (Brittany-France), it was observed that "Surprisingly, no radar was installed at *Stp* Kermorvan". It appeared therefore strange that, during the WWII, this Atlantic Wall sector, so close to the military submarine base of Brest, was not provided with radar surveillance. Therefore, I decided to investigate about the possible presence of radars near the Kermorvan peninsula and the nearby city of Le Conquet.

2. History

The Pointe des Renards, near Le Conquet, derived its name from the abundance of foxes that inhabited the land up to very recent days. But this name was not from origin. According to ancient maps, it was named "Mulets" Pointe. Its rocks, entering the ocean, were not always visible at high tides causing many shipwrecks, one of the last on 1974 was the loss of the longline fishing vessel Dahut from Douarnené (Clochon, 1994).

No relevant constructions were on the Pointe before the half of 18th century. Only at its extremity was the coastal battery of Joul al Louarn created or restored by Vauban on 1688. On 1757-58 the French coastal defence of Brittany was reorganised and a new battery was edified on the Pointe comprising four 18 lbs guns, a powder magazine and a soldier lodgement. Due to bad maintenance and the sea salty air, an inspection on 1777 reported two gun as inoperative. Military inspectors on 1791 reported that only one gun was able to fire, the storage preserved 50 ball projectiles and two barrels of explosive and the soldier lodgement was in good state. An inspection of 1793 reported that the Renards battery was serviced by a guardian and 14 gunners elevated later to 16 which serviced the battery in groups of four. During the Brest blockade by British vessels (1793-1815), Le Conquet port hosted gunners, coastal guards and rapid shallops with two or three masts. A great mast on a circular platform, serviced by a signal guardian, transmitted orders by flags to the shallops and convoys attempting to supply Brest.

On 1860 the French Domain Administration declassed and sold the coastal batteries.

On 1861 the decision was taken to establish a line of electro-semaphoric posts for replacing the obsolete Chappe signal system. Forty-four new semaphoric posts were edified, among them one respectively at Créach'meur, Pointe Saint-Mathieu, Pointe des Renards and Pointe de Corsen. Opened on 1862 the Pointe post was closed on 1881 but it was maintained in good state in view of a possible re-opening. On 1899, the Pointe post was sold to Mr Ferron for 5000F, who transformed it in residence which he inhabited from 1901.

The German *Wehrmacht* arrived at Le Conquet on 19th June 1940. The Pointe houses and the manor of Cruguel were immediately requisitioned. All the reference points identifiable by the allied planes were demolished and *Flak* posts, radars, gonios, projectors, guns and bunkers were installed (**Figure 1**). The Roeland's house on the Pointe was demolished for letting place to a two guns bunker (Clochon, 1994).

There was a *Kriegsmarine* radar station and without doubt one *Luftwaffe* radar station coded *Re* 503. The 25th *Luftwaffe* Signal Company (Unit L42 432) was responsible of the sector from Guipavas to Bénodet. Its IIIrd section was at Le Conquet with 76 soldiers, without doubt in connection with the radars of the sector (Floch, 2012).

The *Stp* Kerlohic was subdivided in resistance nests: *Wn Re* 56 (Le Conquet port), *Re* 57 and *Re* 58 (respectively on the north et south of the Pointe), *Re* 81 to *Re* 83 (Le Conquet city) and *Re* 120 to *Re* 123 (behind the Pointe du Renard) and comprised: 1/V256 (*Unterstand für Maschinensatz für Scheinwerfer G* 200), 1/505, 2/601, 1/622, 1/628, 1/634, 1/646, 1/SK, 1/shelter for *Goliath* (Lecuiller, 2003). *Re* 57 comprised: *Sk Doppelschartenstand* 5 cm *KwK*, Fa storage, Foundation; *Re* 120 comprised: 1 × 628, Antitank wall; *Re* 121 comprised: *V* 256, *Sockel Fu.M.O.* 51 radar "*Mammut Gustav*" (*Re* 503); *Re* 122 comprised: 2 × 601 (1 covered), 1 × 622 (covered), 1 × 646 (behind private house); *Re* 123 comprised: 1 × 634; and globally the *Stp* Kerloich comprised: 2 × 601 anti-tank gun bunker with roof canopy, 1 × 622 Twin group bunker, 1 × 628 group bunker with forward apron, 1 × 634 bunker with six embrasure turret, 1 × 646 water supply bunker 1700 litres, 1 × *Sk Doppelschartenstand* 5cm *KwK*, 1 × V256 energy bunker for radar, 1 × *Socle* for *FuMo radar*, 1 × Fa storage, 1 × Antitank wall, 1 × foundation for a tower (Bunkerpictures.nl, 2012).

On 17th June 1944 at 6 pm, allied aircrafts in swooping attacked the Pointe delivering many bombs. In the evening the Pointe was again attacked (Clochon, 1994). However, up to 10:55 hours of 3rd September 44, a large concentration of craters was directly east of the battery. No bits on the emplacements which appeared unoccupied. The road serving the site was cut by 1 bomb and several near misses. Possible crew quarter gutted. Number of near misses within 50 yards of each primary weapon: No. 1-6, No. 2-6, No. 3-7, No. 4-6 (NARA, 1944).

At the end of August, the American *Task Force S* arrived at 15 km from Le Conquet. On 8th - 9th September began the general offensive against Le Conquet. On 9th September 1944, at noon the 2nd and 5th *Rangers* of the 29th Infantry Division entered Le Conquet. In the mid-afternoon their tanks cannoned the Pointe which reposted with its guns and mortars. On 6 pm the Pointe garrison stopped the fire and capitulated (Clochon, 1994).

On 10th September in the afternoon from the hotel Sainte Barbe the Germans command, by telephone, submitted its request of rendition. The capitulation of Le Conquet took place after the rendition of the defenders of the nearby Kermorvan peninsula (Tomezzoli, 2020). More than thousand German soldiers fall prisoners in the sector Plougonvelin, Trezir, Le Conquet (Rapport Pinczon du Sel, 1947-1948).

On 1947/48 the French Telegraphs Administration established at the Pointe a radio-telephonic station for communicating with ships at the sea. Two operators, from a shelter of an ancient English ambulance, serviced it from 1948. Two houses were built after for ameliorating the comfort of the operators. On 1950 it was established the Radio-Maritime Centre of the French PTT, known by the sailors as Radio Conquet, which grouped radio-telephony and radio-telegraphy. The station closed between 1997 and 2000 (Clochon, 1994).

3. The Visits and the Discoveries

The visits took place on 9th July 2022, 23rd July 2022, and 7th September 2022. The *Stp* Kerloich identified components were the following (**Figures 2-9**). The positions of the disappeared components were tentatively deducted on the basis of their positions on **Figure 1** map.

A minefield (2) (48˚21'23.32"N; 4˚46'38.05"W, height 15.98 m) and a minefield

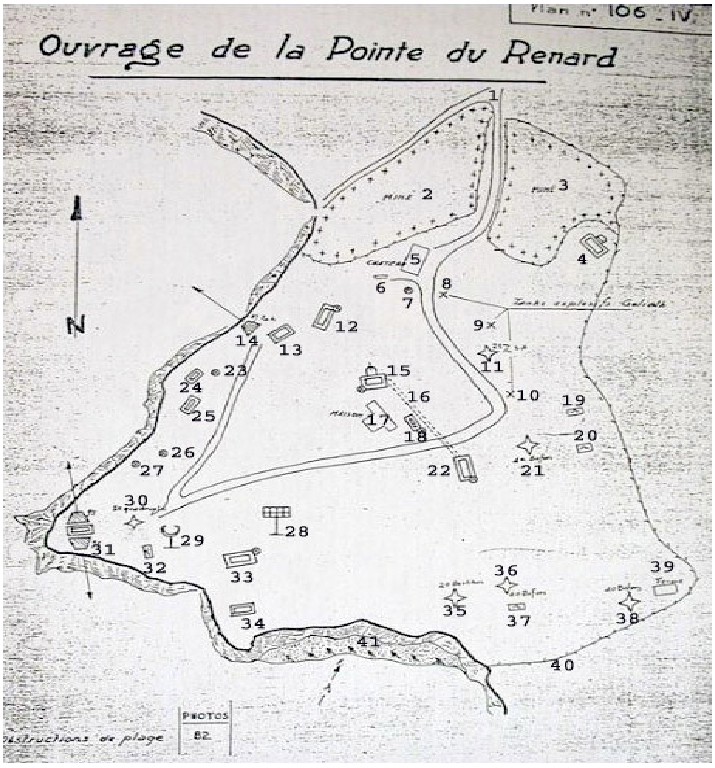

Figure 1. *Stp* Kerlohic (Re 57-58 ; Re120-123), Pointe du Renard (Le Conquet)-map from: Plan n˚ 106_IV (Rapport Pinczon du Sel, 1947-1948): (1) access road; (2) - (3) minefield; (4) unburied concrete bunker surmounted by an armoured cupola for machine gun and grenade launcher; (5) castle-headquarter residence; (6) castle dependence; (7) tobruck for machine gun; (8) - (10) explosive tank Goliath garages; (11) concrete platform for *Flak* gun-small model-25 mm S-A; (12) unburied thick concrete bunker flanked by a tobruck for machine gun; (13) unburied concrete bunker or hold; (14) concrete bunker for anti-tank gun-37 *PaK*; (15) unburied thick concrete bunker flanked by a tobruck for machine gun surmounted by an armored cupola for periscope; (16) concrete tunnel; (17) house-soldier lodgement; (18) unburied concrete bunker or hold; (19)-(20) lightweight concrete bunker or hold; (21) concrete platform for *Flak* gun-small model-40 Bofors; (22) unburied thick concrete bunker flanked by a tobruck for machine gun; (23) tobruck for machine gun; (24) - (25) unburied concrete bunker or hold; (26) - (27) tobruck for machine gun; (28) large format marine search radar; (29) anti-aircraft search radar; (30) concrete platform for *Flak* gun-small model-20 quadruple; (31) double concrete bunker for anti-tank gun; (32) lightweight concrete bunker or hold; (33) buried thick concrete bunker flanked by a tobruck for machine gun; (34) unburied concrete bunker or hold; (35) concrete platform for *Flak* gun-small model-20 Oerlikon; (36) concrete platform for *Flak* gun-small model-40 Bofors; (37) lightweight concrete bunker or hold; (38) concrete platform for D.C.A gun-small model-40 Bofors; (39) farm; (40) barbed wire; (41) tetrahedral pyramids and wooden piles-beach obstacles.

(3) (48˚21'24.25"N; 4˚46'34.15"W, h 20.79 m) de-mined at the end of the WWII. Nothing remained visible.

An unburied concrete bunker surmounted by an armoured cupola for machine gun and grenade launcher (4) (48˚21'23.75"N; 4˚46'31.66"W, h 27.91 m) disappeared.

A castle, headquarter residence (5) (48˚21'22.02"N; 4˚46'36.84"W, h 28.86 m)

Figure 2. *R* 628 (12): (a) Entrance; (b) Crew room with supports for reclinable cots, rusted ceiling and aeration conduits; (c) Support for telephonic connections; (d) Exit stair.

and a castle dependence (6) (48˚21'21.78"N; 4˚ 46'37.97"W, h 27.18 m) in a good preservation state and still inhabited. On the south side of the castle was a 7 × 5 m, different masonry, two floors leaning construction as a castle extension, probably built during of the WWII.

A tobruck for machine gun (7) (48˚21'21.45"N; 4˚46'36.95"W, h 30.3 m) disappeared.

Explosive tank Goliath garage (8) (48˚21'20.91"N; 4˚46'37.48"W, h 33.37 m) leaning against a bicycle garage. It appeared in good preservation state without damages due to combats or bombardments.

Explosive tank Goliath garage (9) (48˚21'20.18"N; 4˚46'37.46"W, h 20.79 m) disappeared.

Explosive tank Goliath garage (10) (48˚21'19.5"N; 4˚46'37.37"W, h 36.96 m) disappeared.

A concrete platform for *Flak* gun-small model-25 mm S-A (11) (48˚21'19.98"N; 4˚46'38.01"W, h 35.13 m) disappeared.

An unburied thick concrete bunker flanked by a tobruck for machine gun (12)

Figure 3. *R* 634 (15): (a) General view; (b) Six embrasures cupola, external view; (c) Periscope opening; (d) Front side, on the left tobruck entrance; (e) External embrasure with splinters of the close combat room (3); (f) Tobruck opening; (g) Embrasure with splinters of the entrance; (h) Six embrasures cupola, internal view; (i) Support for telephonic connections; (j) Embrasure of the crew room.

R 628 (48˚21'21.54"N; 4˚46'40.33"W, h 21.43 m) covered by vegetation, on a private terrain, (**Appendix**, **Figure A1**). The entrances with descending stairs were accessible allowing the interior inspection. The walls preserved the traces of the formwork boards and the original white painting. The crew room preserved the supports for reclinable cots, a rusted ceiling and aeration conduits. On one side was a rectangular support for telephonic connections with a telephonic cable still in place. Various materials and scraps were stacked on the floor. All the original furniture disappeared. No traces of a thermal insulation system were present.

An unburied concrete bunker or hold (13) (48˚21'21.26"N; 4˚46'41.21"W, h 18.08 m) disappeared.

Figure 4. *V* 256 (33) (a) Mounting opening; (b) Tobruck opening; (c) Exhaust duct; (d) Exhaust duct, openings with protection grids; (e) Personnel labyrinth entrance with rectangular niches and embrasure of the close combat room; (f) Entrance door; (g) Piece of mobile cable.

(a) (b) (c)

Figure 5. *V* 256 (33) (a) Mobile cable; (b) Single internal conductor; (c) Rusted plates.

A concrete bunker for anti-tank gun-37 *PaK* (14) (48˚21'18.08"N; 4˚46'45.75"W, h 12.48 m) buried on the bord of a cliff and inaccessible. The opening of the combat room was visible. Its visible external structure appeared in a good preservation state without damages due to combats or bombardments.

An unburied thick concrete bunker flanked by a tobruck for machine gun surmounted by an armored cupola for periscope—*R* 634 (15) (48˚21'19.35"N; 4˚46'34.9"W, h 41.36 m), covered by vegetation, on a private terrain (**Appendix**, **Figure A2**). The front side was in good preservation state without damages due to combats or bombardments. On the left a tobruck entrance, on the right the external embrasure with splinters of the close combat room (3). The combat room of the tobruck was surprisingly clean. The rusted cupola (11) was in good preservation state notwithstanding at least five impact points. Two of them preserved parts of the original projectiles. The entrance with descending stair was accessible allowing the interior inspection. The walls preserved the traces of the formwork boards and the original white painting. The crew room preserved the supports for reclinable cots and a rusted ceiling. On one side was a rectangular support for telephonic connections. The opening of the emerging exit (4) was clearly visible. Various materials and scraps were stacked on the floor. All the original furniture disappeared. No traces of a thermal insulation system were present. All the cupola metallic internal structure disappeared letting visible that no projectile penetrated inside.

A concrete tunnel (16) (48˚21'18.38"N; 4˚46'35.91"W, h 38.73 m). If joining the *R* 634 (15) with the possible *R* 622 (22) its length would be 120 m.

A house-soldier lodgement (17) (48˚21'19.38" N; 4˚46'35.49" W, h 39.58 m), disappeared. It was probably the stable of the castle enlarged and adapted during the WWII. No trace of foundation or ruins were visible on the terrain.

An unburied concrete bunker or hold (18) (48˚21'19.1"N; 4˚46'35.26"W, h 40.33 m) disappeared.

A lightweight concrete bunker or hold (19) (48˚21'19.75"N; 4˚46'31.73"W, h 38.61 m) *R* 601 disappeared.

A lightweight concrete bunker or hold (20) (48˚21'19.55"N; 4˚46'31.67"W, h 38.53 m) *R* 601 disappeared.

A concrete platform for *Flak* gun-small model-40 Bofors (21) (48˚21'18.43"N;

4°46'36.97"W, h 38.49 m) disappeared.

An unburied thick concrete bunker flanked by a tobruck for machine gun (22) (48°21'15.87"N; 4°46'37.38"W, h 39.84 m) about 12 × 8 m, probably an *R* 622, covered by the terrain. The tobruck on the south side was no longer recognizable.

A tobruck for machine gun (23) (48°21'16.85"N; 4°46'46.35"W, h 27.01 m) disappeared.

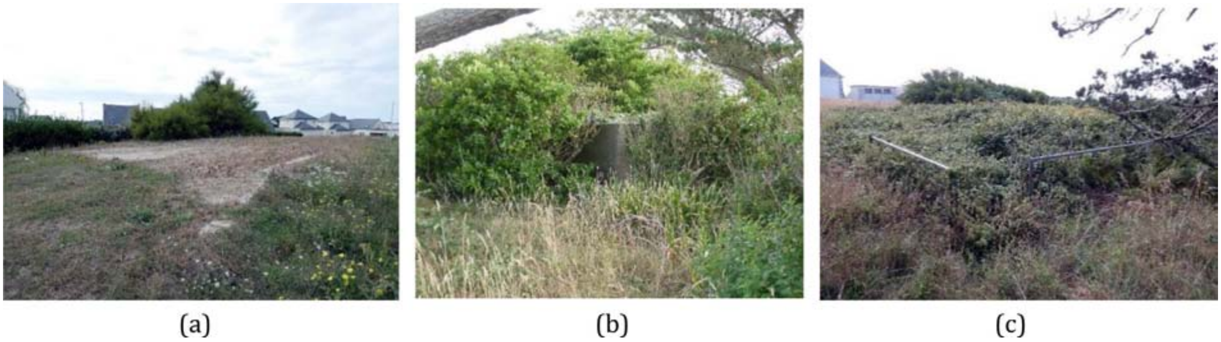

Figure 6. (a) Possible emplacement of the unburied thick concrete bunker flanked by a tobruck for machine gun (22); (b) Concrete support platform of the large format marine search radar (28) covered by vegetation; (c) Ditch covered by vegetation.

Figure 7. Double concrete bunker for anti-tank gun (31) (a) Central portion with entrances closed by bricks; (b) South portion with combat room opening; (c) Combat room interior; (d) North portion with combat room opening.

An unburied concrete bunker or hold (24) (48˚21'15.87"N; 4˚46'49.33"W, h 17.01 m) disappeared.

An unburied concrete bunker or hold (25) (48˚21'15.62"N; 4˚46'49.55"W, h 19.15 m) buried on the bord of a cliff and inaccessible. Only the opening with splinters of the combat room was visible. Its visible external structure appeared in a good preservation state without damages due to combats or bombardments.

A tobruck for machine gun (26) (48˚21'15.47"N; 4˚46'47.7"W, h 31.52 m) disappeared.

A tobruck for machine gun (27) (48˚21'15.13"N; 4˚46'48.16"W, h 30.87 m). Only the circular opening of the combat room, filled with terrain, remained visible.

A large format marine search radar (28) (48˚21'15.47"N; 4˚46'42.12"W, h 39.81 m), probably a *Fu.M.O.* 51 *Mammut Gustav*, disappeared. Only its possible 3 × 3 × 1.5 concrete, support platform covered by vegetation was visible. The platform exposed portions were in good preservation state without damages due to explosions and/or combats. The vegetation covered eight metallic screws, arranged in circle, for fixing the radar support.

An anti-aircraft search radar (29) (48˚21'13.21"N; 4˚46'45.24"W, h 29.47 m), probably a *FuMO* 214 *Würzburg-Riese*, disappeared. Its concrete, support platform, probably a *V* 229, disappeared.

A concrete platform for *Flak* gun-small model-20 quadruple (30) (48˚21'15.1"N; 4˚46'47.34"W, h 31.72 m) disappeared.

A double concrete bunker for anti-tank gun (31) (48˚21'14.4"N; 4˚46'50.15"W, h 27.94 m) on the site of the Joul al Louarn battery, formed by a central portion east oriented, a north portion oriented toward the Kermorvan peninsula and a south portion oriented toward the Pointe Saint-Mathieu. It was covered by terrain and vegetation. The front side of the central portion was partially covered by vegetation, but appeared in good preservation state without damages due to combats or bombardments. It preserved two entrances, one circular hole and traces of the formwork boards with visible pebbles of the Ero Vili (Tomezzoli & Marzin, 2015). The two entrances were closed by bricks; therefore, the interior inspection was not possible. The front side of the south portion was partially covered by vegetation and presented a combat room opening partially obstructed by bricks allowing the inspection of the combat room interior. It appeared severely damaged probably by explosions. A concrete portion with its original metallic armure and various debris were on the floor, the walls and the ceiling appeared scraped off letting visible the metallic armure. Two vertical fissures on the façade and coverage were probably due to said explosions. The front side of the north portion was on the bord of the cliff, the opening of the combat room was not accessible, therefore the inspection of the combat room was not possible.

A lightweight concrete bunker or hold (32) (48˚21'12.61"N; 4˚46'45.69"W, h 28.28 m) disappeared.

A buried thick concrete bunker flanked by a tobruck for machine gun-*V* 256

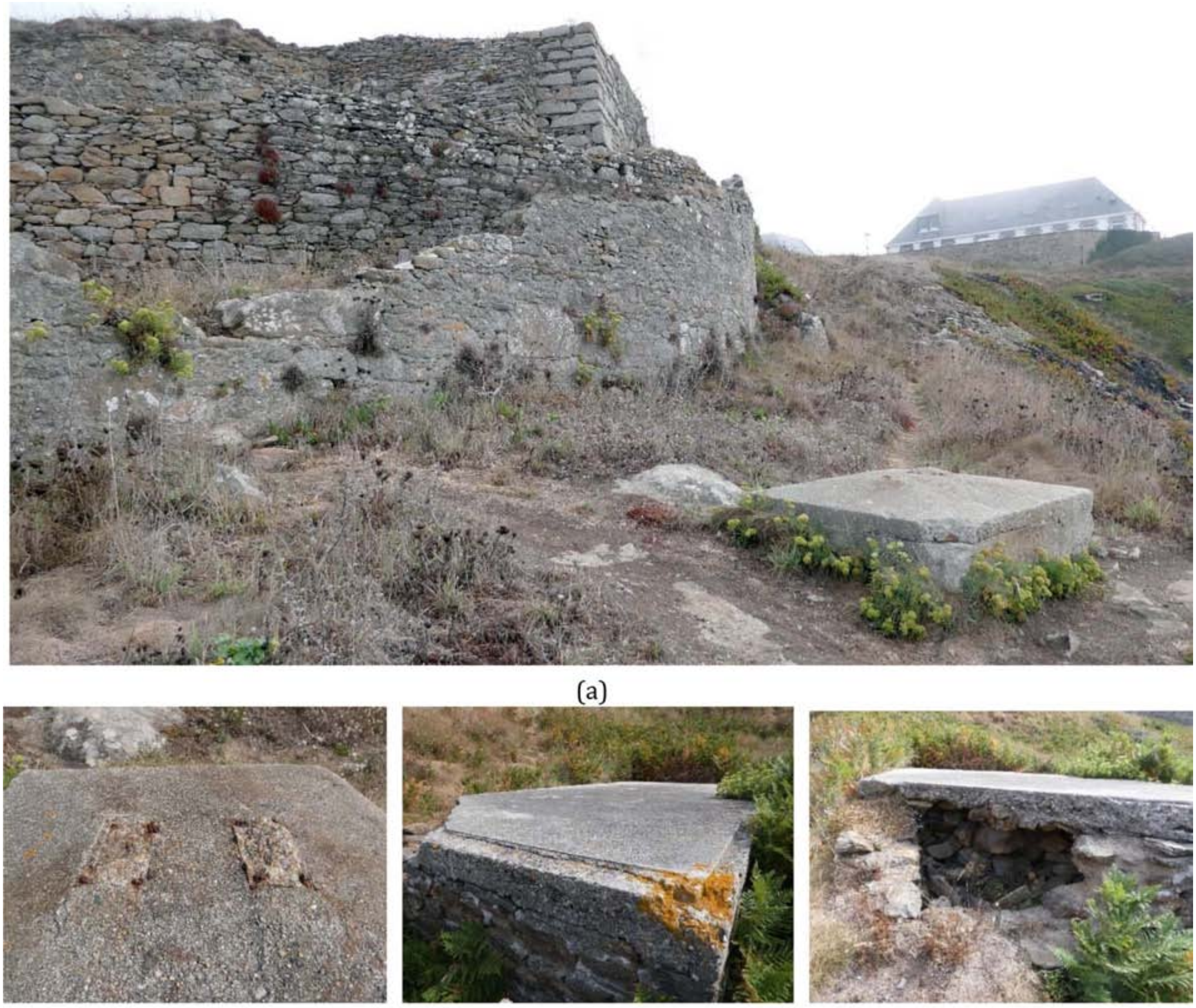

(a)

(b) (c) (d)

Figure 8. Remains of the first Radio Conquet station: (a) Antenna support, on the background ruins of the Joul al Louarn coastal battery; (b) Antenna support, details; (c) Technical shop platform, general view; (d) Platform, internal details.

(33) (48˚21'15.04"N; 4˚46'43.58"W, h 43.58 m) (**Appendix**, **Figure A3**), similar to that discovered at *Stp Re* 311-*FuMB* 445 *Donau* (Tomezzoli, 2018). It had the coverage and the façade partially covered by vegetation. The well-preserved external concrete structure, without damages due to combats, presented traces of the formwork boards with visible pebbles of the Ero Vili. On the coverage, the circular aperture of the tobruck was obstructed by terrain and vegetation; the protruding exhaust duct, partially covered by vegetation, was in good preservation state without damages due to combats. Two of its three openings protection grids disappeared. The emergency exit, on a side of the exhaust duct, was obstructed by terrain. The mounting opening, on the *V* 256 north side, at the end of a concrete inclined access ramp protected by inclined stone walls, was closed by a white garage door. Therefore, the inspection of the engine room, crew lodgement room and fuel room were not possible and their preservation state remained unknown. The personnel labyrinth entrance, near the mounting open-

ing, preserved the original walls white painting faded by the time, two rectangular niches and the embrasure of the close combat room, and led to a closed metallic door. A piece of mobile cable was found near the V 256, in all similar to that discovered near the *V* 256 bunker at *Stp Re* 311-*FuMB* 445 *Donau* (Tomezzoli, 2018).

An unburied concrete bunker or hold (34) (48˚21'7.01"N; 4˚46'39.15"W, h 29.04 m) disappeared.

A concrete platform for *Flak* gun-small model-20 Oerlikon (35) (48˚20'55.26"N; 4˚46'11.2"W, h 22.36 m) disappeared.

A concrete platform for *Flak* gun-small model-40 Bofors (36) (48˚20'56.8"N; 4˚46'8.21"W, h 31.97 m) disappeared.

A lightweight concrete bunker or hold (37) (48˚20'54.94"N; 4˚46' 6.18"W, h 23.84 m) disappeared.

A concrete platform for D.C.A gun-small model-40 Bofors (38) (48˚20'54.08"N; 4˚46'0.92"W, h 20.39 m) disappeared.

A farm (39) (48˚20'54.62"N; 4˚46'11.73"W, h 33.99 m) disappeared.

Barbed wire (40) disappeared. Probably removed after the WWII.

Tetrahedral pyramids and wooden piles-beach obstacles (41) (48˚20'57.81"N; 4˚46'26.18"W, h 0.52 m) disappeared. Probably removed after the WWII.

A 15 × 10 m ditch (48˚21'14.95"N; 4˚46'41.57"W, h 36.83 m) delimited by a railing. A railing interruption on the west side indicated a possible stair for accessing its floor. Completely covered by vegetation, it was not possible to ascertain its preservation state.

The first Radio Conquet station ruins comprising an antenna support (48˚21'13.46"N; 4˚46'51.21"W, h 18.17 m) with two remains of a mast, a station house (48˚21'14.35"N; 4˚46'48.24"W, h 25.91 m) disappeared, a 3 × 5 m technical shop platform (48˚21'14.42"N; 4˚46'48.63"W, h 25.5 m). A corner of the platform was ruined allowing the view of a disorderly stone mass forming its interior.

A 10 × 2 × 2 m antitank wall (48˚21'24.47"N; 4˚46'41.18"W, h 8.76 m) with a rounded top surface barring part of the access to a beach. The formwork, typical of the German masonry and the pebbles of the Ero Vili were clearly visible.

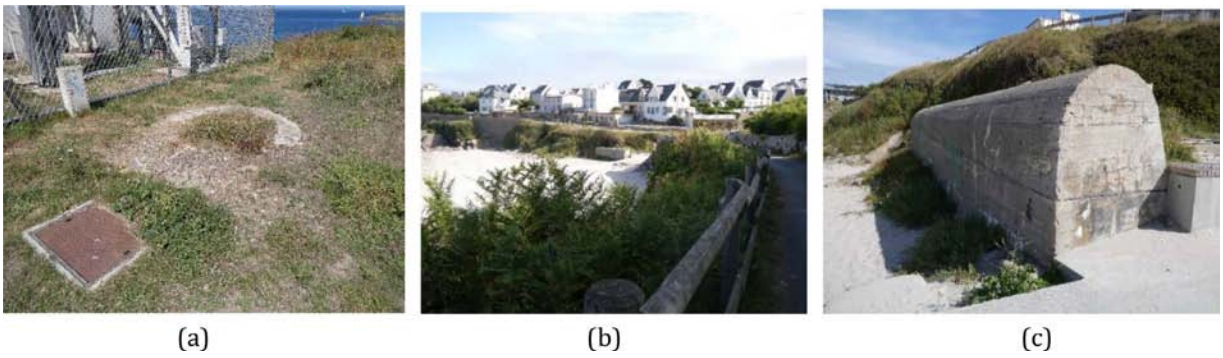

Figure 9. (a) Tobruck (27), opening of the combat room filled with terrain; (b) Antitank wall, general view; (c) Antitank wall, details.

Other components of *Stp* Kerloich were discovered by means of French air reconnaissance images (**Figure 10**); the positions of the components have been tentatively deducted on the basis of **Figure 1** map.

A bunker covered by vegetation (a) (48˚21'16.45"N; 4˚46'31.3"W, h 35.33 m) with two entrances, disappeared.

A bunker (b) (48˚21'16.63"N; 4˚46'38.86"W, h 38.71 m) about 12 × 8 m with tobruck, probably nowadays covered by terrain and vegetation, on the private terrain. Probably a soldier group lodgement.

A bunker (c) (48˚21'18,1"N; 4˚46'39.45"W, h 38.4 m) about 12 × 8 with tobruck flanked on the north-west side by a rectangular bunker with tobruck, probably nowadays covered by terrain and vegetation on the private terrain.

A possible base of a tower (d) (48˚21'17.2"N; 4˚46'33.54"W, h 37.56 m) disappeared.

Unknown structures (e) (48˚21'18.95"N; 4˚46'32.26"W, h 38.17 m) connected by paths, disappeared.

Unknown structure (f) (48˚21'18.53"N; 4˚46'36.38"W, h 38.59 m), probably a square bunker, nowadays covered by terrain and vegetation, on the private terrain.

Unknown structures (g) (48˚21'15.5"N; 4˚46'33.69"W, h 36.69 m), probably a bunker connected by a path to a ditch, nowadays covered by terrain and vegetation, on the private terrain disappeared.

Unknown structure (h) (48˚21'15.69"N; 4˚46'33.2"W, h 37.37 m) probably a bunker nowadays covered by terrain and vegetation.

Figure 10. (a) Possible buried bunker; (b) Possible buried bunker; (c) Possible buried bunker; (d) Foundation for a tower?; (e) Unknown structures; (f) Unknown structure; (g) Unknown structures; (h) Unknown structure; (15) *R* 634; (22) Unburied thick concrete bunker flanked by a tobruck for machine gun.

4. Discussion

The number of disappeared components: 4, 7, 9 - 11, 13, 17 - 21, 23 - 24, 26, 28 - 30, 32, 34 - 39 is considerable. Various hypotheses can be made for explaining their disappearance: (a) these components were covered with terrain after the WWII, (b) they have been demolished during the works of construction of the after-war Radio Conquet components, (c) they have been demolished and the fragments used for constructing barriers against the coastal sea erosion, (d) they have been integrated in components constructed after theWWII, (e) they have never been built. One hypothesis does not exclude the others. Concerning (a), no surface modifications indicating covered bunkers has been remarked during the visits. Concerning (b) and (c), the demolition would have had very high costs not reasonably sustainable by the municipality of Le Conquet and the Brittany region. Concerning (d) no house appears to have been constructed over or integrating all or parts of said components. Concerning (e), it is not possible to assume that the Rapport Pinczon de Sel was inaccurate in indicating the components forming the *Stp* Kerloich (**Figure 1**). In fact, it was prepared by a serious military commission immediately after the WWII and, used in many previous publications, it has always provided correct indications about the components of the German bases visited. Mr Clochon, historian of Le Conquet, confirmed that no massive bunker destruction was made after the WWII and he is in favour of the hypotheses (a) and (d).

The ditch is not visible on post WWII French air reconnaissance images. Therefore, it is not possible to assume that it could have had the functions of either hosting and protecting one or more shacks for personnel lodgement as those at Cap Fréhel (Tomezzoli & Moser, 2021), *Qu* 500 and *Qu* 13 at the Pointe du Raz (Tomezzoli, 2021), on the Menez Hom (Tomezzoli, 2017a) and at Flescou (Tomezzoli, 2022) or be a pool as those at Murs Érigné (Tomezzoli, 2016) and at the Domaine de Pignerolle (Tomezzoli, 2019) for providing relax to the personnel in service and water in case of fire to the devices of the *Stp*. Mr Clochon is of the opinion that it was excavated after the WWII for providing water in case of fire at the buildings of the after WWII Radio Conquet components.

The *V* 256 was a thickness B bunker for protecting a mobile power generator for headlights G 200 K, operated by 1 × officer and 5 × servants lodged inside it. The power transmission to the headlight was assured by a 100 m long flexible cable, a portion of it was discovered on the site. The movable generator was introduced through the ramp and the bunker mounting opening. Ventilation and re-cooling of water was carried out by a screw fan in the generator room. It sucked air out of the room and blowed it over a radiator and out through the exhaust duct. Ventilation for the lodgement room was carried out by an electric or a hand drive fan with gas insolation. The generator room was not gas-proof; but the lodgement room was fitted with a gas barrier door (Fleuridas, 2022).

The mobile cable discovered near the *V* 256 was in all similar to that found at *Stp Re* 311-*FuMB* 445 *Donau* (Tomezzoli, 2018). In both sites, because no searchlight G 200 K was present, the two *V* 256, through said cables, powered the respective *Stps* radars. The cable presented a spiral metal external rusted insulation, a first internal rubber insulation, a second metallic internal insulation, a final very thin internal cylindrical insulation containing a filling material surrounding a single cylindrical conductor. Two rusted plates of unknown purpose were also discovered near *V* 256.

The radar deployed at the Pointe or in the nearby land is a rather controverse question.

A first source (Rapport Pinczon de Sel, 1947-1948) indicates: a *Flak* search radar (radar de recherche DCA) and a marine search radar great model (radar de recherche marine grand model).

A second source (Lippmann, 2021) indicates:

- 447, *FUMO,* Pte des Renards, *Seetaktische Funkmeßortung*, 1 × *FuMO* 214 *Würzburg Riese*, 1 × *FuMO* 2 *Calais B*;
- 448, *FUMO*, Keronvel/Le Conquet Südost, *Seetaktische Funkmeßortung*, 1 × *FuMO* 301 oder 303, 1 × *FuMO* 51 *Mammut Gustav*.

A third source (Friese 4, ABSA) partially confirmed these last locations, indicating:

- *SeeTakt*, *FUMO*, Pointe des Renards, 1 *FuMO* 214 *Würzburg Riese*, 1 *FuMO* 2 *"Calais"*;
- *FuMG*, Keronvel (Le Conquet) Sud-ouest (Ploumoguer), 1 × *FuMO* 302, 1 × *Wassermann Typ*?, 1 × *FuMO* 51 *Mammut Gustav*.

However, during the visits at the Pointe no *V* 229, hexagonal support for the *FuMO* 214 *Würzburg Riese*, has been found. Concerning the *Mammut-Gustav* radar, only four were built and the fourth was at the Pointe (S IV). Starting from 1941, the German manufacturer GEMA manufactured some (different?) versions of the *FMG* 41 *G (gA)* = *FuMO* 51 "*Mammut Gustav*" indicated as long-distance search system for land use on the 80 cm wave. It consisted of a 10 m × 20 m antenna which could be rotated mechanically by about ±50˚ around a central mast. Two external rans supporting masts with wheels on concentric rails circular sections. The equipment set (368 MHz, 125 kW) was housed in a barrack behind the central mast [112, 243] (Trenkle, 1979). The 3 × 3 × 1.5 m concrete platform identified during the visits at the Pointe could be said central mast, but no trace of the concentric rails exposed or buried in the terrain were visible. It is also possible that said platform was the support for the *FuMO* 2 *Calais B*.

The visit made at Keronvel, now a district of Le Conquet, on 9th July 2022 revealed no vestiges of radars or supports for radars *Wassermann* and/or *Mammut Gustav*. Moreover, a paysan interrogated on place confirmed that no such kind of radars or radar vestiges existed at Keronvel.

A further source (Chazette, 2014), on the basis of coordinates derived from British archives, mentions a displacement of the *Mammut Gustav* from the Pointe to a more elevated position at *Re* 503.

In both these last two cases, the indications of Keronvel and *Re* 503 would correspond to the German radar base *Re* 503 at the locality Keringar Vihan (Groaz-Ar-Veiller), 500 m east from Keronvel, visited on 12th September 2009 (Tomezzoli, 2017b). However, said visit revealed a first concrete bunker for radar *Freya*, without basement and rails for a *Mammut Gustav* radar and a second brick bunker invaded by the vegetation and inaccessible.

5. Conclusion

The visits on the terrain rather than providing complete certitudes opened various issues concerning the *Stp* Kerloich. The fate of its disappeared components, the radars in service at the Pointe during the WWII, the possible radar displacements, the radars in service at *Re* 503 *during the WWII*, remain to be solved. The hope is that further studies will help to shed light on all these issues.

Acknowledgements

I am grateful to Mr Clochon J.-P. for his explanations concerning the German installations on the Pointe des Renards, to Mr Fleuridas P. for his explanations and his kind permission to insert in the Appendix the plans of the bunkers *V* 256, *R* 628 and *R* 634 and to the proprietor of the private terrain for his kind permission to visit the bunkers *R* 628 and *R* 634.

Conflicts of Interest

The author declares no conflicts of interest regarding the publication of this paper.

References

Bunkerpictures.nl (2012). *Datasheet Le Conquet/Point des Renards*. https://www.bunkerpictures.nl/datasheets/france/finistere/kva%20b/kvgr%20saint-renan/datasheet-le%20conquet-point%20des%20renards.html

Chazette, A. (2014). *Conquet Radar*. https://fortif29.forumactif.org/t405-conquet-radar?highlight=le+conquet

Clochon, J.-P. (1994). *La pointe des renards: Historique*. https://www.aspect-le-conquet.fr/le-conquet-en-savoir-plus/la-pointe-des-renards-historique

Fleuridas, P. (2022). *Regelbau V 256*. Private Archive.

Floch, A. (2012). *L'Occupation Allemande dans les 162 Communes du Nord Finistère (1940-1944)*. Cloitre imprimeurs. Saint Thonan.

Lecuiller, A. (2003). *Ensemble fortifié (Stützpunkt "Kerlohic") (Re 57-58; Re 120-123), Pointe du Renard (Le Conquet)*. Dossier IA29001511. http://patrimoine.bzh/gertrude-diffusion/dossier/ensemble-fortifie-stutzpunkt-kerlohic-re-57-58-re-120-123-pointe-du.renard-le-conquet/67f817a7-4eef-4dc1-8538-1f97b9d3afd8

Lippmann, H. (2021). *Funkmeß(ortungs)stellungen in Frankreich*. Bretagne West mit Brest. Stand 03.03.2021. http://www.atlantikwall.info/radar/france/rf_.htm#Bretagne_West

NARA (National Archive Catalogue) (1944). *III a (1619): Le Conquet, France. From RG: 243*. Damage Assessment Reports. National Archives Identifier: 41003967, Container Identifier: 92, HMS Entry Number(s): Entry 27, I-10. Creator: WWII Department. U.S. Strategic Bombing Survey. European Survey. Intelligence Branch. Target Section. 1944-1945.

Rapport Pinczon du Sel (1947-1948). *Le Mur de l'Atlantique la Cote de la Manche et de l'Atlantique du Mont Saint-Michel à Laita. Service Historique de la Marine. Brest, Livre IV. Plan n° 106_IV, (refs. E 162, 1 U 61)*.

Tomezzoli, G. T. (2016). The German Base "the Bank" at Mûrs-Érigné (Anjou-FR). *Archaeological Discovery, 4,* 37-47. https://doi.org/10.4236/ad.2016.41004

Tomezzoli, G. T. (2017a). The WW II German Stützpunkt on the Menez-Hom (Finistère-FR). *Archaeological Discovery, 5,* 224-237. https://doi.org/10.4236/ad.2017.54013

Tomezzoli, G. T. (2017b). The German Radar Surveillance around the Aber Wrach during the WW II. *Archaeological Discovery, 5,* 22-41. https://doi.org/10.4236/ad.2017.51002

Tomezzoli, G. T. (2018). The WW II German Defences Structures around Ploumoguer (Finistère-FR). *Archaeological Discovery, 6,* 62-87. https://doi.org/10.4236/ad.2018.62005

Tomezzoli, G. T. (2019). The BDU West between WWII and Cold War. *Archaeological Discovery, 7,* 1-19. https://doi.org/10.4236/ad.2019.71001

Tomezzoli, G. T. (2020). The Stp Kermorvan (Le Conquet-FR). *Archaeological Discovery, 8,* 228-244. https://doi.org/10.4236/ad.2020.83013

Tomezzoli, G. T. (2021). The German Radar Stations at the Pointe Du Raz (FR). *Archaeological Discovery, 9,* 198-222. https://doi.org/10.4236/ad.2021.93011

Tomezzoli, G. T. (2022). The Heer Küste Artillerie Abteilung 1161. *Archaeological Discovery, 10,* 193-214. https://doi.org/10.4236/ad.2022.104007

Tomezzoli, G. T., & Moser, J.-L. (2021). The German Radar Station La 318 Frosch. *Archaeological Discovery, 9,* 113-134. https://doi.org/10.4236/ad.2021.92006

Tomezzoli, G., & Marzin, Y. (2015). The Ero Vili and the Atlantic Wall. *Advances in Anthropology, 5,* 183-204. https://doi.org/10.4236/aa.2015.54018

Trenkle, F. (1979). *Die deutschen Funkmeßverfahren bis 1945*. Motorbuch Verlag. Stuttgart.

Appendix

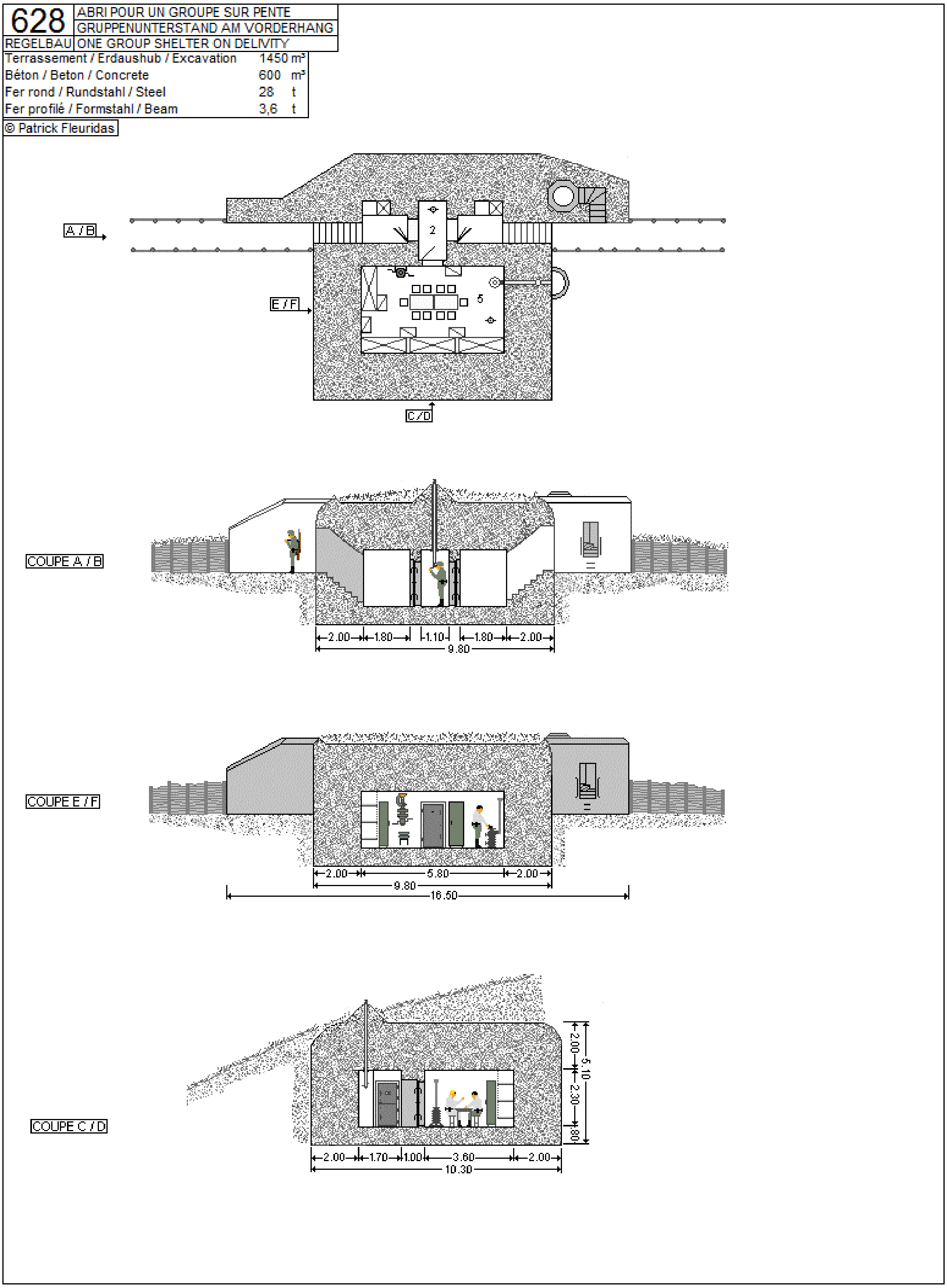

Figure A1. R 628 plan: 2 gaslock; 5 crew room (Courtesy Fleuridas P.).

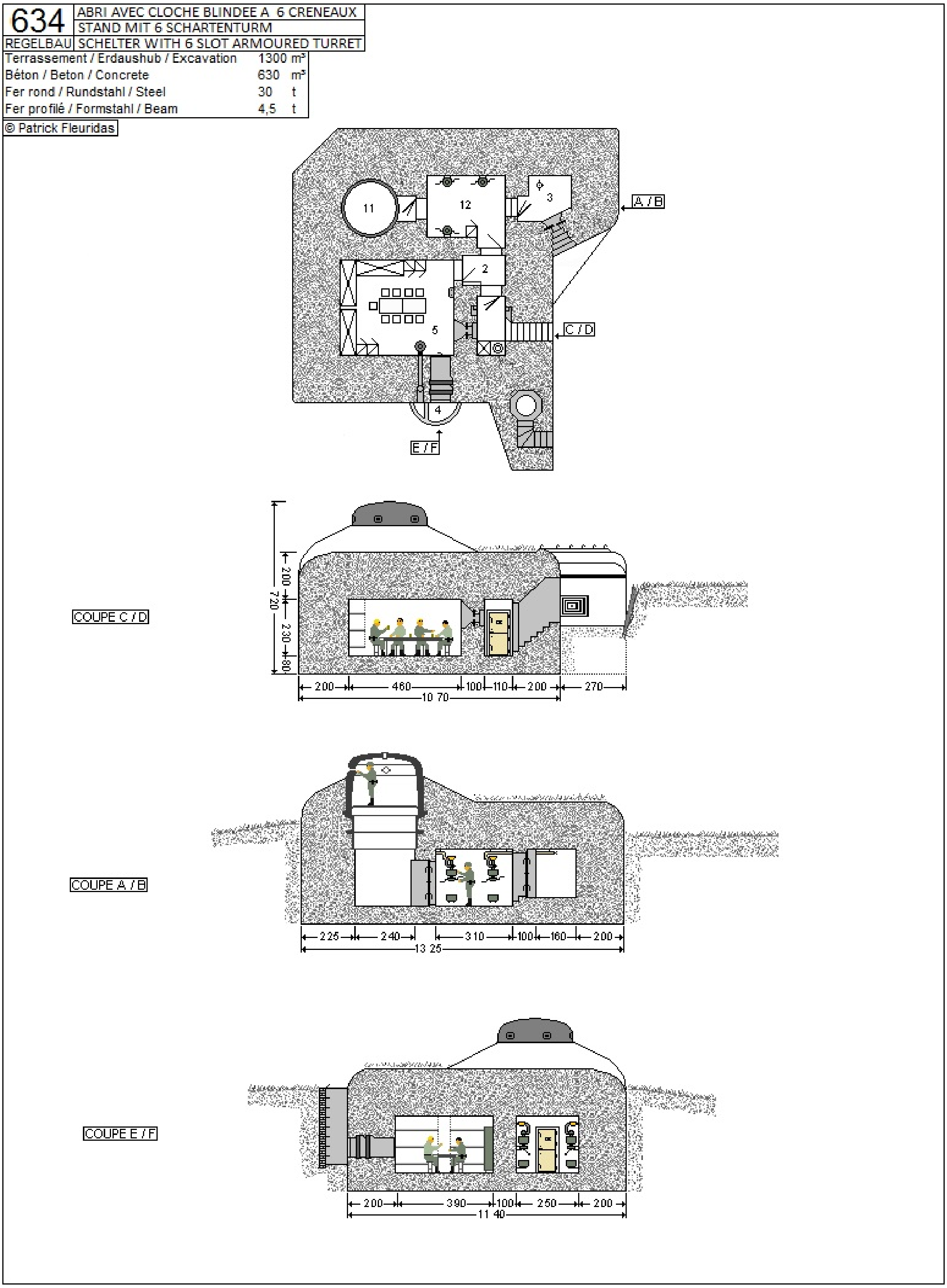

Figure A2. R 634 plan: 2 gaslock; 3 close combat room; 4 emergency exit; 5 crew room; 11 six embrasures turret; 12 ventilation room (Courtesy Fleuridas P.).

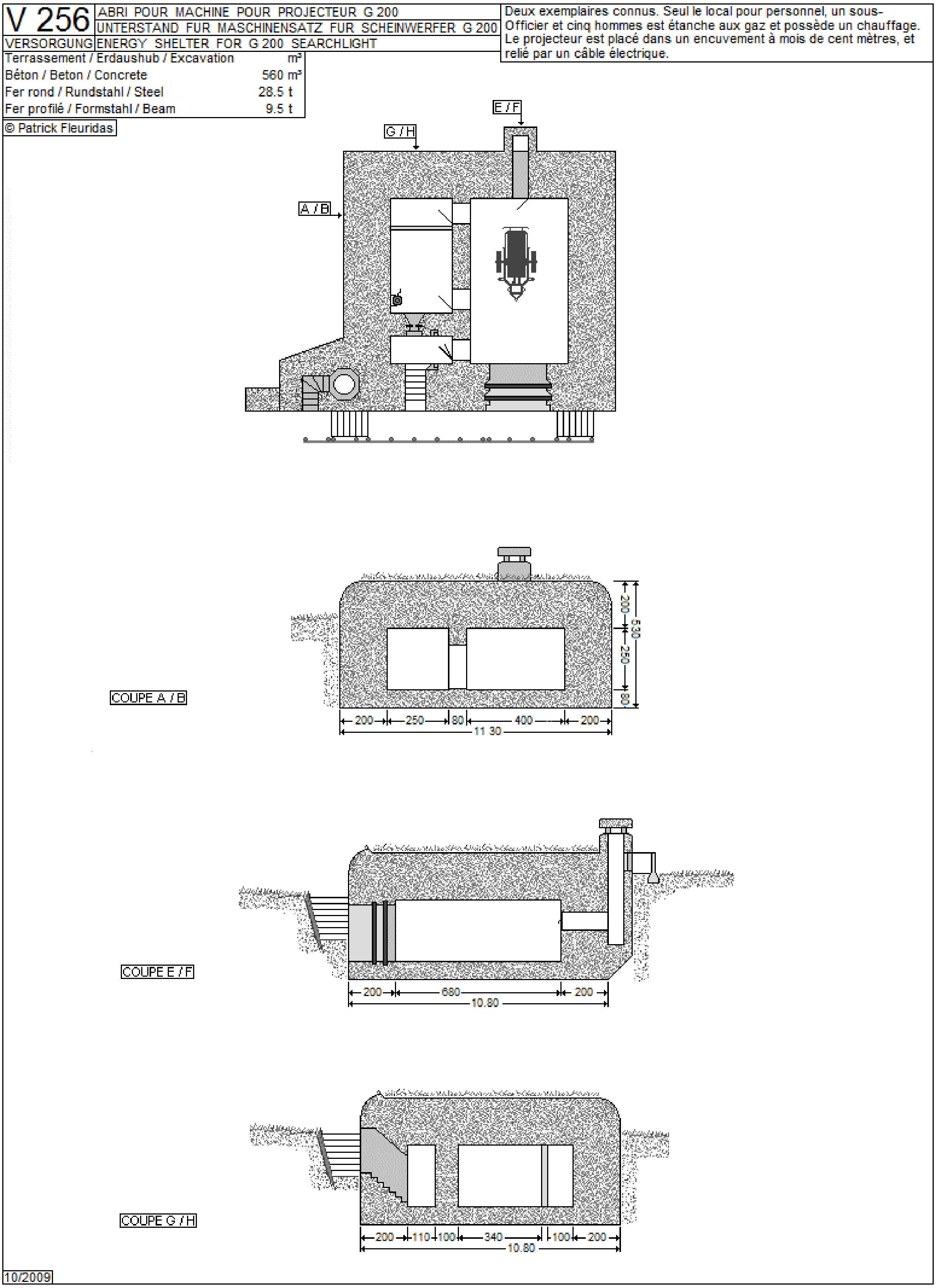

Figure A3. V 256 plan (Courtesy Fleuridas P.).

Archaeological Discovery, 2023, 11, 153-170
https://www.scirp.org/journal/ad
ISSN Online: 2331-1967
ISSN Print: 2331-1959

Roman Empresses' Coins from a Private Collection: A Descriptive Archaeological Study

Musallam R. Al-Rawahneh[1], Vagner Carvalheiro Porto[2]

[1]Department of Archaeology and Tourism, College of Social Sciences, Mutah University, Karak, Jordan
[2]University of São Paulo, São Paulo, Brazil
Email: rwahneh@mutah.edu.jo, vagnerporto@usp.br

How to cite this paper: Al-Rawahneh, M. R., & Porto, V. C. (2023). Roman Empresses' Coins from a Private Collection: A Descriptive Archaeological Study. *Archaeological Discovery, 11,* 153-170.
https://doi.org/10.4236/ad.2023.112007

Received: January 10, 2020
Accepted: February 15, 2020
Published: April 12, 2023

Abstract

This is the first study of a unique private collection of coins belonging to Roman empresses. The collection includes silver and bronze/copper coins bearing inscriptions, pictures, symbols, and monograms. These coins have significant artistic implications as they represent unique Roman styles and types, and some of them are rare. The time frame of the existence and usage of the study sample extends from the beginning of the first century A.D. to the beginning of the fourth century A.D., concurrent with the emergence of the Roman Empire and the height of its expansion and prosperity. The study also seeks to discuss the reasons these coins depicting the empresses were produced; for example, the marriage of Marcus Aurelius with the emperor's daughter, Faustina the Younger—the coins attesting the desire for the continuation of the dynasty and celebrating the beginning of a new Saeculum Aureum. The coinage also reflects the joint rule of Marcus Aurelius and Lucius Verus until 169 A.D., when Faustina II and Lucilla were depicted. Homonoia and the victory over Armenia were also depicted, and the decades are celebrated. We also discuss the possible reasons for the deterioration of bronze coinage in the second half of 2nd century A.D. and the reasons that led to a substantial increase in coinage in the name of Augusta at the end of Hadrian's reign.

Keywords

Roman Empire Period, Roman Empresses, Numismatics, Roman Coins

1. Introduction

The coins were chosen to represent the currency of the Roman Empire over a five-hundred-year period when the coinage system underwent significant development and anticipated all coin types that have since been created. At the same time, in terms of artistic merit, it achieved such an excellence that will almost never be surpassed. There is a consensus among scholars that various currency reforms occurred at the same time; we continue to wonder why the Roman state minted coins in the first place. What was the purpose? To answer this question, the coinage was based on various metals, and the supply of these metals was important for minting coins. In essence, according to Howgego, the "supply of money was dictated by the availability of metals that could in principle be used as money, by the extent to which such metals were used as money, and by how hard that money was made to work". Howgego (1992: p. 4).

Many reforms occurred after the shift to the Empire, including the establishment of a new currency. Gold was introduced to suit the demands of the world's metropolises, and two new coins, the Aureus and its half, were made in this metal. They were based on silver coins. The standard silver currency remained the denarius, with distinct types. The emperor's head replaced those of deities, with a superscription that foreshadowed current currency legends. It was made of the emperor's name and titles, frequently with the date of strike placed in a circle around the edge of the coin (Metcalf, 2012: pp. 338-343). Nero (45-68 A.D. was the first emperor to diminish the weight of the denarius, starting a process of degeneration, but Nero was a man of tremendous creative aptitude, despite his weaknesses. His interest in the imperial currency led him to establish an as (*aes*) and quadrants in orichalcum, in addition to the ones struck in copper (Sear, 1988: p. 11; Metcalf, 2012: pp. 346-348).

2. Sabina 83-137 A.D.

Vibia Sabina was the granddaughter of Emperor Trajan and the daughter of L. Vibius, Sabinus, and Matidia; she was Hadrian's wife from 117 to 138 A.D., thanks to Plotina's favor (Seaby, 1979: p. 210; Sear, 1988: p. 13; Gagarin, 2010: p. 60). Sabina's marriage to the 24-year-old Hadrian thus seemed to indicate that the young man had been marked out for the Imperial succession. Their 36-year union was destined to be childless, and there was much gossip surrounding the unhappiness of their relationship, most of it probably groundless. She followed her husband on the majority of his excursions, but their marriage was strained (Sear, 1988: p. 83). Despite her husband's accession to the imperial throne in A.D. 117, Sabina did not receive the title of Augusta (and thus the right to coinage in her name) until A.D. 128. The reason for the long delay is unknown, but it appears to have coincided with Hadrian's postponement of accepting the title Pater Patriae (Father of His Country) (Sear, 2002: p. 191). Although not extensive by later standards, Sabina's coinage was much larger than any previous consort, which would seem to contradict the rumors of their unhappy relationship. Sabina died late in the year 136, thus predeceasing her husband by about a year and a half, and was accorded a special coinage to commemorate her consecration. Hadrian consecrated her and issued a special coinage (Sear, 1988: p. 151; Sear, 2002: p. 192; Gagarin, 2010: p. 63; Metcalf, 2012: p. 569). Also, under Hadrian's reign, coins bearing the image of Sabina were produced in the eastern and western provinces, **Figure 1**.

According to Richard A. Abdy (Abdy, 2014: pp. 73-91), the main series of Sabina coinage throughout her lifetime falls into two main groups of obverse legends. The first is formed when SABINA AVGVSTA IMP HADRIANI AVG P P quickly drops the IMP (which had also been present in the pre-P P group). SABINA AVGVSTA HADRIANI AVG P P is seen with a large amount of coinage, which was most likely created over time; however, it is possible that it remained within sestertii throughout her life. The second legend format is shortened (at first just to gold and silver) to SABINA AVGVSTA. This shortening trend is perfectly in keeping with the simplification of the legends on the coinage in the name of Hadrian himself. This is the case with our coin.

Figure 1. AR Denarius. Rome, 128-136/7 A.D. th. 1.72 mm.; dim.18.58 mm.; 3.25 gr.; dir. 6 h. Obv. SABINA. AVGVSTA. diad. and dr. bust r., hair in a queue down back. Rev. IVNONI. REGINAE. Juno, veiled, stg. hd. l., holding patera and scepter. l. hand. (Under Hadrian) R.I.C 395a; B.M.C. 895; R.I.C 401a; St. 370 and *80. R.S.C II 37. R.C.V 1187.

3. Faustina I Senior 100-141 A.D. (The Elder/Maior)

Annia Galeria Faustina Senior is the illustrious daughter of M. Annius Verus (three times consul) and Rupilia Faustina. She was probably born in the last decade of the first century; she married Antoninus Pius 138-161 A.D. before his accession and bore him two sons and two daughters, one of whom was Faustina II and the mother of Faustina Junior (Seaby, 1979: p. 124; Sear, 1988: p. 161), but only one (the younger Faustina) lived long enough to see her father achieve imperial status after Hadrian's death in A.D 138 (Sear, 2002: p. 278; Varner, 2004: p. 153; Gagarin, 2010: p. 124; Callatay, 2013: p. 310).

Faustina died in A.D. 141 "and was consecrated by Antoninus, who also issued a very extensive commemorative coinage in her honor", **Figure 2**, **Figure 3**. (Sear, 2002: p. 277), only two years after she had received the title of Augusta. Her deification was followed by a commemorative coinage in her honor issued on an unprecedented scale in the full range of denominations. The year 147 marked a major turning point when the elevation of the younger Faustina to the rank of Augusta resulted in the disappearance of this title from the obverses of her mother's posthumous coinage. Her lifetime coinage is thus relatively sparse in comparison to the massive postmortem releases created several times by her bereaved husband during the next two decades (Sear, 2002: p. 278). The extensive later "Diva Faustina" issues may have been concentrated around the 10th and 15th anniversaries of the empress's death in 141 and the dedication of her temple the following year (i.e., AD 151-2 and 156-7) (Sear, 2002: p. 265; Gagarin, 2010: p. 124; Callatay, 2013: p. 311).

Figure 2. AR Denarius. Rome, 147-149 A.D. th. 2.32 mm.; dim. 17.39 mm.; 3.45 gr.; dir. 6 h. Obv. DIVA. FAVSTINA, diad. dr. bust r., hair, looped up Rev. AVG. VSTA, Vesta, veiled, stg. l., hd. l., (rare) holding the long supporting fold of drapery in r. hand. l., hand to the side. (Antoninus Pius) R.I.C 362; B.M.C. 421; R.I.C II, 104; Sear 4584.

Figure 3. AR Denarius. Rome, 147-161 A.D. th. 2.39 mm.; dim. 17.40 mm.; 3.43 gr.; dir. 12 h. Obv. (rare) [DIVA] FAVSTINA, diad. dr. bust r., wearing pearls bound on top of her head. Rev. AETER NITAS Aeternitas stg. l., holding globe and billowing veil in r. hand. (Antoninus Pius), R.I.C II 351; B.M.C.R.E 373; R.S.C 32. Sear, 4578.

4. Faustina II Junior 130-175 A.D. (The Younger/Minor)

"Annia Galeria Faustina" was the daughter of Antoninus Pius and Faustina Senior; she was born about A.D. 127, and was the wife of her maternal cousin, the Roman Emperor Marcus Aurelius. Six years later the couple was married; she subsequently bore many children, one of whom was the future emperor Commodus. In 147, the younger Faustina received the title of Augusta in celebration of the birth of her first child (Seaby, 1979: p. 221; Sear, 1988: p. 170; Gagarin, 2010: pp. 123-124). Faustina's coinage began with her elevation to imperial status in AD 147 and was issued under her father's authority under Emperor Antoninus Pius for the first fourteen years. Thereafter, until she died in AD 175, her coinage was struck under her husband, Emperor Marcus Aurelius. A lengthy posthumous coinage was also produced in 176 (Sear, 2002: p. 281). Unfortunately, to our knowledge, it is not possible to assign precise dates to virtually all individual Roman issues of Faustina within the period AD 161-175 (Sear, 2002: p. 341; Varner, 2004: p. 154; Callatay, 2013: p. 311).

She died late in AD 175 in the remote mountain village of Halala (later Faustinopolis) in Cappadocia. She had been accompanying her husband on his journey to the east in the aftermath of the abortive rebellion of Avidius Cassius, in which she may have been implicated. Despite this, and a reputation for marital infidelity, her memory was revered by the compassionate emperor, who ordered her immediate deification. Although the commemorative coinage issued in her memory was not produced on the same vast scale as that of her mother three decades before, it is nonetheless surprisingly extensive and includes an interesting array of unusual types and legends, **Figure 4**, **Figure 5** (Seaby, 1979: p. 221; Sear, 1988: p. 170; Sear, 2002: p. 337; Gagarin, 2010: p. 124; Callatay, 2013: p. 312).

Figure 4. AR Denarius. Rome, 161-175 A.D. th. 2.15 mm.; dim. 18.55 mm.; 3.42 gr.; dir. 7 h. Obv. FAVSTINA. AVGVSTA, diad. dr. bust r., with a double circlet of pearls around the head, hair looped up or in a knot neck. Rev. FECVN. DITAS, Fecunditas stg. hd. r., holding a scepter and a small child. (Aurelius), B.M.C. 91; R.I.C. 677; R. S.C II 99. Sear 5252.

Figure 5. AR Denarius. Rome, 161-175 A.D. th. 2.55 mm.; dim. 17.65 mm.; 3.47 gr.; dir. 12 h. Obv. FAVSTINA AVG VSTA, diad. dr. bust r., with a double circlet of pearls around the head, hair looped up or in a knot neck Rev. FECVNDI AVG VSVSTAE, Fecunditas stg. hd. l., holding two infants/children in her arms, between two young girls. (Paris unusual style) (Aurelius) B.M.C. 398; R.I.C. 676; R.S.C II 95; Sear 5251.

5. Crispina 164-187/192 A.D.

Bruttia Crispina, the daughter of L. Fulvius Bruttius Praesens, accompanied Marcus Aurelius on his expedition against the Sarmatians. After this triumph, Commodus was associated with Marcus Aurelius as co-emperor, and he was married to Commodus in A.D. 177, when she received the title "Augusta", Nevertheless, she was banished to Caprese (Capri) and later pit to death during the beginning of her husband reign (Seaby, 1979: p. 255; Sear, 1988: p. 183; Varner, 2004: p. 153; Gagarin, 2010: p. 51). Crispina was converted in Augusta. Her coins were typical for such imperial ladies, depicting all of the classic Roman deities and qualities for which Augusta was ideal; in this example, Venus, the goddess of love and beauty, held an apple in her right hand, **Figure 6** (Brennan, 2004: p. 35).

Figure 6. AR Denarius. Rome, 180-183 A.D. th. 1.95 mm.; dim. 18.85 mm.; 3.51 gr.; dir. 6 h. Obv. CRISPINA. AVGVSTA, diad. dr. bust r., with one circlet of pearls around the head, hair looped up or in a knot neck Rev. V E N V S, Venus stg. front, hd. l., holding an apple in r. hand and drawing up a drapery fold on 1., shoulder. (Commodus) B.M.C. 44; R.I.C III 286a; R.S.C II 35; R.S.C 35.

6. Julia Domna 170-217 A.D.

Julia Domna was a Roman empress of Arab origin, she was born in Emesa (Homs) in the Roman province of Syria about AD 170, she was the younger daughter of the wealthy and influential Julius Bassianus, attracted the attention of the ambitious 42-year-old widower Septimius Severus, after the death of his first wife, married her about A.D. 173 as his second wife. It was not until A.D. 188 that she bore him his first son, named Bassianus, later changed to Antonius and nicknamed Caracalla. A year later, another son, Geta, was born in 189 and was also destined to become emperor (Gagarin, 2010: p. 141). Later in life, she gathered a coterie of men of culture and learning, greatly adding to the brilliance of the Imperial court in Rome. There can be little doubt that she exercised considerable political influence over her husband, between AD 200 and 205. After the downfall of Plautianus Julia resumed her former prominent place in public life. Julia Domna's coinage began with her elevation to imperial status in AD 194 and was issued under her husband's authority, Emperor Septimius Severus, for the first seventeen years. Thereafter, until the temporary downfall of the dynasty in AD 217, it was struck under her sons, the emperors Caracalla and (briefly) Geta. There was also a small amount of posthumous coinage produced under Elagabalus following the restoration of the dynasty in 218, **Figures 7-9** (Seaby, 1982b: p. 51; Sear, 1988: p. 194; Sear, 2002: pp. 489-490; Gagarin, 2010: p. 141).

Figure 7. AR Denarius. Rome, 196-211 A.D. th. 2.58 mm.; dim. 17.98 mm.; 2.92 gr.; dir. 1 h. Obv. IVLIA. AVGVSTA, diad. dr. bust r., hair looped up or in knot neck. Rev. CERERI. FRVGIF., Ceres set. l., holding grain ears R. hand and long torch l. hand. (Severus) B.M.C 10-13 and 592; R.I.C 546 and 636; R.S.C III 14; Sear 6576.

Figure 8. AR Denarius. Rome,197-211 A.D. th. 2.15 mm.; dim. 17.41 mm.; 3.21 gr.; dir. 6 h. Obv. IVLIA. AVGVSTA, diad. dr. bust r., hair looped up or in knot neck. Rev. VENVS. FELX, Venus Felix stg. Half-left holding the apple and drawing (drapery) a veil from the shoulder. irregular flan. (Severus) B.M.C. S85 note; R.I.C. 580 notes. 286a; R.S.C 198. Sear, 1851.

Figure 9. AR Denarius. Rome, 211-217 A.D. th. 1.98 mm.; dim. 20.05 mm.; 3.64 gr.; dir. 6 h. Obv. IVLIA. AVGVSTA, diad. dr. bust r., hair looped up or in knot neck. Rev. VENVS. VICTRIX, Venus Victrix, set. l., on the throne, holding palladium (rare) and a scepter. (Severus) B.M.C. 95, 168; R.I.C. 583; R. S. C III, 245; Sear 6612.

After the death of Septimius in 211, she was still treated with some degree of deference by Caracalla, but she was forced to witness the murder of Geta in her arms in A.D. 217. Afterward, she succeeded in disguising her grief to secure the goodwill of her surviving son, who bestowed on her many honors. After Caracalla's murder, she stayed on at Antioch until she was ordered to leave, at which point she committed suicide by refusing all nourishment (Seaby, 1982b: p. 51; Sear, 1988: p. 194; Sear, 2002: p. 491; Varner, 2004: p. 177, 180, 187; Gagarin, 2010: p. 142; Callatay, 2013: p. 316).

7. Plautilla 185/188-212 A.D.

Publia Fulvia Plautilla, the daughter of the enormously rich and powerful praetorian prefect C. Fulvius Plautianus, was a native of the north African city of Lepcis (Leptis) Magna. Appointed to the Pretorian prefecture in AD 197, Plautianus became one of the wealthiest and most influential individuals ever to occupy this important office, his career inviting comparison with the better-known Sejanus during the reign of Tiberius. Like Sejanus, Plautianus may have had designs on the throne itself (Seaby, 1982b: p. 89; Sear, 2002: p. 546; Gagarin, 2010: p. 51, 285). Fulvia married Caracalla in A.D. 202, bringing a large dowry with her. However, the couple had never had any affection for one another, and it is doubtful if the marriage was ever consummated, especially as Caracalla was only fourteen at the time of the wedding (his bride was probably older). Coin types hinting at Imperial offspring are better interpreted as expressions of hope than statements of accomplished fact. Plautilla's coinage commenced with her elevation to the rank of Augusta following her marriage to Caracalla in 202 and continued until her political downfall in 205. It comprises principally gold and silver denominations, such as those classified as being very scarce (*dupondii* and *asses*) or very rare (*sestertii*), **Figure 10** (Metcalf, 2012: p. 512). Her aurei and denarii include a few types from the Syrian mint of Laodicea, though this sole survivor from the time of the eastern wars was closed not long after Plautilla's marriage. She was incredibly snobbish, and her abusive husband quickly despised her. Septimius exiled her to Lipari at his request, following her father's death in A.D. 205. She remained in misery until after Septimius' death, when she was slain on her husband's orders (Seaby, 1982b: p. 89; Sear, 2002: p. 747; Varner, 2004: p. 164; Gagarin, 2010: p. 51, 285; Metcalf, 2012: p. 512).

Figure 10. AR Denarius. Eastern mint (Laodicea), 202-205 A.D. th. 2.44 mm.; dim. 17.94 mm.; 2.64 gr.; dir. 12 h. Obv. PLAVTILLAE AVG VSTAE, dr. bust r., with hair in nearly vertical waves and drawn into a large bun at the neck. Rev. CONCORDIAE, Concordia set. l., holding patera in r. hand and double cornucopia in l. hand. (Caracalla) B.M.C. 300, 734; R.I.C 360 and 370; R.S.C II 7. Sear 7067.

8. Julia Soaemias 180-222 A.D.

Julia Soaemias Bassiana, born probably before AD 180, was the mother of Elagabalus (218-222 A.D.), was the daughter of Julius Avitus and Tulia Maesa, the elder daughter of Julia Domna's sister Julia Maesa and the consular Julius Avitus. She married Varius Marcellus, a senator, who enjoyed a distinguished career under Severus and Caracalla, and gave birth to their son, the future emperor Elagabalus, in AD 204. Elagabalus, Julia Soaemias' son, became Emperor in 218 and gave her the title of Augusta (though apparently not the right of coinage at the time). Becoming a widow, she retired after the death of Caracalla to Emesa, where she and her mother persuaded the troops to declare Elagabalus emperor. She returned to Rome and became a senator (Gagarin, 2010: p. 34). The young emperor's shameless behavior seems to have been inherited from his mother. To Julia Maesa's dismay, Soaemias seemed to encourage rather than attempt to curb his moral depravity and religious fanaticism. As a result, she shared his fate when the prurient mutinied on March 11, AD 222, and murdered both mother and son; their mutilated bodies were dragged through the streets of the city and thrown into the Tiber. The coinage in the name of Julia Soaemias is noticeably scarcer than that of her mother, clearly suggesting a shorter period of issue. Her dated Alexandrian tetradrachms are limited to Elagabalus' regnal years 4 and 5 indicating that no Egyptian coinage was produced for her before late August AD 220. It seems likely that the same is true of her Roman issues. No Antoniniani (*Antoninianus*) (the denomination discontinued in the summer of 219) were struck in her name or denarii of Syrian style, a series that ceased sometime in 220, **Figure 11**, **Figure 12** (Seaby, 1982b: p. 125; Sear, 1988: p. 216; Sear, 2002: p. 626; Gagarin, 2010: p. 34; Metcalf, 2012: p. 572).

Figure 11. AR Denarius. Rome, 218-222 A.D. th.1.96 mm.; dim. 19.46 mm.; 2.92 gr.; dir. 1 h. Obv. IVIA SOAEMIAS AVG, dr. bust r. Rev. VENVS CAELESTIS, Venus set. l., on the throne, holding an apple in r. hand and a scepter in l. hand; in front, a child stg. r., raising both hands. (Elagabalus). B.M.C.R.E 55-60 (describes some as holding patera instead of apple); R.I.C. 243; R.S.C III 14. Sear 7720.

Figure 12. AR Denarius. Rome, 218-222 A.D. th. 1.91 mm.; dim. 19.20 mm.; 2.96 gr.; dir. 12 h. Similar **Figure 11**. (rare) the child shows only the left hand, without raising/ lifting it.

9. Julia Maesa 159-224 A.D.

Julia Maesa, a daughter of Julius Bassianus (160-224 A.D.), priest of the Sun, was born at Emesa (Homs) in Syria; she was the sister of the empress Julia. In 187, she married Julius Avitus. She was a woman of great sagacity and courage and possessed great wealth. She retired to Emesa on Caracalla's death and succeeded in persuading the troops to proclaim Elagabalus emperor. She fought at the head of his troops against Macrinus, and "she was largely responsible for the rebellion that resulted in the overthrow of Macrinus and the restoration of the Severan Dynasty" (Seaby, 1982b: p. 127; Gagarin, 2010: p. 34, 142; Metcalf, 2012: p. 509). Young Antoninus (Elagabalus) ascended the imperial throne, and the entire family slowly made their way back to Rome. Julia Maesa soon realized that she was going to have a difficult task controlling the boy who had been catapulted into such an exalted position, especially as she received little help from the emperor's mother, her daughter Julia Soaemias. All attempts failed, and Maesa had to make the difficult decision to sacrifice her daughter and grandson to ensure the survival of the dynasty. Maesa was by now quiet and gradually faded into the background, her political role being assumed by the astute Mamaca. Alexander issued a small posthumous coinage in her honor. Julia Maesa's coinage was more extensive than that of any other empress during Elagabalus' reign. It commenced almost as early as that of the emperor himself and includes silver Antoniniani (*Antoninianus*), a denomination discontinued in 219, as well as denarii of Syrian mintage, a series that ended in 220. Some scholars believe that Roman coinage in the name of Julia Maesa continued into the reign of Severus Alexander. If so, it is difficult to determine which of her issues belong to the post-Elagabalus phase, and for this reason, we have placed her entire coinage within the period AD 218-222. Against the notion of a continuation of Alexander's reign is the absence of any Alexandrian issues of Maesa after 222. However, the Balkan mint of Marcianopolis (*Parthenopolis*) did produce a significant series of bronze coins combining the portraits of Alexander and his grandmother, who died in 223 A.D. and was greatly missed for her wise counsels, **Figure 13** (Seaby, 1982b: p. 127; Sear, 1988: p. 217; Sear, 2002: p. 630; Varner, 2004: p. 157, 188; Metcalf, 2012: p. 572).

Figure 13. AR Denarius. Rome, 220-222 A.D. th. 2.49 mm.; dim. 18.48 mm.; 2.97 gr.; dir. 12 h. Obv. IVIA MAESA AVG, dr. bust r., occasionally with a diadem (Stéphane). Rev. SAECVLI FELICITAS, Felicitas stg. l. front, hd., holding long caduceus and sacrificing over lighted altar; star in r. field., (Severus Alexander) B.M.C.R.E 79; R.I.C 271; R.S.C III 45; Sear 7757.

10. Otacilia Severa 244-249 A.D.

Marcia Otacilia Severa, the daughter of Severus, Governor of Pannonia, married Philip I (the Arab) 234-249 A.D., about A.D. 234, by whom she had Philip II in A.D. 237 (Seaby, 1982a: p. 17; Metcalf, 2012: p. 575). Though very little is known about the biographical details of her life, she may have been of noble Roman birth, as suggested by her name; if so, one can only speculate on how she came to marry the son of an Arab chieftain. She gave birth to their only son, the younger Philip, about seven years before her husband's accession to the throne and was appointed Augusta's title early in the reign; Otacilia Severa had been Augusta since Philip's ascension. The currency depicts her as symbolizing the regime's conventional values, in the frequent form of its Concord (Brennan, 2004: p. 46). She enjoyed a generous share of the imperial coinage, with one of the six officials of the Rome mint being assigned to the production of issues in her name. Antioch also struck Antoniniani (*Antoninianus*) for her, although these are by no means common. Otacilia's fate is shrouded in mystery. She was in Rome at the time of her husband's defeat by Decius in AD 249. It is unclear, however, whether she was murdered by the praetorians at this time or merely permitted to retire into private life, **Figure 14** (Varner, 2004: p. 151; Sear, 2005: p. 324; Callatay, 2013: p. 312; Metcalf, 2012: p. 172; Metcalf, 2012: p. 480).

Figure 14. AR Antoninianus. Rome, 245-247 A.D. th. 1.77 mm.; dim. 22.96 mm.; 4.21 gr.; dir. 6 h. Obv. M. OTACIL SEVERA AVG. dr. diad. bust r., resting on a crescent (denarii and quinarii). Rev. CONCORDIA AVGG., Concordia set. l., holding patera in r. hand and double cornucopia in l. hand. R.I.C125; R.S.C IV 4; Sear 9147.

11. Salonina 253-268 A.D.

Cornelia Salonina, also known as Chrysogone ("begotten of gold"), was of Greek origin and had been married to Gallienus 253-268 A.D. (Seaby, 1982b: p. 111; Sear, 1988: p. 265). "Salonina was the equal of Agrippina Senior or Faustina Junior for her intrepid spirit and her support of the army; indeed, she was hailed Mater Castrorum", Many additional attributes are credited to her. Salonina and Gallienus were both benefactors of the arts and strong followers of Plotinus, the Neoplatonist philosopher who lived in the mid-3rd century. We have no reason to doubt that she participated in her husband's flamboyant lifestyle, for she is honored with the rare epithet Crysogone, which means "Golden Born" or "Begotten of Gold" on several provincial coins, mainly from Ionia and Lydia. Salonina married Gallienus around 240, and the couple had three children, all of whom are portrayed on the reverse of the aureus. We may presume that Salonina's adoration is focused on her family rather than the gods because the principal figure, symbolizing her is not veiled. Valerian II and Saloninus, two of these offspring, gained imperial positions under their father, but both died tragically before their parents (Seaby, 1982b: p. 111; Sear, 1988: p. 265; Varner, 2004: p. 211). Salonina's Alexandrian coinage commences only during the third regnal year (AD 255-6), and this may be the date of her elevation to the rank of Augusta. A woman of sophistication and learning, she and her husband were both members of the philosopher Plotinus' circle of intellectuals in Rome, and it is possible that she also had Christian sympathies. In AD 268, the empress was probably a witness to her husband's murder during the siege of Milan; her subsequent fate is unknown. An extensive coinage was issued in Salonina's name, both during the joint reign of Valerian and Gallienus and throughout the period of her husband's sole rule. It was on a larger scale than for any empress since the time of Julia Domna, wife of Septimius Severus, **Figures 15-20** (Sear, 2005: p. 324; Callatay, 2013: p. 312; Metcalf, 2012: p. 575).

Figure 15. AR Antoninianus. Rome, 257-260 A.D. th. 1.57 mm.; dim. 23.59 mm.; 2.78 gr.; dir. 12 h. Obv. SALONINA AVG, diad. dr. bust r., resting on a crescent. Rev. PIETAS AVGG., Pietas set. l., holding a scepter. In l. hand and extending r. hand, two children stg. r. at her feet and resting on a scepter held in l., and a third child stg. beside her on l. side. R.I.C 35, 59; R.S.C IV 84, 84a; Sear 10647. Extremely rare and in exceptional condition for the issue, undoubtedly among the finest specimens known.

Figure 16. AR Billon Antoninianus. Asia Mint (Uncertain Syrian mint), 258-260 A.D. th. 1.73 mm.; dim. 20.33 mm., 3.88 gr.; dir. 6 h. Obv. SALONINA AVG, diad. dr. bust r., resting on a crescent. Rev. ROMAE AETERNAE, Roma set. l., shield on the side, holding a spear, and presenting Victory to Emperor Gallienus stg. r. before her star in the field above. R.I.C 67, R. S.C IV 103; Sear 10651.

Figure 17. AE Billon Antoninianus. Asian mint (Uncertain Syrian mint), 258-260 A.D. th. 1.88 mm.; dim. 20.68 mm.; 4.18 gr.; dir. 12 h. Obv. CORN SALONINA AVG, diad. dr. bust r., resting on a crescent. Rev. CONCORDIA AVGG, Gallienus, togate, stg. r., clasping hands to empress Salonina. stg. l., facing each other, wreaths in the field above. R.I.C 63; R.S.C 31, 31a; Sear 10630.

Figure 18. AR Billon Antoninianus. Antioch, 260-264 A.D. th. 1.74 mm.; dim. 22.18 mm.; 2.91 gr.; dir. 12 h. Obv. SALONINA AVG, dia., dr. bust r., wearing Stephane, on the crescent. Rev. IVNO REGINA, Juno stg. l., holding patera and scepter; peacock at Juno's feet in l. R.I.C 92; R.S.C IV 67; Sear 10641.

Figure 19. AR Billon Antoninianus. Antioch, 265-267 A.D. th. 1.92 mm.; dim. 19.87 mm.; 4.73 gr.; dir. 6 h. Obv. SALONINA AVG, diad. dr. bust r., resting on a crescent. Rev. VENVS AVG, Venus stg. l., holding a helmet and transverse spear and resting on a shield at her side; Mintmark: PXV in exergue = (TR P XV). R.I.C 86; R.S.C IV 113; Sear 10654.

Figure 20. AE Billon Antoninianus. Antioch, 265-267 A.D. th. 2.01 mm.; dim. 21.51 mm.; 4.22 gr.; dir. 6 h. Obv. SALONINA AVG, diad. dr. bust r., resting on a crescent. Rev. VENVS AVG, Venus stg. l., holding the apple and the transverse spear and resting on the shield on her side; Mintmark: PXV in exergue = (TR P XV). R.I.C 31; R.S.C V 3047.

12. Severina 270-275 A.D.

Lile is known for the history or ancestry of Ulpia Severina, the wife of Aurelian, although her name would indicate Spanish origin (Sear, 1988: p. 283). Aurelian was a career soldier from an Illyrian background. According to Brennan (Brennan, 2004: p. 46), he was to be the one who reunited the shattered Roman world under one emperor and was to be honored with the title *Restitutor Orbis* (World Restorer). As she did not become Augusta until late in her husband's reign, Severina's coinage extends only over a short period (AD 274-275) but is nevertheless of considerable interest. The numismatic evidence makes it clear that issues in her name continued for some time after Aurelian's death, though the precise length of this "interregnum" period is much disputed by scholars. It was formerly believed that the accession of Tacitus was delayed by six months, but it now seems likely that the new emperor's proclamation took place less than two months after his predecessor's murder. The fate of Severina is unknown, but it may be presumed that she retired into private life and was honored by her husband's successors (Sear, 1988: p. 438). The coin below was minted under Augusta Severina, in the Antioch mint. It can be emitted after the east has recovered. The reverse CONCORDIAE MILITVM legend may indicate that the Severina is associated with the Soldiers' Concord, **Figure 21**, **Figure 22** (Brennan, 2004: pp. 46-47).

Figure 21. AE Billon Antoninianus. Siscia mint, 274-275 A.D. th. 1.85 mm.; dim. 23.84 mm.; 3.63 gr.; dir. 12 h. Obv. SEVERINAE AVG, diad. dr. bust r., wearing Stephane resting on a crescent. Rev. CONCORDIAE MILITVM. Concordia Militum stg. facing l., holding standards/ensigns in each hand, IV in r. field (=); Mintmark: XXI in exergue. R.I.C V-1, 13; R.C.V 3282; Cohen 8; Sear 11706.

Figure 22. AE Antoninianus. Siscia mint, 274-275 A.D. th. 1.85 mm.; dim. 23.82 mm.; 3.59 gr.; dir.12 h. Similar **Figure 21**. without IV in r. field.

13. Galeria Valeria 293/305-311 A.D.

Galeria Valeria, the daughter of Diocletian and Prisca, was born between 284 and 305 A.D. In 293 he married Galerius' second wife. Valeria was promoted to the titles of Augusta and Mater Castrorum in 308. Valeria adopted Candidianus, her husband's illegitimate son, as her own because Galerius had no children with her. Despite being a Christian or liking Christianity, she was compelled to sacrifice to the gods during the Great Persecution of 303 and was venerated alongside her mother as a Christian saint (Varner, 2004: p. 215, 221).

Valeria and her mother Prisca were handed to Licinius after Galerius died in 311. However, the two ladies escaped from Licinius to Maximinus II, whose daughter was engaged to Candidianus. Valeria denied Maximinus' marriage proposal after a short time, and he captured and imprisoned her in Syria, confiscating her property. Licinius ordered the execution of both ladies when Maximinus died. Valeria went into hiding for a year before being discovered in Thessaloniki. In 315 A.D., she was kidnapped by a crowd, killed in the city's great plaza, and her body dumped into the sea, **Figure 23** (Varner, 2004: p. 215, 221; Gagarin, 2010: p. 421; Metcalf, 2012: p. 598).

Figure 23. AE Follis. Cyzicus mint, 308-311 A.D. th. 2.43 mm.; dim. 24.36 mm.; 5.34 gr.; dir. 12 h. Obv. GAL VAL., ERIA AVG diad. and dr. bust r. Rev. VENTERI V. ICTRICI. Venus sgt. l., holding up an apple in r. hand and raising drapery over the shoulder with l., A Δ (Delta) in l. field, with Mintmark: MKV? in exergue. R.I.C. IV 46; Sear 14597.

14. Conclusion

This study sheds some light on twenty-three Roman coins, dating back to twelve Roman empresses. It was found that eighteen coins were made of silver, and eighteen coins were made of bronze/copper. This study sample extends from the beginning of the second century A.D. to the beginning of the fifth century A.D. Some 50 types are minted in Trajan's time in year 11 (126/127) (Al-Rawahneh, 2002: p. 32), probably for his tenth birthday. In contrast to Trajan, Hadrian continues a dynastic scheme, beginning with pictures of members of his wife Sabina's imperial house in year 13 (128/129) and his chosen heir, L. Aelius Caesar (with a Roman date) (137). In year 15 (130/131), Sabina even gets her tetradrachm series (Metcalf, 2012: p. 569), probably for his tenth birthday. In contrast to Trajan, Hadrian continues a dynastic scheme, beginning with pictures of members of his wife Sabina's imperial house in year 13 (128/129) and his chosen heir, L. Aelius Caesar (with a Roman date) (137). In year 15 (130/131), Sabina even gets her tetradrachm series. The currency reflects Marcus Aurelius and Lucius Verus' combined administration until 169. Faustina II and Lucilla, as well as Commodus in the role of Caesar, make appearances. The decennalia (Decennia), as well as Homonoia and the victory over Armenia, are depicted. Marcus Aurelius' tetradrachm coinage begins to drop visibly in year 10 (169/170) but deteriorates significantly in year 17 (176/177); copper coinage is also reduced (Howgego, 1992: p. 4).

It is just speculation if the general decrease in currency output at this period is connected to the visible drop in population. The population loss might be linked to the plague of 165/166, but it could also be linked to the events leading up to the so-called Bucoli insurrection (Metcalf, 2012: p. 571). The Roman mint began striking significant coinage in the name of Augusta in the later part of Hadrian's reign, possibly from his decennalia forward. The Antonines continued and intensified this practice. Duncan-Jones (1994: pp. 72-75) used hoard evidence to assess the extent of manufacturing. To summarize, during Hadrian and Commodus, around one out of every seven coins was made for the Augusta, but under Pius and Marcus, this increased to about two out of every seven. Duncan-Jones (1994: p. 75) speculates that this trend may be due to their use as coinage for two imperial ladies under Pius (Faustina I and II) and Marcus (Faustina II and Lucilla), whereas there was only one Augusta during Hadrian and Commodus (Sabina and Crispina, respectively). There is no comparable documented hoard evidence to provide a direct comparison, which demonstrates that over half of provincial mints working during the reigns of Pius and Marcus issued coins depicting Augusta, while fewer than a quarter of those operating during the reign of Commodus did. However, far fewer types were produced than might appear. Under Pius and Marcus, around one in every seven provincial coin types had a girl on the obverse, but this dropped to one in every fourteen under Commodus. The most noticeable feature is the continuous halving of the output of a "female" coin during Commodus at imperial and provincial mints. Furthermore, the dramatic decrease in the number of provincial mints that select the Augusta mint at all shows that the cause of the fall may have less to do with the number of Augustae (Metcalf, 2012: p. 433).

Acknowledgements

This work was partially supported by the Scientific Research Committee/ Mutah University. This private collection of Roman coins is owned by Dr. Nayef Al-Qoussous and is housed in the Jordan Ahli Bank Numismatics Museum. The authors would like to thank Dr. Nayef Al-Qoussous, who allowed us to study and publish these coins, and Dr. Hassan Al-Zuod, Numismatic Museum Manager, who helped us and transmitted to us certain useful data.

Conflicts of Interest

The authors declare no conflicts of interest regarding the publication of this paper.

References

Abdy, R. A. (2014). Chronology of Sabina's Coinage at the Roman Mint. *Revue Numismatique, Année, 171,* 73-91. https://doi.org/10.3406/numi.2014.3242

Al-Rawahneh, M. (2002). *The Reign of Aretas IV in the Light of Nabateans Numismatics* *from a Private Collection*. Bayt Al-Anbat Press, Alrai Newspaper.

Brennan, P. (2004). The Coins. In P. Brennan, M. Turner, & N. L. Wright (Eds.), *Faces of Power. Imperial Portraiture on Roman Coins* (pp. 15-77). Nicholson Museum, The University of Sydney.

Callatay, F. (2013). *Ancient Coins of the JDL Collection Auction Part I, Numismatica*. ARS Classica NAC AG.

Duncan-Jones, R. (1994). *Money and Government in the Roman Empire.* Cambridge, New York, Melbourne: Cambridge University Press.

Gagarin, M. (2010). *The Oxford Encyclopedia of Ancient Greece and Rome*. 7-Volume Set, Oxford University Press.

Howgego, C. (1992). The Supply and Use of Money in the Roman World 200 B.C. to A.D. 300. *The Journal of Roman Studies, 82,* 1-31. https://doi.org/10.2307/301282

Metcalf, W. E. (2012). *The Oxford Handbook of Greek and Roman Coinage*. Oxford University Press. https://doi.org/10.1093/oxfordhb/9780195305746.001.0001

Seaby, H. A. (1979). *Roman Silver Coins, Revised by Robert Loosley, Volume II, Tiberius to Commodus, Arranged According to Gohen* (3rd ed.). Seaby Publications Ltd.

Seaby, H. A. (1982a). *Roman Silver Coins, Revised by David R. Sear, Volume IV, Gordian III to Postumus, Arranged According to Gohen* (2nd ed.). Seaby Publications Ltd.

Seaby, H. A. (1982b). *Roman Silver Coins, Revised by David R. Sear, Volume III, Pertinax with Balainus and Pupienus, Arranged According to Gohen* (2nd ed.). Seaby Publications Ltd.

Sear, D. R. (1988). *Roman Coins and their Values* (4th Revised ed.). Seaby Publications Ltd.

Sear, D. R. (2002). *Roman Coins and Their Values, Volume II, The Accession of Nerva to the Overthrow of the Severan Dynasty AD 96-235, Spink*. The Cambridge University Press.

Sear, D. R. (2005). *Roman Coins and Their Values, Volume III, The Third Century Crisis and Recovery AD 235-285. Spink*. The Cambridge University Press.

Varner, E. R. (2004). *Mutilation and Transformation, Damnatio Memoriae and Roman Imperial Portraiture (Monumenta Graeca et Romana) (No. 10)*. Brill.

Abbreviations

l.	= Left
r.	= Right
AR	= Silver
AE	= Copper/Bronze
Obv.	= Obverse
Rev.	= Reverse
th.	= Thickness
dim.	= Diameter
dir.	= Direction
mm	= Millimeters
gr.	= Grams
set.	= Seated
stg.	= Standing
dr.	= Draped
diad.	= Diademed
ex.	= Exergue
hd.	= Head
p.	= Page
pl.	= Plate
R.I.C	= The Roman Imperial Coinage
C.R. B	= The Coinage of Roman Britain
R.S.C	= Roman Silver Coins
R.C. V	= Roman Coins and Their Values
B.M.C	= British Museum Catalogue
B.C.E.	= Before the Common Era
A.D.	= Anno Domini ("in the Year of the Lord" the Year Jesus Was Born)

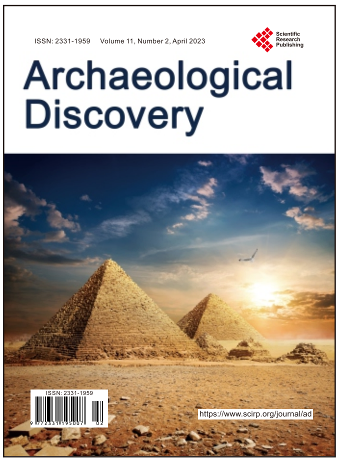

Call for Papers

Archaeological Discovery

ISSN Print: 2331-1959 ISSN Online: 2331-1967
https://www.scirp.org/journal/ad

Archaeological Discovery (AD) is an international journal dedicated to the latest advancement in the study of Archaeology. The goal of this journal is to provide a platform for scientists and academicians all over the world to promote, share, and discuss various new issues and developments in different areas of Archaeological studies.

Subject Coverage

All manuscripts must be prepared in English, and are subject to a rigorous and fair peer-review process. Generally, accepted papers will appear online within 3 weeks followed by printed hard copy. The journal publishes original papers covering a wide range of fields but not limited to the following:

- Aerial Archaeology
- Archaeological Method and Theory
- Archaeological Science
- Archaeometry
- Art Archaeology
- Environmental Archaeology
- Ethnoarchaeology
- Experimental Archaeology
- Field Archaeology
- Geoarchaeology
- Historical Archaeology
- Island and Coastal Archaeology
- Lithic Studies
- Maritime Archaeology
- Prehistoric Archaeology
- Religious Archaeology
- Social Archaeology
- Underwater Archaeology
- World Archaeology
- Zooarchaeology

We are also interested in: 1) Short reports — 2-5 page papers in which an author can either present an idea with a theoretical background but has not yet completed the research needed for a complete paper, or preliminary data; 2) Book reviews — Comments and critiques, special peer-reviewed issue for colloquia, symposia, workshops.

Website and E-Mail

https://www.scirp.org/journal/ad E-mail: ad@scirp.org

What is SCIRP?

Scientific Research Publishing (SCIRP) is one of the largest Open Access journal publishers. It is currently publishing more than 200 open access, online, peer-reviewed journals covering a wide range of academic disciplines. SCIRP serves the worldwide academic communities and contributes to the progress and application of science with its publication.

What is Open Access?

All original research papers published by SCIRP are made freely and permanently accessible online immediately upon publication. To be able to provide open access journals, SCIRP defrays operation costs from authors and subscription charges only for its printed version. Open access publishing allows an immediate, worldwide, barrier-free, open access to the full text of research papers, which is in the best interests of the scientific community.

- High visibility for maximum global exposure with open access publishing model
- Rigorous peer review of research papers
- Prompt faster publication with less cost
- Guaranteed targeted, multidisciplinary audience

Scientific
Research
Publishing

Website: https://www.scirp.org
Subscription: sub@scirp.org
Advertisement: service@scirp.org